THE NUMERICAL MODELLING OF A FLUE GAS PRECIPITATOR.

G. C. van Eeden

B. Eng. (Mechanical)

Dissertation submitted in partial fulfilment of the requirements for the degree
Magister Ingeneriae
in the
School of Mechanical and Materials Engineering
Faculty of Engineering
at the
Potchefstroom University for Christian Higher Education.

Promoter: Prof. C. G. de K. du Toit
POTCHEFSTROOM, SOUTH AFRICA
2003

ABSTRACT

Suspended fly-ash particles in industrial emission gasses have a major degrading effect on the whole environment. Electrostatic precipitation is one of the oldest and most effective gas-cleaning processes used today. Electrostatic precipitators use electrostatic forces to clean the flue gas of ash particles. Stricter emission control laws force industries (like SASOL) to improve their electrostatic precipitators.

This study consists of a comprehensive literature survey and the development of a numerical fluid flow model. The proper flow of the gas through an electrostatic precipitator is one of the most important factors to ensure high collection efficiencies. The gas flow must be distributed over the whole flow domain in order to utilize the entire collecting area. The three-dimensional numerical model only considers the fluid dynamics of a precipitator. The finite volume method together with the SIMPLE algorithm is used to solve the fluid dynamic equations.

The computer resources available are not sufficient to simulate the full detail of the structures inside a full-scale precipitator. Thus the precipitator flow domain was simplified by making certain assumptions and approximations. The distribution plates in the precipitator inlet ensure good gas distribution through the entire precipitator. Porous baffles are used to approximate the distribution plates and the electrical fields are approximated by porous mediums.

The effect of the distribution plates and the electrical fields on the gas flow through the precipitator was investigated. The results have shown that the gas flow was expanded over the whole flow domain and the maximum velocity inside the precipitator was significantly reduced because of the effect of the distribution plates. The simulated gas flow velocity profiles are in relative good agreement with measured velocity profiles. The methodology followed in this study can be used to predict gas flow patterns inside a precipitator but further research is necessary.

OPSOMMING

Industriële uitlaatgasse bevat klein vlieg-as deeltjies wat 'n groot nadelige invloed op die omgewing het. Elektrostatiese presipitasie is een van die effektiefste prosesse wat hedendaags gebruik word om hierdie vlieg-as deeltjies uit die uitlaatgasse te verwyder. Elektrostatiese presipitators gebruik elektrostatiese kragte om die asdeeltjies van die uitlaatgasse te skei. Industrieë (soos SASOL) word deur strenger omgewingswette gedwing om hulle elektrostatiese presipitators te verbeter.

Hierdie studie bestaan uit 'n omvattende literatuurstudie en die ontwikkeling van 'n numeriese model, wat die gasvloei deur 'n presipitator simuleer. Die korrekte vloei van die gas deur 'n presipitator is een van die belangrikste faktore om hoë presipitator effektiwiteite te verseker. Die gasvloei moet oor die hele vloeigebied versprei wees om sodoende die opvangarea ten volle te benut. Die drie-dimensionele numeriese model simuleer slegs die gasvloei deur 'n industriële presipitator. Die vloeidinamika van die presipitator word opgelos met behulp van die eindige volume metode en die SIMPLE algoritme

Die beskikbare rekenaarhulpbronne is nie voldoende om die volle interne geometrie van 'n industriële presipitator te simuleer nie. Die komplekse interne geometrie word vereenvoudig deur sekere aannames en benaderings te maak. Geperforeerde plate in die presipitator inlaat, verseker dat die gasvloei oor die hele opvangarea versprei word. Poreuse smoorplate word gebruik om die geperforeerde plate te benader, terwyl die elektriese velde deur poreuse mediums benader word.

Die effek van die geperforeerde plate en die elektriese velde op die gas vloei deur die presipitator was ondersoek. Die resultate het getoon dat die gas vloei oor die hele vloei area versprei was en die maksimum vloeisnelheid was aansienlik verminder as gevolg van die geperforeerde plate. Die gesimuleerde snelheids profiele het goeie ooreenkomste getoon met gemete snelheidsprofiele. Die numeriese model kan gebruik word om die gas vloei deur 'n presipitator te ondersoek maar verdere ontwikkeling is nodig.

ACKNOWLEGEMENTS

Firstly I would like to thank my study leader Prof. C.G. du Toit for his guidance, leadership and advice. Without his comforting words and knowledge this study would not have been possible. I would also like to thank Mr. L. A. le Grange of Softflo cc. for providing me unrestricted use of his commercial software, Flo++ and for his time, efforts and advice during the development stages of the numerical model.

Secondly I would like to thank my study mentor at SASOL, Mr. H. Botes and the SASOL personnel at the boiler plant, for providing me with the necessary information and dimensions, in order to complete this study. Also for organising the visits to Secunda, the long distance arrangement proved to be a problem sometimes. Mr. W. Schmitz for providing information on literature sources.

Thanks to my fellow colleagues and friends for their technical support and for making the last two years more enjoyable. Special thanks to Hans and Francois for their personal time and input during the study. Thanks to Jo for her continuous support and her willingness to help.

My eternal gratitude to my mom, dad and sisters for their encouraging words, prayers and support during the last two years. Thanks for giving me the opportunity to study and believing in me.

Most importantly I would like to give praise to my heavenly Father for giving me the opportunity, persistence and ability to complete this project. Also for giving me the privilege to share my life with a loving family and great friends.

Gert van Eeden

TABLE OF CONTENTS

NOMENCLATURE

Roman letters

$\bar{n}$	Normal vector to surface dA	see Eqn. (3.22)
$\bar{S}_M$	Source term vector, $\bar{S}_M\left(S_{Mx},S_{My},S_{Mz}\right)$	–
$\bar{U}$	Velocity vector, $\bar{U}(U,V,W)$	–
$\bar{u}$	Total velocity vector, $\bar{u}(u,v,w)$	m/s
$\lvert\bar{u}\rvert$	Magnitude of superficial velocity	m/s, see Eqn. (4.6)
A	Collecting area	m^2, see Eqn. (2.1) & (2.3)
A	Surface area of the Control volume	m^2
a	Neighboring coefficients	see Eqn. (3.27)
b	Coefficient in SIMPLE algorithm	see Eqn. (3.28)
C_μ	Dimensionless constant	see Eqn. (3.43)
$C_{1\varepsilon}$	Adjustable constant	see Eqn. (3.45)
$C_{2\varepsilon}$	Adjustable constant	see Eqn. (3.45)
CV	Control volume	m^3
D	Diffusion coefficient	m^2
d	Coefficient in SIMPLE algorithm	see Eqn. (3.35)
E_{ij}	Mean rate of deformation component	–
e	Thickness of ash layer on collecting plate	m
F	Convective flux per unit area	m^2
I	Current	A
I_{dr}	Turbulence intensity	–
j	Density of electrical current that cross ash layer	C/m^3
K_i	Permeability of porous media	–
k	Turbulent kinetic energy	m^2/s^2
L	Thickness of catalyst (ash) layer	m

L_{dr}	Turbulent length scale	–
p	Pressure	Pa
p_{out}	Outlet pressure	Pa
Q	Volumetric flow	m^3/s
R	Resistance	Ω
r	Catalyst (ash) resistivity	Ω/m
S_M	Directional component of source term	–
S_ϕ	Source term for ϕ	–
$S_{\phi P}$	Source term for ϕ in control volume	–
t	Time	s
u	Velocity component in x-direction	m/s
u_i	Superficial velocity in ξ_i-direction	m/s
V	Voltage potential	V, see Eqn. (2.2)
V_p	Volume of Control volume	m^3
V_r	Voltage decrease because of ash layer	V
v	Total velocity component in y-direction	m/s
v_n	Superficial velocity towards porous baffle	m/s
v_1	Design velocity	m/s
v_2	Measured velocity	m/s
v_3	Minimum velocity	m/s
w_m	Migration velocity	m/s
w	Total velocity component in z-direction	m/s
x	Distance in Cartesian direction x	m
y	Distance in Cartesian direction y	m
z	Distance in Cartesian direction z	m

Greek letters

$\bar{\tau}$	Viscous stresses vector	Pa
α	User-specified coefficient defining permeability	–
β	User-specified coefficient defining permeability	–
ε	Turbulent dissipation rate	m^2/s^3
ϕ	General variable	–
Γ	General variable	–
η	Collection efficiency	–
λ	Volumetric deformation viscosity	$kg/m \cdot s$
μ	Dynamic viscosity	$kg/m \cdot s$
μ_g	Specified fluid viscosity	$kg/m \cdot s$
μ_t	Eddy viscosity	m^2/s
ρ	Fluid density	kg/m^3
ρ_g	Specified fluid density	kg/m^3
ρ_r	Electrical resistivity of ash layer	$\Omega \cdot m$, see Eqn. (2.5)
σ_k	Prandtl number	see Eqn. (3.44)
σ_ε	Prandtl number	see Eqn. (3.45)
τ	Viscous stresses	Pa
ξ_i	Orthotropic direction	–

Super and subscripts

B	Cell center on numerical grid (bottom)	
b	Cell face on numerical grid (bottom)	
catalyst	Characteristic of catalyst (ash)	see Eqn. (2.2)
E	Cell center on numerical grid (east)	
e	Cell face on numerical grid (east)	
I	Cell center location in the x-direction	
i	Cell face location in the x-direction	

J	Cell center location in the y-direction	
j	Cell face location in the y-direction	
N	Cell center on numerical grid (North)	
n	Cell face on numerical grid (North)	
nb	Neighbouring cell	
P	Cell center on numerical grid (central point)	
$plate$	Characteristic at collecting plate	see Eqn. (2.2)
S	Cell center on numerical grid (south)	
s	Cell face on numerical grid (south)	
T	Cell center on numerical grid (top)	
t	Cell face on numerical grid (top)	
W	Cell center on numerical grid (west)	
w	Cell face on numerical grid (west)	
x	In Cartesian direction x	
y	In Cartesian direction y	
z	In Cartesian direction z	
'	Correction value	
*	Temporary value	

LIST OF FIGURES

Chapter 1: Introduction

Chapter 2: Literature Survey

Chapter 3: Theory

Chapter 4: ESP Model

Chapter 5: Results

Appendix B: Simulation Results

LIST OF TABLES

Chapter 3: Theory

Chapter 4: ESP Model

Chapter 5: Results

CHAPTER 1

1. Introduction

1.1 Introduction

Electrostatic precipitation is one of the most efficient and oldest gas-cleaning processes used today. A short background followed by the basic operation of the electrostatic precipitation process is given. The purpose of the study, the problem statement and a short description of every chapter complete this chapter.

1.2 Background

Air pollution is a major concern in today's industry. The problem of air pollution is one that grows with our civilization, and is a result of it. Suspended particles in industrial emission gasses can be very harmful when inhaled by humans and animals. Such particles have a degrading effect on the whole environment. As a result stricter emission control laws are enforced on the industries to improve their gas-cleaning processes. This is necessary to limit the number of suspended particles in the emission gasses.

Gas-cleaning processes can be mechanical or electrical in nature. Mechanical processes refer to processes that fundamentally depend on inertial or mechanical forces. These processes include gravity settling, centrifugal or cyclonic separation, gas washing or scrubbing, filtration through screens, fabric bags or packed beds and sonic agglomerations. Electrical processes depend mainly on electrical forces to separate the suspended particles from the emission gasses. The most commonly known electrical gas-cleaning process is electrostatic precipitation and is used in electrostatic precipitators (ESPs).

Electrostatic precipitation has many advantages, both in operation and in application. In most mechanical processes the separation process affects the entire gas stream. In electrostatic precipitation the separation forces are only applied to the particles and not the entire gas flow. This direct use of the forces explains the little energy needed to operate the system. Modern power plants only use 0.1% of the generated power to operate the charging and collection of dust in the ESPs. The wide range of particle sizes collected by ESPs (Electrostatic precipitators) is another important advantage of this electrical process. The finest particles can be collected because of the relatively large electric forces acting on the particles. The typical size of particles collected varies from 100 μm to the sub-micron size. There is almost no limit to the cleaning efficiency of an ESP, and some precipitators obtain efficiencies between 98% and 99.9%.

Electrostatic precipitation is used in many areas such as; power generation, steel and cement production and the processing of paper and nonferrous metals. Electrostatic precipitation is also used in the chemical industries for phosphate processing, petroleum refining and sulphuric acid production.

The most common use for ESPs is in boiler plants. A typical industrial boiler (±500 MW boiler) can burn over 200 tons of coal per hour. The fly ash content may be 10% to 40% depending on the quality of the coal. Therefore, between 480 tons and 1920 tons of fly ash can be deposited in the ESP on a daily basis. These statistics are for one ESP alone and most power plants have at least seven to ten ESPs working at the same time. Thus, a small enhancement in the collection efficiency will lead to a large increase in the amount of fly ash collected.

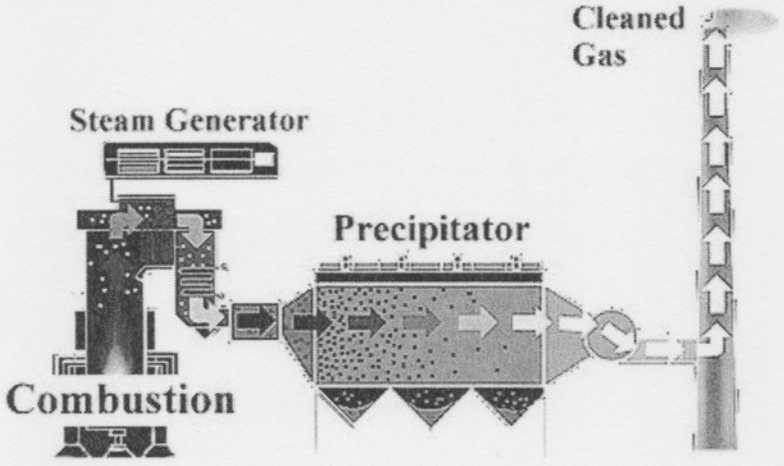

Figure 1.1: Operation of an ESP in a boiler plant.

1.3 Basic Operation

Figure 1.1 illustrates the basic operation of an ESP in a boiler plant. The boiler burns coal in order to generate steam. The ash that remains can be divided into two parts. The coarse ash is collected by hoppers at the bottom of the boiler and is removed via conveyer belts. Small ash particles called fly-ash remain in the emission gasses from the boiler and have to be separated from the exhaust gasses before they can be released into the environment. The ESP collects and removes the fly ash from the emission gasses.

An ESP can be defined as an apparatus which utilizes electrical forces to separate small particles from gasses. The main components are the ESP shell, the high-voltage power supply, the wire electrodes, the collecting plates (ground electrodes), the rapping system and the hoppers. Figure 1.2 shows an industrial ESP with its main components.

There are basically three steps in the collection and removal of the suspended particles:

- The electrical charging of the particles.
- The collection of the charged particles.
- The removal of the particles from the collecting electrodes.

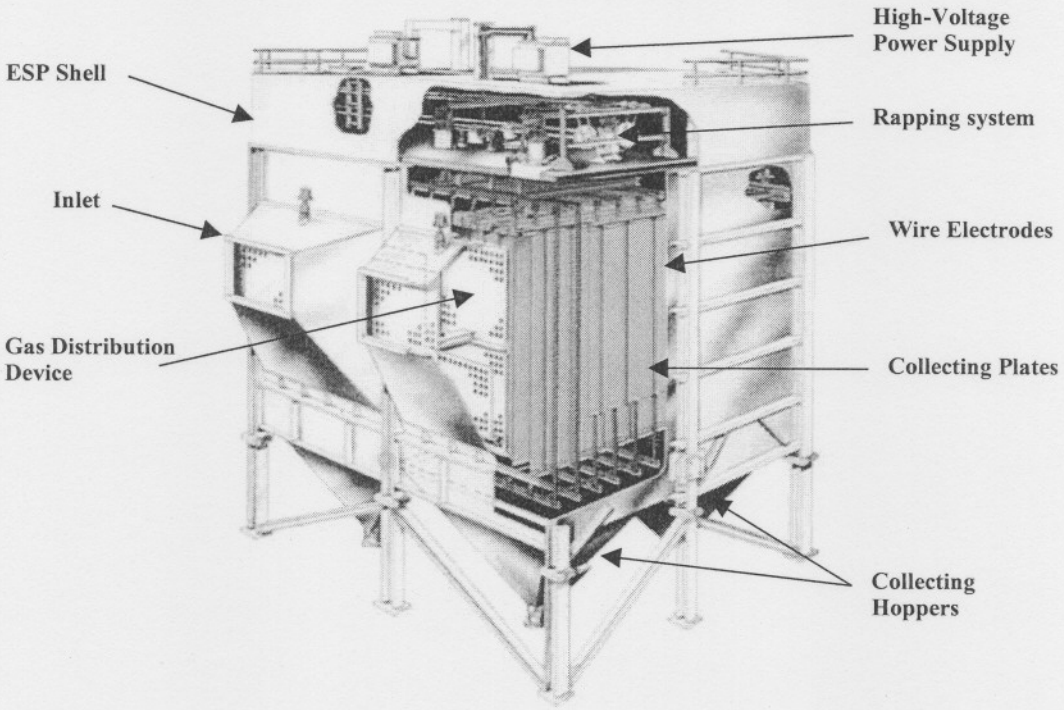

Figure 1.2: An Industrial ESP.

Figure 1.3 illustrates the basic internal workings of an ESP. Most single stage precipitators consist of wire electrodes suspended between parallel plates. The parallel plates (collecting electrodes) are usually at about 300mm intervals. The emission gasses containing the suspended particles flow horizontally through these collecting passages. The electrical field, established between the wire electrodes and the collecting plates, charges the particles. The discharged wires are connected to the high voltage power supply and are usually at negative polarity. The collecting plates are connected to the ground terminal at zero voltage. A corona region is formed between the discharged electrodes and grounded plates. The corona is manifested by a highly active visible glow in the electric field region near the wire surface. Large numbers of negative ions are formed in this glow region and are attracted by the ground plates.

The collecting plates attract the electrically charged ash particles. Dust cakes are formed on the collecting plates because of the agglomeration forces between the dust particles. These dust cakes are periodically loosened by a rapping mechanism and fall into hoppers, situated at the bottom of the ESP shell.

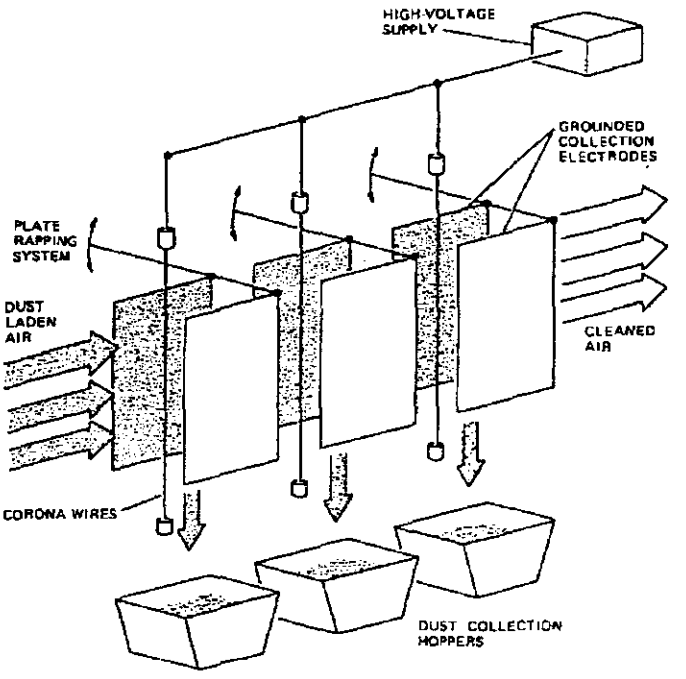

Figure 1.3: Basic internal workings of a wire-plate ESP (Palmer, 1996).

1.4 ESP Design

In the earlier years ESP design and improvements were based on experimental results and on certain rule-of-thumb procedures. These methods were necessary but limited in scope and unable to explain the internal working of an ESP. Since the late 1940's ESP design relied more on the fundamental laws. The development in computer technology and numerical methods, during the last two decades, enabled researchers to develop complex mathematical ESP models. The process of electrostatic precipitation is very complex and consists of various phenomena that interact. Using computer resources these models can then be solved in a numerical manner.

1.5 Environmental laws

The Chief Air Pollution Control Officer (CAPCO) is the main environmental body in South Africa, which specifies the allowable emissions of the industries. CAPCO forces industries like SASOL (South African Coal, Oil and Gas Corporation) to continuously improve their gas-cleaning processes, in

order to comply with the specifications. If the emissions of the plant exceed the CAPCO regulations the plant load must be lowered. This will lead to a significant loss of revenue for the company. The CAPCO specification for SASOL II and III are currently at an average particle emission of about 180mg/Sm^3, where S represents "standard". The current particle emissions are about 100mg/Sm^3, and their target for the nearby future is 50mg/Sm^3. In order to reach this goal the ESPs must be improved and retrofitted.

1.6 ESP Phenomena

The basic internal workings of an ESP are known but there are still many grey areas that need more understanding. The theory of electrostatic precipitation can be divided into three different areas: fluid dynamic flow, electrostatic field and particle dynamics. Every one of these areas has its own unique phenomena and it is the interaction of these phenomena that makes the electrostatic precipitation process possible.

1.6.1 Fluid Dynamic Flow

The gas flow inside a precipitator is one of the most important parameters that influence ESP efficiency. Its influence is equal to or greater than that of the corona and electrostatic forces acting on the particles. Excessive turbulence, gas jets, swirls, pulsations and other unbalanced flow conditions will cause large re-entrained losses and will lead to poor collection efficiencies. It is common that collection efficiencies can be increased from 70% to 95% only by improving the gas flow. The gas flow is also the first factor under consideration when improvements are needed.

1.6.2 Electrostatic Field

The electrostatic field between the discharge electrodes and collecting plates interacts with the particles in the gas flow. The particles are charged through the electrostatic field and the collisions with ions. The Coulomb body forces acting on the particles, force them to move along the electric field lines. Figure 1.4 shows the typical electrical field lines between the discharge electrodes and collecting plates. The ions and the charged particles in the

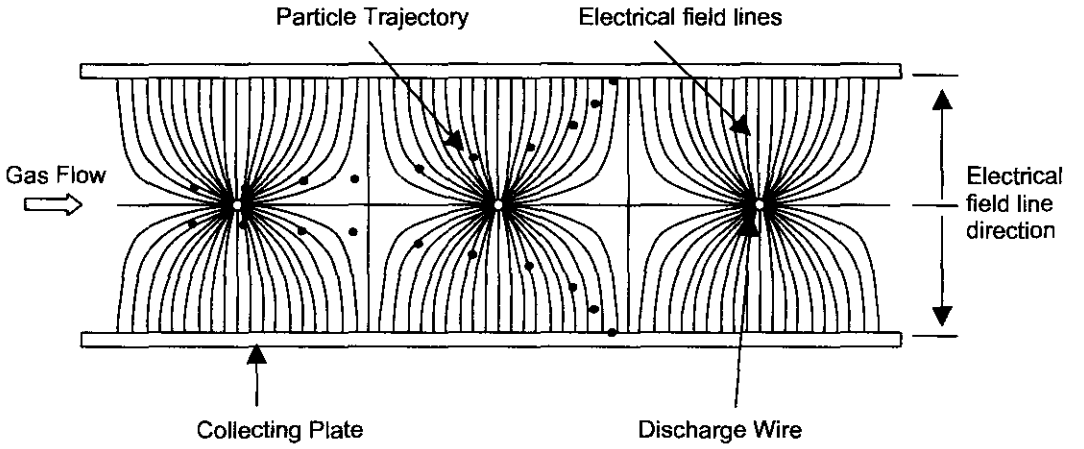

Figure 1.4: Electrical Field Lines.

space between the electrodes and collecting plates influence the electric field. At light dust loads, the space charge effects can reduce collecting efficiency and cause corona quenching. The resistivity of the fly ash can also distort the electrical field. The characteristics of the burned coal determine the resistivity of the fly ash. High resistivity ash can cause back corona on the collecting plates, which will reduce the number of charged particles. Back corona can also cause particles to be re-entrained into the gas stream. Low resistivity ash can easily be charge by the electric field and quickly be discharged when it hits the collecting plates. This can also cause re-entrainment of particles into the gas flow.

1.6.3 Particle Dynamics

The electrical forces exerted by the electrical field, and the drag forces exerted by the fluid flow, influence the trajectories of the particles in the gas stream. The purpose of the fluid flow is to transport the particles through the ESP and the purpose of the electric field is to charge and collect the particles. The rate of particle collection is proportional to the Coulomb forces acting on the particles. The Coulomb forces in turn, are a product of the particle charge and the electric field intensity. In practice two different rapping systems are used to loosen the dust cakes on the collecting plates. The first works with a hammer mechanism that strikes the plates and the second works with a vibrating system that continuously vibrates the plates. The rapping system can also reduce collection efficiency when dislodged particles are re-entrained into the gas stream.

1.7 Problem Definition

Large industries like SASOL have a large effect on the environment. The emissions of these industries without proper control can have a detrimental effect on animals, plants and humans alike. The purpose of the engineers and designers are to develop and improve equipment to reduce air pollution levels to a minimum. Extensive research and experimental tests were done throughout the years to better understand and improve electrostatic precipitation. However, with growing environmental concern the process must be further enhanced and optimised. The computer revolution also opened new doors for research on electrostatic precipitation. The gas flow through an ESP can determine the collection efficiency. The gas flow is also one parameter that can easily be manipulated by vanes, ducts, baffle plates, etc. in order to achieve better ESP performance.

1.8 Scope of study

This study consists of a literature survey discussing most relevant aspects that influence ESP efficiency. The study includes the development of a CFD (Computational Fluid Dynamics) model to simulate the fluid flow through a SASOL ESP. A commercial CFD code (Flo++) is used to assist in the ESP simulation. The numerical model only considers the flow of the gas through the ESP. Because of the limitation imposed by the computational resources, no electrostatic conditions will be considered. The complexity of the model is also limited because of the large size of the ESP. The model can be used to investigate the inlet conditions, the gas distribution and the outlet conditions. This information can then be used to draw certain conclusions and to make recommendations concerning the gas flow through the ESP.

1.9 Description of Chapters

A short description of every chapter is presented below:

Chapter 2: Literature Survey.

The literature survey is presented. Aspects like ash resistivity, pulsed energization, ESP geometries, back corona and secondary flows that influence ESP performance are discussed. Other topics like ESP modelling and experimental works also form part of this chapter.

Chapter 3: Theory.

The basic mathematics and theories of fluid dynamics through an ESP are discussed. Fundamental equations and physical properties used in the numerical model are explained. The solution methodology employed is also explained.

Chapter 4: ESP Model.

The development of the CFD model is presented. The flow domain of the numerical model is identified according to the ESP geometry. The limitations, assumptions and boundary condition of the model also form part of this chapter.

Chapter 5: Results.

The CFD model is used to generate results. The validity and the effects of the results are discussed.

Chapter 6: Conclusions and Recommendations.

Conclusions and recommendations are made concerning the results obtained by the ESP model.

CHAPTER 2

2. Literature Survey

2.1 Introduction

The first chapter discussed the background and the basic operation of an ESP. The following chapter contains the highlights of previous work conducted on the process of electrostatic precipitation. Various experimental and modelling studies were done in order to understand the process better and to improve ESP design. During the past few years ESP modelling was done with numerical methods because of the complexity of the process and the interaction between the various mechanisms.

This survey includes the research of different modelling techniques and factors that influence ESP performance. The influences of ash resistivity, ESP geometry, secondary flows, pulsed energization and back corona on collecting efficiencies are discussed. The chapter will start with a short background on the origin of electrostatic precipitation.

2.2 Historical Origins

The Greeks knew of electrostatic attraction of small amber particles as early as 600 B.C. The investigation of Coulomb in 1785 to 1789 and his discovery of the inverse square law form the basis of electrostatics (White, 1963: 3). The first recorded work regarding electrical attraction of smoke was in 1600 by Gilbert. The studies of Sir Oliver Lodge in 1884 resulted in the first attempt to apply electrostatic precipitation commercially at a lead-smelting factory. The electrostatic device failed in its purpose due to the primitive method of producing high-voltage electricity and the insulating character of lead fume. More research was done on electrostatic precipitation between 1885 and 1903 but never evolved into something more than a laboratory experiment. The groundbreaking work of Cottrell between 1903 and 1910 led to the first

working industrial precipitator. In 1906 Cottrell used a synchronous mechanical rectifier in order to obtain high-voltage discharges. However, the maximum voltage was limited to values between 10kV and 15kV. (Modern ESPs function at 40kV) The success of these experiments led to the installation of the first large-scale industrial precipitator near California in 1910. The precipitator was adequate for its purpose, but many aspects needed improvement. However, the precipitator's efficiency was calculated to be between 80 and 90%. After the success of the precipitator, Cottrell's process was adopted and the process of electrostatic precipitation became a reality (White, 1963: 4).

2.3. Previous work

During the last century various theoretical and experimental research was conducted on electrostatic precipitation. At the beginning of the century Deutsch developed the first ESP model (De Nevers, 1995):

$$\eta = 1 - \exp(-(w_m A)/Q) \qquad (2.1)$$

where η is the collecting efficiency, w_m the migrating velocity, A the collecting area and Q the volumetric flow through the section. The migration velocity is the velocity component of the ash particles perpendicular to the collecting plate.

This model is very limited because of drastic idealized assumptions made, but is still used today as a basis for ESP design. In order to improve the model various researchers developed certain factors to incorporate aspects like re-entrainment, turbulent mixing, back corona, etc (e.g. Zhibin & Guoquan, 1994; Hao *et al.*, 1990; Leonard *et al.*, 1980). The development of numerical methods enabled researchers to better understand electrostatic precipitation and to develop more accurate prediction models, which is based on fundamental laws. The rest of this chapter will focus on research done on ESP modelling and on aspects that influence ESP performance.

2.3.1 ESP Geometry

The internal ESP geometry does not only determine the gas flow and gas distribution through the precipitator. It also plays a very important role in the intensity and electrical field distribution around the discharge wires. Thus, aspects like electrode geometry, plate-to-wire and wire-to-wire spacing strongly influence ESP performance.

Jedrusik *et al.* (2001) investigated ESP efficiency using different electrode geometries and particle sizes. Barbed plates, barbed tubes, wires and spiked bands geometries were used in an experimental scale precipitator (Figure 2.1). A glass precipitator was used in their studies, by this means they could visualize the trajectories of the solid particles and they could measure their velocities. The migration velocity determines the collection efficiency of solid particles in an ESP. The barbed tube electrode showed a tendency to increase the migration velocity with an increase in particle diameter and applied voltage. This increase in migration velocity seemed to offer the best geometry of all the electrode geometries tested.

Kim & Lee (1999) conducted a series of experiments on a laboratory scale single-stage ESP, in order to identify the operation conditions for maximum collection efficiency. They also investigated the influence of particle contamination at the discharge electrode and the collecting plates. The wire-to-plate spacing, wire-to-wire spacing, the airflow velocity, the turbulence intensity and the discharge electrode diameter were investigated during their studies. The results showed that an increase in wire-to-plate spacing causes

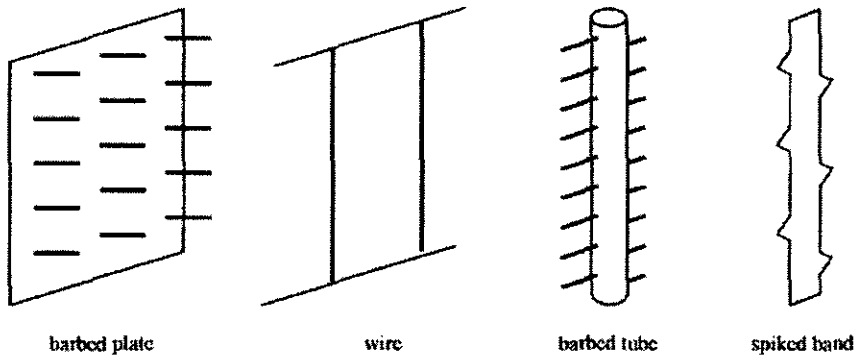

Figure 2.1: Four different electrode geometries used. (M. Jedrusik *et al.*, 2001)

a decrease in collection efficiency. The results also identified the important influence of wire-to-wire spacing on ESP efficiency. The optimal spacing for this laboratory scale precipitator was determined at 37.5mm. As the flow velocity increased the collection efficiency decreased. This is because higher flow velocities reduce the treatment time of the dust particles inside the collecting duct, resulting in poorly charged particles. The results also showed that turbulence affects the efficiency at low electric field regions, but at high field regions the efficiency is not significantly affected. An increase in discharge wire diameter caused a decrease in ESP efficiency. The corona will decrease as the wire diameter increases for a constant applied voltage. Weaker corona power will result in lower collection efficiencies.

Miller *et al.* (1998) used an experimental ESP to determine the influence of barb length, barb distance and the distance between the corona electrodes on the effectiveness of electrostatic precipitation. Secondary flow is an important factor in the collection of small particles. The formation and intensity of the secondary flow strongly depends on the current density distribution and therefore on the electrode and collecting plate geometry. Longer and sharper barbs produced higher currents than short and sphere point barbs. Efficiency measurements were also taken with different number of barbs on the discharge electrode. Figure 2.2 show how the number of barbs were varied between 3 and 15.

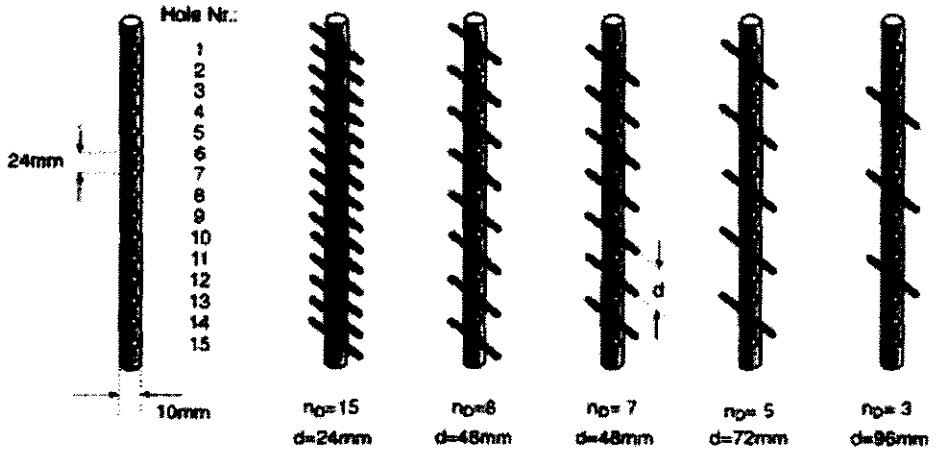

Figure 2.2: Different barb distances used. (J. Miller *et al.*, 2001)

The I/V (Current/Voltage) curves showed an increase in current as the number of barbs increased, 15 barbs showed 50% higher currents than 3 barbs. The tests also showed that an electrode with 8 barbs and 15 barbs deliver almost the same efficiency. Thus, in conclusion can be said that the optimum distance between barbs is about 50 mm. The results showed that the optimum electrode distance is equal to or smaller than half of the collecting duct width. The optimum settings, identified by the experiments, showed uniform and low current levels, which limits the development of back corona.

2.3.2 Ash Resistivity

The characteristic of fly-ash that influences the efficiency of an ESP the most is the electrical resistivity. Fly-ash electrical resistivity can be defined as the ability for an ash particle to accept an electrical charge. The worst problem with ash resistivity is the development of back corona.

According to Tulsa (1998) enhanced ESP efficiencies can be gained through fluid-catalyst cracking (FCC) units by lowering the catalyst (fly-ash) resistivity. Tulsa describes the ESP mechanism through Ohm's law:

$$V_{plate} - V_{catalyst} = I_{plate} * R \tag{2.2}$$

The resistance is a function of the catalyst resistivity:

$$R = (r * L)/A \tag{2.3}$$

where r is the catalyst resistivity, L is the thickness of the catalyst layer collected at the plates and A is the total surface area of the collecting plates. Combining equations (2.2) and (2.3):

$$I = (V_{plate} - V_{catalyst})A/r * I \tag{2.4}$$

It can be seen that smaller resistivities will result in larger currents, thus increasing the ESP efficiency. This study showed that the use of contaminated metals in combination with high temperatures has the largest influence in lowering resistivities. Ammonia injection can also improve resistivity levels. In one case the efficiency of an ESP was improved from 96% to 98%.

Navarrette *et al.* (1997) used a pilot precipitator to investigate the influence of plate spacing and ash resistivity on ESP performance. Two different plate spacing were used, 300mm, which is the value mostly found in commercial precipitators, and 400mm which are the most up to date tendencies among designers. Two different types of coal were used, a high resistivity coal and a low resistivity coal. According to the study the voltage decrease caused by the ash layer on the collecting plates is given by:

$$V_r = \rho_r j\, e \qquad (2.5)$$

where ρ_r is the electrical resistivity of the layer, j is the density of the electrical current that cross the layer and e is the thickness of the layer. This voltage decrease causes deterioration in the corona discharge of the electrodes, thus high resistivity ash causes lower ESP efficiencies. The high resistivity coal showed best results with the 400mm plate spacing, the 300mm plate spacing showed lower efficiencies with every test done. The low resistivity coal showed better results with 300mm plate spacing than with the 400mm plate spacing.

Schmidle *et al.* (1995) showed, by using a laboratory ESP, that the collecting efficiency was strongly dependant on the ash resistivity. They showed that low resistivity fly ash leads to loose dust cakes, favouring re-entrainment and to high resistivity weakens the electrical field in the collecting ducts. High resistivity ash layers on the collecting plates produce ions with opposite polarity than the corona. This results in the neutralizing of the particles and prevents them from being precipitated. These electrical discharges and the increase of current in the ash layer indicate back corona. The deteriorating effect of high resistivity ash can be limited through techniques like thermal treatment and pulsed energization.

Bibbo (1995) investigated gas conditioning as an effective method to reduce ash resistivity levels, in order to obtain the optimal conditions for efficient ESP operation. A new SO_3 gas-conditioning process was researched and developed called EPRICON. During combustion of coal in the boiler a small fraction of the SO_2 produced is converted to SO_3. The SO_3 is then

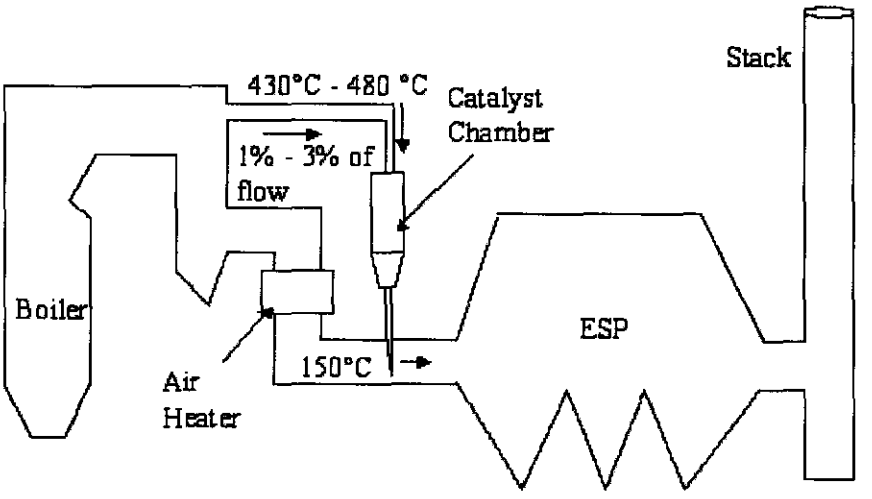

Figure 2.3: EPRICON Process

absorbed on the surface of the fly ash, resulting in lower ash resistivities. However, the SO_3 developed naturally may not be enough to reduce the resistivity levels in order to obtain efficient ESP performance.

The EPRICON process (Figure 2.3) works by extracting a small fraction of the flue gas from the boiler. This fraction of the flue gas is then passed over a catalyst, heated by the gas. In the catalyst chamber 30% to 70% of the SO_2 in the flue gas is converted to SO_3. The slipstream, now SO_3-rich, is re-injected ahead of the ESP to provide the required reduction of resistivity. The EPRICON system was installed in two precipitators. The resistivity of the fly ash was not directly measured, but the ESP power levels were monitored with and without the EPRICON system. The change in ESP power was significant and showed a strong relationship between the EPRICON system and the corona power. The total ESP power was increased by 200%.

2.3.3 ESP Modelling

The interaction between the electric field, the fluid flow and the particle flow is very complex. The complexity of the process increases the difficulty in developing an accurate prediction model. Scientists and engineers researched various methods to develop accurate ESP simulation models. Some models use a coupled system to accurately describe particle movement in the collecting duct. These models are complex in nature and three-dimensional simulations are not commonly found. Uncoupled models usually

concentrate on the gas flow distribution through the ESP and three-dimensional simulation is occasionally used. Extensive research was also conducted to incorporate turbulent flow effects into ESP models.

Varonos *et al.* (2002) developed a method to optimize the existing precipitators with minimum cost. This method was applied on a full-scale industrial precipitator operating in a power station unit. The fluid flow was simulated as three-dimensional, which increased the complexity. The Navier-Stokes equations along with the $k-\varepsilon$ turbulence model were solved using the finite volume method. A Lagrangian approach was used, in which the particle trajectories were calculated and monitored until collection or escape in the atmosphere occurred. This gave an accurate prediction of the ESP efficiency. The main objective of this study was to minimize the re-entrainment losses of industrial ESPs. This can be achieved through aerodynamic optimization of the velocity profile at the inlet of the ESP. The use of smoothing grids and "flaps" were investigated as two methods to improve the gas distribution at the inlet. The original design showed a highly non-uniform velocity profile and it was skewed in the wrong direction. The reason for the poor aerodynamic quality of the flow was the sudden expansion in the geometrical configuration at the inlet of the ESP and the blockage caused by the vertical plates. The results of the numerical insertion of five smoothing grids showed a 44% reduction in emissions, in comparison to the original operating conditions. The collecting areas on plates were also wider and smoother, with an important section of them extended to the lower parts of the collecting plates. The smoothing grids gave a uniform velocity profile (Figure 2.4), which lead to an enhanced efficiency. The insertion of three numerical "flaps" in the sudden expansion area at the inlet of the ESP showed that the main part of the flow passed through the lower section of the collecting area. The velocity profile was, however not uniform. Thus smoothing grids are the more efficient choice for optimising the gas flow. The results of the numerical model were in good agreement with experimental data.

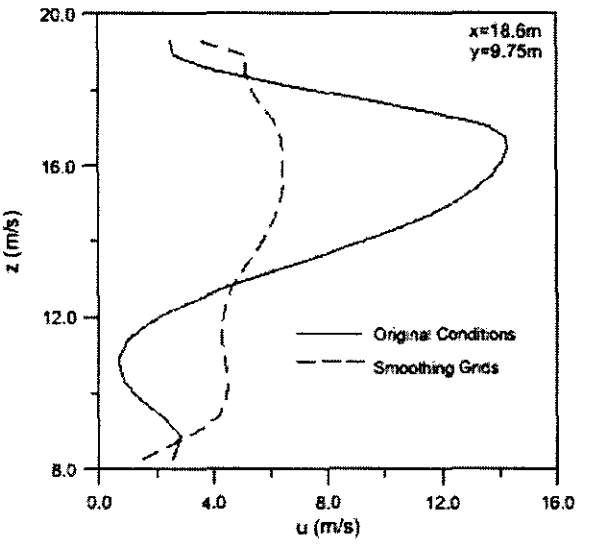

Figure 2.4: Velocity profile with and without smoothing grids. (Varonos *et al.*, 2002)

Kogelschartz and Edgar (2001) described an advanced numerical model that improves the understanding of the processes taking place inside a precipitator. The aim of their study was to develop a three-dimensional model to accurately predict the dust particle trajectories inside an ESP. The model used different software packages and workstations that were linked in order to obtain the best simulation. A three-dimensional model was required because the modern precipitator that was simulated used helical electrodes. The helical shape of the electrode has some important advantages in that it forces a well-defined current density distribution in the duct. This stable current density distribution makes the helical electrode geometry superior to other electrode shapes. The electrodes are like springs mounted under tension and this provides a self-centering action. The vibrating characteristics of these spring-like electrodes also enhance the rapping process. They found that the spacing of corona electrodes must be optimized in connection with the shape of the collecting plates. This has a strong influence on the ion distribution and the current density. Two mechanisms are responsible for the charge accumulation on the dust particles. Bigger particles (> 1 μm radius) are charged through a process called "field charging". Field charging drives the ions to the particle surface until a saturation charge is reached (depending on particle size and electrical field strength). As the particle is being charged it

repels more and more ions, and when all the ions are repelled the saturation charge is reached. Smaller particles are charged through a process called "diffusion charging". This process depends on the random thermal motion of ions and the resulting collisions with dust particles. Field and diffusion charging takes place at the same time inside the precipitator. The results of the model showed that best ESP efficiencies were gained with particles of a 0.5 μm diameter and when electric wind was limited. The electric wind (also known as corona or ionic wind) is generated through the ions that travel from the discharge wire to the collecting plates at velocities of about 100m/s. The results were in good agreement with measurements from a full-scale precipitator.

Kruger (1999) presented a numerical model that investigated the electrohydrodynamic conditions inside a wire-plate electrostatic precipitator. The finite volume approach was used for the electrostatic and fluid dynamic conditions. Using a Lagrangian approach, the particle dynamics were solved. Kruger used an algorithm that contains sub algorithms for the electrostatics, fluid dynamics and particle dynamics models. The model was implemented into a commercial finite volume software package called Flo++ (Le Grange, 1999). The numerical results were validated with analytical solutions and compared with experimental measurements. Good agreement for the stream wise profiles was obtained, but the measured velocities exhibited a much larger transverse component than the numerical results. This discrepancy was because of the isotropic nature of the $k-\varepsilon$ turbulence model. The coupling between electrostatic and fluid dynamic models did enable the prediction of ionic wind effects.

Gallimberti (1998) described a mathematical model for the simulation of the operating conditions of large-scale ESPs. The numerical model describes the relevant mechanical, electrical, physical and chemical processes that are involved in the transport, charging, migration and collection of fly ash. Each process (corona discharge, particle charging, particle collection, rapping, re-entrainment) has its own mathematical model based entirely on the

relevant physical laws. The complete model consists of several modules, which exchange information, thus resulting in a more detailed simulation. The model layout is shown in Figure 2.5. The finite difference method is used with separate grids for each section or module. A three-dimensional simulation of the fluid dynamics through a whole precipitator was conducted. The precipitator contained distribution plates, with calibrated holes, at the ESP inlet in order to ensure uniform gas flow through the main body. The first simulations showed that the flow distribution in the main body was far from being uniform, causing a low efficiency. The non-uniform gas distribution was caused by a sharp bend at the inlet of the ESP. The following simulations were done with different hole positions and hole calibrations on the distribution plates. This was done in order to control turbulence and re-circulation losses, thus improving the ESP efficiency.

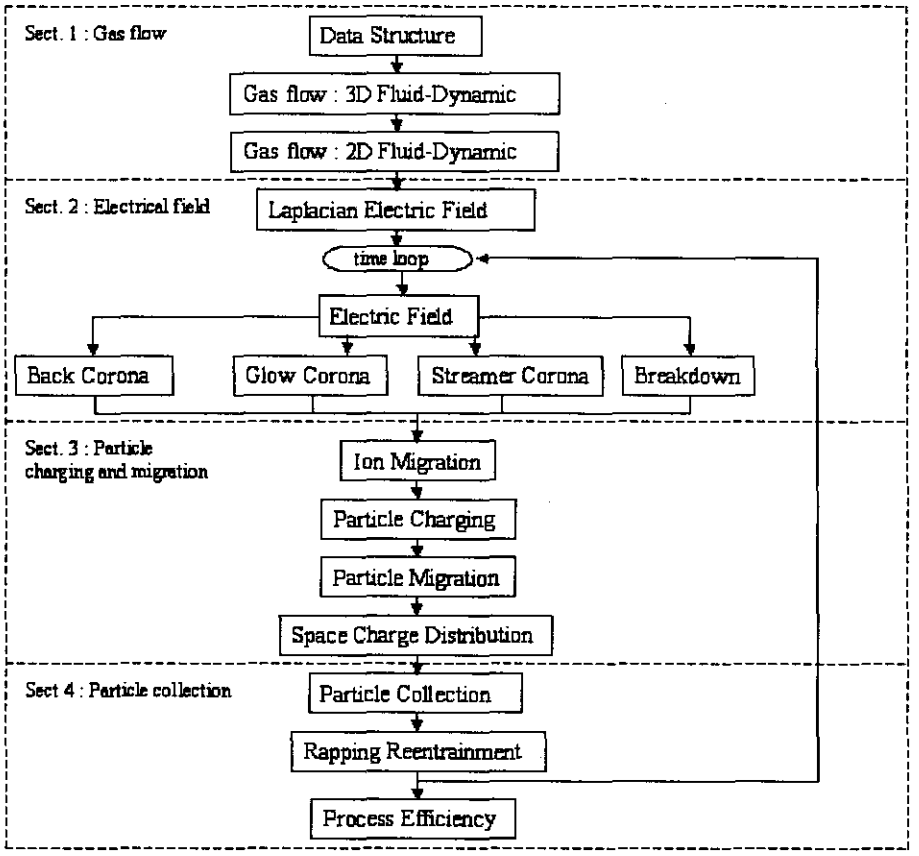

Figure 2.5: Flow-chart of ESP mathematical model. (Gallimberti, 1998)

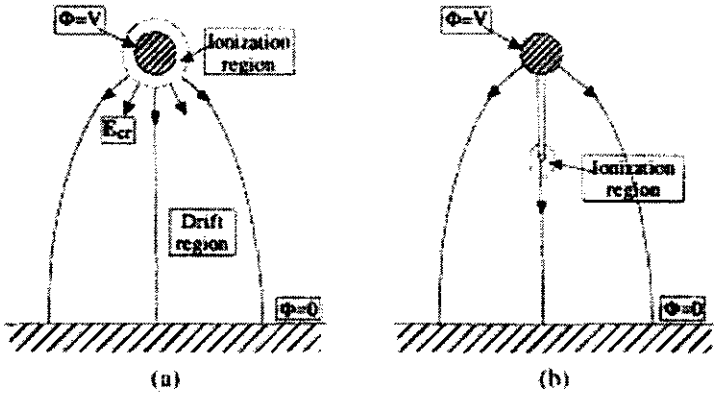

Figure 2.6: Corona discharge types: a) Glow corona b) Streamer corona (Gallimberti, 1998)

Glow and streamer corona are the two types of corona discharges observed in ESPs. The model verifies which form of corona discharge is more active and calculates the ionic charge input. Figure 2.6 explains the mechanism of glow and streamer corona. Glow corona is confined in a small region near the high-voltage electrode, where the ionisation processes occur in the from of electron avalanches. Streamer corona is formed by a large number of branched filaments developed from the discharge electrode into the high field region. At the tip of the filaments the ionisation area is formed. Glow corona is dominant with continuous or slow charging voltage operations and streamer corona is more dominant with impulse voltages. The particle migration module simulates the particle motion; it takes into consideration all the forces applied on the particle (viscous, electrical and gravitational) and the process of charging exchange and turbulent diffusion. The particle migration model uses a mixed Eulerian-Lagrangian method to determine the velocities of the particles.

Choi & Fletcher (1997) used strong coupling of the governing equations to accurately predict the particle motion inside an ESP. A finite volume approach was used to solve both the turbulent fluid flow and the electrical conditions. They also showed the importance of particle space charge effects on ESP efficiency. Particles close to the wire are highly charged and move toward the collecting plate. Particles far from the wire drift downstream because they have less charge. This results in particle trajectories that

frequently cross and form a high mass concentration banded area. This band distorts the electric field and reduces the Coulomb forces. This means that the efficiency of an ESP can be over-predicted when particle space charge effects are neglected. Small particles contribute more to particle space charge and the corresponding distortion of the electric field, than large particles. This is because particle charge density depends on the total surface area, and smaller particles provide a larger total surface area for a given mass flow.

Meroth (1997) used a coupled method in order to show the influence of ionic wind on particle movement. A finite element solver was used for the Poisson equation coupled with a finite volume scheme for the conservation equations of the electric current, in order to calculate the Coulomb forces. This result was then applied as a volume source in a finite volume solver for the fluid flow. The FMD (Field Modified Diffusion) model was used to calculate the charging mechanism. The model consists of two parts: One part for the field charging (for large particles) and the other for diffusion charging (for small particles). An Eulerian/Lagrangian approach was used to compute the particle motion. The results showed that larger particles are accelerated more towards the collecting plates than small particles. This is because the larger particles are more highly charged and obeys larger inertia forces. The computational speed of the model was much faster than traditional models and flexible regarding physical geometries.

Gas distribution over the cross section of each precipitation field strongly influences ESP efficiencies. Each area with higher gas velocities than the average velocity values will lower the collection efficiency. Vortices and backflow patterns within the ESP field must be avoided under all conditions. Leibacher (1996) used CFD (Computational Fluid Dynamics) software to predict turbulent gas flow patterns inside an ESP. The results can be used to improve the airflow inside the ESP and thus ensuring higher efficiencies. The software (FLUENT) uses an Eulerian multiphase model with a fully coupled gas-dust model to accurately predict the gas flow. The electrostatic forces were neglected and the focus of this study was primarily on the gas flow

through a precipitator. Low dust concentration and high dust concentration were investigated and compared with actual measurements from a real ESP. Baffle plates were used at the inlet to ensure good gas distribution inside the ESP. The low and high dust concentration models showed good correlation both qualitatively and quantitatively with experimental data.

Kim & Lee (1999) used a laboratory scale precipitator to evaluate different theoretical models in order to identify the most accurate ESP model. The results from the experiments were compared with the Deutsch, Cooperman, Leonard and Zhibin & Guoquan models. The Deutsch model assumes complete mixing by turbulent flow and thereby uniform concentration profiles. To avoid this drastic assumption of infinite diffusivity, finite diffusivity models were developed with the convective-diffusion equation and various boundary conditions. An example of such a model is the Leonard model. He assumed uniformity of the velocity components of the charged particles and particle diffusivity. This model did not accurately describe the particle diffusivity near the collecting plates, where it is significantly lower than in the turbulent core. Cooperman's model is similar to the Deutsch but it accounts for the effect of turbulence and particle turbulent diffusion. However it did not estimate the effects of re-entrainment and particle diffusivity. The model by Zhibin & Guoquan takes into account the effects of turbulent mixing by electric wind. Different ESP geometries, velocities and particle sizes were experimentally investigated. The Zhibin & Guoquan model exhibited the best comparison with the measured results for every test done. This model was also identified as the best prediction model.

Different types of discharge electrodes (star-shaped, saw-tooth spike and tube-type spike) and collecting plates are used, in order to improve collection efficiencies. The effect of discharge electrode shape on the electric field strength distribution is only second to the applied voltage. Hao *et al.* (1990) developed a method to generate a correctional wire diameter. The field strength distribution for different shape discharge electrodes can be calculated directly by the same methods used for conventional wires, but with the correctional wire diameter identified for the specific shape of electrode. The

correctional diameter of a discharge electrode (star-shaped, saw-tooth spike and tube-type spike) is the diameter of a wire electrode whose voltage-current characteristics under the same conditions approximate that of the discharge electrode. It was found that a diameter of 0.8 mm approximates a saw-tooth spike electrode and a diameter of 2.7 mm for the star-shaped electrode. The results with the correctional wire diameter were in good agreement with experimental results. This method was also used to predict the performance of four full-scale ESPs. The results showed that the approximation techniques are sufficiently accurate.

Turbulence modelling:

Zhibin and Guoquan (1994) improved their previous ESP model by introducing turbulent mixing into the model. This was done by incorporating turbulent mixing coefficients into the efficiency equations. The convection diffusion model was used for charged particles transport and was incorporated into the collection efficiency formula. The turbulent mixing coefficient is a representation of the effect of turbulence on particle transport. This coefficient was directly developed on the basis of mass transfer, Navier-Stokes and Shaughnessy equations. Turbulent mixing depends mainly on fluid mechanical parameters of turbulent flows with corona wind, the local electric conditions and the particle size. The results of the improved model were compared with experimental data and with the Deutsch model. The turbulent mixing model and the Deutsch model were in good agreement for particles larger than 1 μm but the presented model was closer to the measured data for smaller particles.

Soldati *et al.* (1993) used direct numerical simulation (DNS) with a pseudospectral method to solve the Navier-Stokes equations. Through this method the transport of particles in turbulent flows under the action of different electrostatic fields can be simulated. The results from the simulated turbulent flow field were qualitative and quantitative in very good agreement with experimental results. The coupling of the electrostatic field and the turbulent flow was neglected during this study. However, Soldati *et al.* (2000) used the

same approach to show the effects of secondary flows on particle collection. Given the characteristics of this method for performing the simulations, individual particle positions could be monitored at each time step. It was noted that the profiles showed that turbulent diffusion plays an important role in the deposition process. The migration velocity decreases as the particle collection proceeds. It is believed that this decrease is because of wall-generated turbulence. The turbulence intensity is higher (because of the bulk flow) at the wall and the particles are more affected by turbulent diffusion in this area. This turbulence tends to push the particles away from the plate toward the electrostatic drift, which tend to push the particles toward the plate. The consequence of this interaction is a decrease in migration velocity, resulting in a lower efficiency.

Leonard *et al.* (1980) conducted a study to develop a model that predicts more accurate ESP efficiencies than the Deutsch model. It was found that measured ESP efficiencies were much higher than those predicted by the Deutsch model. This suggested a deficiency in the Deutsch model, thus a more exact prediction model is needed. This could lead to smaller precipitators with the same efficiencies predicted by the Deutsch model. In this study transport of particles due to the combined effects of mobility and eddy diffusion in the gas flow were investigated. The convective diffusion equation was solved analytically for monodisperse particle concentration, as a sum of normal nodes that can represent any entrance profile. The Deutsch model assumes a constant concentration profile in the collecting duct. This means that the mass flux to the wall is also constant. For a non-zero Peclet number the concentration is higher at the walls than in the centre. This means that the flux to the walls is actually larger than predicted by the Deutsch model. The most significant conclusion is that the gas flow quality is a crucial factor in ESP performance. It was also indicated that the Deutsch efficiency is not the theoretical maximum that can be expected, but much higher efficiencies and migration velocities should be possible if good flow quality can be engineered. If efficiency measurements are lower than the Deutsch values, it indicates either poor gas flow quality or that there are

unrecognised major effects degrading the performance (re-entrainment, back corona, sneakage, etc.).

Alternative modelling techniques

Ramsdell (1968) presented a paper, describing design criteria for electrostatic precipitators. Ramsdell's criteria consist of certain curves; the first is called the "Ramsdell Equation" and shows the relationship between ESP efficiency and an active bus section. An active bus section refers to a separately energized precipitator field where a transient electrical disturbance in a given section, is not reflected in any other section. This curve was then used to develop a second curve that showed the relationship between efficiency and collecting area. Low-sulphur ash has a high resistivity and is collected with difficulty. A third set of curves was developed that show the relationship between efficiency and sulphur content. The gas velocity inside a precipitator is also a major factor that influences efficiency. A lower velocity creates more treatment time for the fly ash to be collected and the re-entrainment losses are also smaller. Ash with high resistivities (low sulphur content) is not so easily collected, thus lower sulphur coals require lower gas velocities.

Hati & Singiresu (2001) used a procedure, based on the concept of game theory, for the optimum design of an air pollution control system. The problem was formulated as a four-criteria optimisation problem. The four objectives of the optimisation study were the cost of the precipitator, the cost of the stack, the maximum ground-level concentration of particle matter and the maximum ground-level concentration of sulphur dioxide. The efficiency of the ESP and the stack height were treated as the design variables. The objective of their study was to develop a strategy for a pollution control system that would provide an optimal trade-off between the costs of the system, the efficiency of the precipitator and the stack height. A game is defined by the actions of a set of players (objectives) who act according to their own strategies to maximize their individual gains. If the players act independently without cooperating, the game is called a non-cooperative game and the solution is called a Nash Equilibrium Solution. In a cooperative game the players work together with the idea that the outcome of the solution will be better than the

Nash solution. The solution of the game theory included the Nash and the cooperative solution and was used to solve the design problem.

Many prediction models used today are limited and only valid under certain conditions. The interaction between the gas flow and the electric field and the effects of non-ideal parameters (sneakage, re-entrainment, back corona, etc.) are the most difficult to simulate. Kiss & Berta (2001) developed a model, which uses existing ESP models as the primary ones, but also use fuzzy logic to handle the uncertainty of the parameters and to take the non-ideal factors into consideration. The idea of fuzzy logic is to evaluate and extend the capabilities of existing ESP models. The aim of fuzzy logic can be divided in two. Firstly it is used to evaluate the reliability of the given model, when there are uncertain parameters among the input values. Secondly it can be used to change the output quantities in such a way that they get closer to the real values.

2.3.4 Secondary flows

The electrohydrodynamic (EHD) interaction between the corona discharge and the gas flow can produce disturbances. The ions streaming through the gas stream exert body forces on the gas molecules, which results in secondary flows and turbulence. Well-organised secondary flow, shown in Figure 2.7-a, is present with uniform positive discharges. In the barbed-wire precipitator the recirculation vortices move transverse to the main bulk flow, shown in Figure 2.7-b. The wire spacing, gas flow and barb spacing determine the vortex structure. Figure 2.7-c illustrates that at low gas flow velocities an individual discharge spot will create an elliptical shaped vortex (Yamamoto and Sparks: 1986).

Mizeraczyk *et al.* (2001) used particle image velocimetry (PIV) to instantaneously measure the flow field velocity and to investigate the secondary flows in a laboratory scale precipitator. PIV is based on the scattering of laser light on the particles following the flow. The laser "sheet" of 1mm thickness was set along the flow direction, perpendicular to the collecting plates. The flow inside the collecting duct, with no voltage applied,

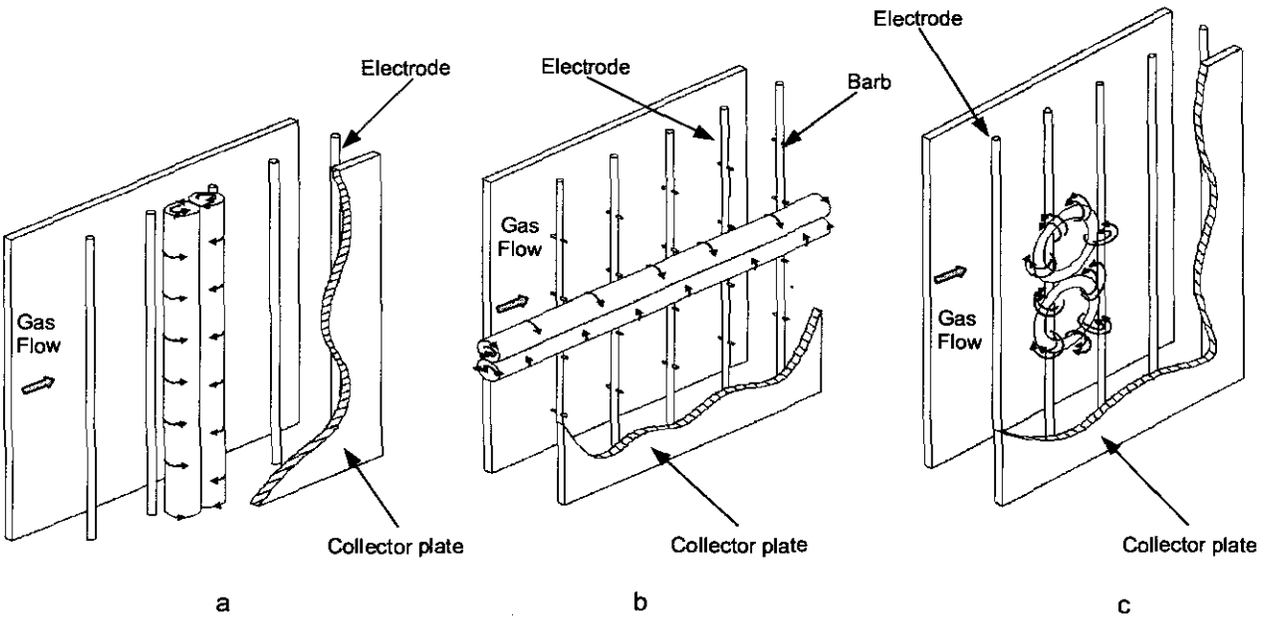

Figure 2.7: Secondary flow in an ESP: a) Secondary flow in a positive discharge precipitator with smooth wires. b) Secondary flow in a negative discharge precipitator with barbed wires. c) Negative tuft discharges.

was almost laminar and without turbulence. After applying a voltage the flow became very turbulent and changed significantly. The results from the PIV showed the gas flow from the discharge electrode towards the collecting plates, the reversed flow and the large vortices, resulting from the upstream direction of the flow. The secondary flow and the resulting vortices were more pronounced with positive polarized electrodes than with negative polarization. The investigations of the near-collecting plate region showed the importance of secondary flows in the collection of fine particles.

Soldati (2000) used a direct numerical solution (DNS) to examine the behaviour of particles in the flow field resulting from the interaction between EHD flows and the turbulent flow through a precipitator. Particle trajectories showed that the EHD flow contributed to particle re-entrainment but also sweeps particles toward the wall, thus having a negligible influence on the efficiency. This was verified by comparing the present simulation with other simulations in which the electrostatics acted only on the particles and not on the flow field. It was concluded that particle deposition is scarcely influenced

by EHD flows, and rather strongly dependent on the distribution of the electrostatic field near the wall. This means that more time, research and effort must be placed on other factors like gas distribution, ESP geometry and sufficient optimal power supplies, in order to enhance ESP efficiencies.

Altering the structure of the geometry-dependent electric body force acting on the gas flow can control EHD flows. Large-scale current non-uniformity is the source of large-scale vorticity and fluid mixing. An alternative electrode that reduces the length scale of the discharge non-uniformity may reduce these deteriorating effects. An example of such an alternative electrode is a barbed-plate electrode. Davidson & McKinney (1991) did experimental studies on a laboratory-scale ESP, in order to investigate EHD flows in wire-plate (Figure 2.8-a) and barbed-plate (Figure 2.8-b) precipitators. Flow visualization was used for their research in EHD flow patterns. The current-voltage characteristics for the wire-plate geometry showed higher corona onset values than for the barbed-plate geometries. EHD flow can be seen as a series of corona wind jets moving transverse to the main gas flow, originating from individual discharge spots. The jet velocity depends on the current level of the

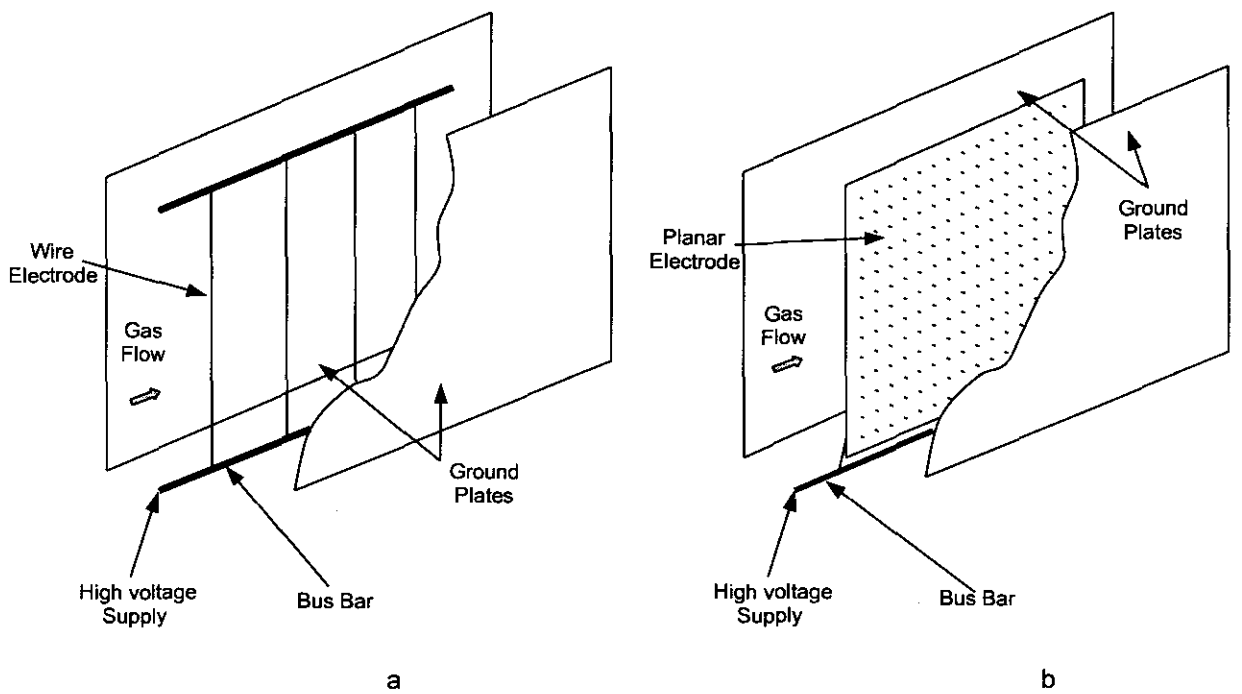

Figure 2.8: a) Wire-plate ESP b) Barbed-plate ESP

discharge spot. The jet shape is determined by the discharge point distribution. All the geometries showed that corona onset causes an obvious increase in vorticity and turbulent mixing. For the wire-plate ESP the developed EHD flow was almost similar to that predicted (Figure 2.7-a). The barbed-plate geometry showed the desired effect of reducing turbulent mixing relative to the conventional wire-plate design. This may lead to an increase in the ESP collection efficiency. The barbed-plate design distributes the current more evenly in the flow duct, thus reducing the scale of the electrically induced fluid motions.

Leonard *et al.* (1983) performed extensive experiments to obtain an understanding of how secondary and turbulent flows are generated by corona discharge and how these effects influence ESP efficiency. Schlieren visualization and laser-anemometry results were obtained and compared with other experimental results. Perpendicular to the corona wire, the flow separates from the wall upstream of the wire and reattaches downstream leaving regions of recirculation flows opposite the wires near the wall (Figure 2.7-a). The studies showed that the flow was non-turbulent in the core of the flow. This was confirmed with smoke-wire visualization techniques and showed the generation of streamwise vorticity in the corner near the precipitator end walls. The hot-wire measurements demonstrated, that for positive corona discharge no turbulence was produced aside from the end walls turbulence. Smoke-wire visualization showed vortical motion induced near the tunnel end walls (Figure 2.7-b). Negative corona discharge showed that the level of turbulence intensity in the core of the flow increased when the mean gas velocity was less than 2 m/s. No change in the turbulence intensity was observed with velocities higher than 2 m/s. It was concluded that the level of corona-induced turbulence is significantly smaller than that resulting from entrance ducting and the wakes of internal structures.

2.3.5 Pulsed energization

Pulsed energization is an alternative method to provide high voltage power to the collecting system. With impulse energization the voltage pulse produce the corona space charge and the continuous DC voltage is to ensure particle drift.

Macarie & Martin (1997) discussed the benefits of pulsed energization in the operating conditions of ESPs. In order to gain high collection efficiency, high migration velocities are necessary. The ESP voltage waveform determines the magnitude of the migration velocity. Pulsed energization also eliminates back corona, by the de-energizing before back corona can start and re-energizing when the voltage across the dust layer returns to the initial low level. The higher the dust resistivity, the longer the time period between the pulses must be. Pulsed energization not only enhances the ESP efficiency but the energy consumption can also be significantly reduced, which will lead to cost savings.

According to Dinelli *et al.* (1991) the means to restore the efficiency of ESPs in the presence of high resistivity ash is through SO_3 conditioning or impulse energization. Extensive experimental studies were done on impulse energization on a full-scale industrial precipitator. The precipitator was divided into two independent channels. The one channel "Reference channel", was operated with conventional energization (AC rectified voltage) and the second channel "Experimental channel", was operated with impulse energization. The efficiency of the reference channel and the experimental channel was found to be close, in the case with low resistivity ash, but the power consumption of the experimental channel was 20-30% lower. Impulse energization ensures efficiency values higher than 99.6% and prevents the inception of back corona. The enhancement factor of the migration velocity with impulse energization was about 1.5, with reference to conventional energization. Pulsed energization also showed great benefits in the collecting of fine particles. This is because of the higher peak voltage that can be maintained across the electrode structure for a sufficient time to provide the necessary charge and also allows better avalanche processes and streamer

penetration into the gas. (Impulse energization showed no development of back corona at peak voltages up to 70kV. Conventional energization showed the development of back corona at peak voltages of 37kV)

2.3.6 Back corona

Back corona is a violent energetic conversion of electrostatic energy to thermal energy that causes minor gas explosions. These explosions blow the ashcakes off the plates and make it impossible to collect these particles. Characteristics of back corona are a lower spark-over voltage, a higher current flow and lower collection efficiency. Back corona can begin to form at layer resistivities of about $2 \times 10^8 \Omega/m$.

Chang & Bai (1999) experimentally investigated the influence of back corona on the performance of a laboratory-scale single discharge wire-plate precipitator. Tests were done with dusts of different resistivities. Dust with moisture conditioning and dust without moisture conditioning. The results showed that flue gas conditioning by water injection could effectively improve ESP performance by reducing the effects of back corona. The conditioning by water injection effectively reduces the fly-ash resistivity. It allows the precipitator to operate under higher effective corona power, which results in a higher collection efficiency. It was found that the collection efficiency is proportional to the applied voltage. The voltage and power consumption decreased under constant current operation in the presence of back corona. The collection efficiency was found to be independent of the applied current. The experimental results showed that back corona has a large effect on the collection of sub-micron size particles.

Kim & Lee (1999) experimentally investigated ways to reduce back corona by optimising the rapping system. The experiments showed that after 300 min the collection efficiency was reduced from 95% to 80% because of the development of back corona. Two different rapping systems were investigated. A hammer mechanism that strikes the plates and a vibrating system that continuously vibrates the plates. The hammer rapping system

was investigated on its own first. The experiments showed that the rapping efficiency increased with an increase in time between raps. This is because the thickness of the fly-ash layer increases with time. The aggregating force of the deposited particles is strong enough for the hammer impact to separate the ash from the collecting plates and deposit it into the hoppers. Thin dust layers produce fine and light aggregates that can easily be re-entrained. Secondly the hammer system together with the vibrator system was investigated as an effective rapping system. The results showed that the rapping efficiency increased by 2-10%. This resulted in constant higher collection efficiency, which refer to a reduction in back corona.

2.3.7 Other effects

There are other minor aspects, which can also affect ESP efficiencies.

De Nevers (1995) explains spark-over and its effect on ESP performance. If the wire-to-plate distance is small enough and the voltage is high enough, then an ionised conducting path will be formed between the wire and plate. This ionised path is a good conductor and forms a continuous standing spark. The power supply must sense this sudden increase in current and stop the electric flow in order to prevent transformer burnout. These sparks are energetic and disrupt the ashcakes on the plates, thus reducing the ESP efficiency. Experimental results showed that low electrical field strength with no sparks also leads to low ESP efficiencies. Most ESP control systems allow about 50 to 100 sparks per minute. This seems to be an optimum balance between the desire to raise the electric field strength and to limit the number of sparks.

De Nevers (1995) also discusses sneakage, which can deteriorate ESP efficiency. In an ESP all the gas does not pass through the collecting zone, because the wires and plates do not completely reach to the bottom and top of the ESP. These untreated areas where the wires and plates are connected to the ESP are called sneakage. The effect of sneakage is minimised by using seals and baffles.

According to Katz (1979) corrosion factors are not of great importance where steady state operations apply, but the causes of corrosion are identified. Corrosion usually includes a loss of metal from large metal areas. The three major corrosion causes are:

- Temperature excursions that result in acid dew point or water vapour condensation.
- Air in-leakage
- Insufficient application of heat or insulation at exposed wall surfaces.

2.4. Identified shortcomings

Extensive experimental investigations and theoretical research were done on electrostatic precipitation. Accurate and stable ESP models were developed and are used to predict ESP performances. However there are still many grey areas that need more understanding. The following shortcomings were identified in the literature:

- The majority of ESP models are two-dimensional. This is because three-dimensional models are time consuming and computationally very expensive. The resources available to simulate the internal workings of large equipment like ESPs are also limited, which make two-dimensional simulations the preferred choice.

- Fewer investigations are being done on the gas flow through an ESP than on the electrostatics. The electrostatics is the less understood mechanisms in electrostatic precipitation and the electric field strength distribution is the most decisive factor in ESP collection efficiency. Thus more emphasis is placed on the electrical conditions.

- The Deutsch model is still being used in ESP design. Modern and more accurate models can be used to predict collection efficiencies. Thus smaller ESPs can be designed with the same capabilities of large Deutsch designed ESPs (Leonard *et al.*: 1980). This could ultimately result in fewer gas emissions and cost savings.

- Little research has been done on degrading effects like re-entrainment, back corona, ash resistivities and spark-over. These effects are known to have a large influence on collection efficiencies and need more attention.

2.5. Closure

The literature related to the process of electrostatic precipitation was discussed in this chapter. The two most important factors to ensure high collection efficiencies are the electric field strength distribution and the gas flow distribution. If the gas flow is not distributed over the entire precipitation field, some active collecting areas go to waste. This will result in lower collection efficiencies. Good gas distribution will also ensure lower mean velocities inside the collecting ducts. This will provide more treatment time for the fly ash particles to be properly charged and collected.

The main objective of this study is to develop a three dimensional CFD model of the gas flow through an ESP. The theory and mathematical formulations behind the fluid dynamics inside an ESP will be presented in the next chapter.

CHAPTER 3

3. Theory

3.1 Introduction

Chapter 2 contained the relevant literature on the process of electrostatic precipitation. Different ESP models were investigated and the influence of aspects like ESP geometry, ash resistivity and pulsed energization on ESP performance were discussed. This chapter describes the theory of fluid dynamics through an ESP. The governing equations used to develop a three-dimensional fluid flow model will be formulated. The complete and detailed theory behind fluid dynamics can be found in most CFD handbooks such as Versteeg & Malalasekera (1995).

CFD (Computational fluid dynamics) is the numerical analysis of systems involving fluid flow and heat transfer by means of computer simulations. Three separate numerical solution techniques can be identified: finite difference, finite element and spectral methods. The major differences between the separate methods are in the way that the flow variables are approximated and with the discretization process.

A special finite difference method namely the finite volume method is widely used by software packages like STAR-CD, FLUENT and Flo++ (Serfontein, 2000; Le Grange, 1999). Commercial CFD codes use numerical algorithms to solve fluid flow problems. These codes make use of sophisticated graphical user interfaces to input problem parameters and to examine the results, by this manner the solution power of the commercial code can easily be accessed.

All CFD codes consist of three main components:

- Pre-processor: The main purpose of the pre-processor is to define the computational domain (flow region) and the fluid properties.
- Solver: Solves the governing equations for the problem stated in the pre-processor, using a certain numerical method. The solution is iterated until the specified convergence criteria are satisfied.
- Post-processor: The function of the post-processor is to present the results.

Conservativeness, boundedness and transportiveness are incorporated into all finite volume methods in order to ensure successful CFD simulations. Good CFD modelling often includes a sensitive trade-off between accuracy and stability.

3.2 Governing equations

The governing equations of fluid flow dynamics is the conservation laws of physics (Versteeg & Malalasekera, 1995):

- Mass conservation.
- Momentum conservation.
- Energy conservation.

This study is only concerned with the fluid flow through an ESP and no thermal flow will be simulated. Thus only the mass and momentum conservation laws will be presented.

The behaviour of the fluid flow can be described by the macroscopic properties (such as velocity, pressure, density and temperature) because at macroscopic length scales the molecular structure and molecular motions of the fluid may be ignored. A small fluid element with sides δx, δy and δz is considered (Figure 3.1):

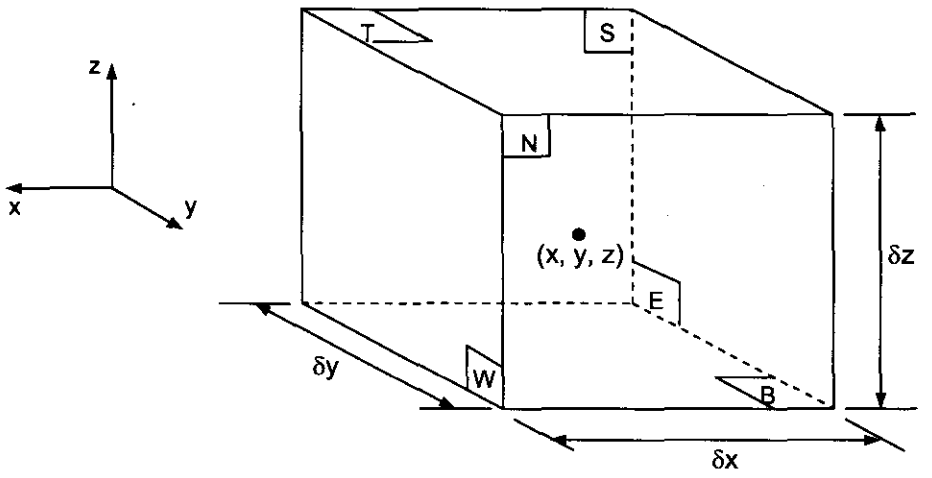

Figure 3.1: Fluid element for conservation laws.

The six faces are labelled as North, South, West, East, Top and Bottom. The centre of the fluid element is located at (x, y, z). The first two terms of the Taylor series can be used to describe the fluid properties at the faces of the small fluid element. For example if the pressure at the centre of the element is, p then the pressures at the faces W and E can be expressed as:

$$p - \frac{\partial p}{\partial x}\frac{1}{2}\delta x \quad and \quad p + \frac{\partial p}{\partial x}\frac{1}{2}\delta x$$

3.2.1 Mass conservation

The mass conservation of the fluid element can be described as:

Rate of mass increase in fluid element.	=	Rate of mass into the fluid element.	-	Rate of mass out of the fluid element.

The rate of mass increase in the fluid element is:

$$\frac{\partial}{\partial t}(\rho \delta x \delta y \delta z) = \frac{\partial \rho}{\partial t}\delta x \delta y \delta z \qquad (3.1)$$

where ρ is the density, t is time and $\delta x \delta y \delta z$ is the element volume.

The product of the density, area and the velocity component normal to the face gives the total mass flow rate across the face of the element. The total mass flow rate across the face of the fluid element is now equated to the rate of increase of mass inside the element. This leads to the following simplified equation:

$$\frac{\partial \rho}{\partial t} + \frac{\partial (\rho u)}{\partial x} + \frac{\partial (\rho v)}{\partial y} + \frac{\partial (\rho w)}{\partial z} = 0 \tag{3.2}$$

in vector notation:

$$\boxed{\frac{\partial \rho}{\partial t} + div\left(\rho \bar{u}\right) = 0} \tag{3.3}$$

where $\bar{u}$ is the velocity vector $u(u,v,w)$. Equation (3.3) gives the unsteady, three-dimensional mass conservation equation at a point in a compressible fluid. The first term describes the rate of charge in time of the density and the second term describes the net mass flow across the element faces and is called the convective term. For a constant density ρ the equation reduces to:

$$div\left(\bar{u}\right) = 0 \tag{3.4}$$

This equation describes the mass flow rate for an incompressible fluid.

3.2.2 Momentum conservation

Momentum conservation can be described as the rate of change of momentum which is equal to the sum of the forces acting on a fluid particle (Newton's second law).

Rate of increase of momentum in fluid element.	=	Rate of momentum into the fluid element.	-	Rate of momentum out off the fluid element.	+	Sum of forces acting on the fluid element.

Rates of increase of momentum in the x-, y-, and z-directions per unit volume of a fluid particle can be expressed as:

$$\rho\frac{Du}{Dt}, \qquad \rho\frac{Dv}{Dt}, \qquad \rho\frac{Dw}{Dt}, \tag{3.5}$$

Two types of forces acting on fluid particles can be identified:

- Surface forces: Pressure and viscous forces
- Body forces: Gravity, centrifugal, Coriolis and electromagnetic forces.

It is common practice to include the effects of surface forces as separate terms in the momentum equation and the body forces as source terms.
The stresses on a fluid element can be defined in terms of the pressure and the viscous stress components acting on the fluid element. The pressure (normal stress) is denoted by p and the viscous stresses by τ_{ij}. Where i and j indicate the stress component that acts in the j-direction on a surface normal to the i-direction. The magnitude of the forces acting on the fluid element is the product of the stresses and areas. Thus the net force acting on the fluid element in the x-direction is the sum of the force components acting in that direction. By setting the rate of increase of x-momentum equal to the total force in the x-direction due to surface stresses plus the rate of increase of x-momentum due to sources, gives the x-component of the momentum equation:

$$\rho\frac{Du}{Dt} = \frac{\partial\left(-p+\tau_{xx}\right)}{\partial x} + \frac{\partial\tau_{yx}}{\partial y} + \frac{\partial\tau_{zx}}{\partial z} + S_{Mx} \tag{3.6}$$

the y-component of the momentum equation:

$$\rho\frac{Dv}{Dt} = \frac{\partial\tau_{xy}}{\partial x} + \frac{\partial\left(-p+\tau_{yy}\right)}{\partial y} + \frac{\partial\tau_{zy}}{\partial z} + S_{My} \tag{3.7}$$

the z-component of the momentum equation:

$$\rho\frac{Dw}{Dt}=\frac{\partial\tau_{xz}}{\partial x}+\frac{\partial\tau_{yz}}{\partial y}+\frac{\partial\left(-p+\tau_{zz}\right)}{\partial z}+S_{Mz} \tag{3.8}$$

in vector notation:

$$\rho\frac{D\bar{u}}{Dt}=-grad(p)+div(\bar{\tau}_{ij})+\bar{S}_M \tag{3.9}$$

where $\bar{S}_M$ is the source vector term $\left(S_{Mx},S_{My},S_{Mz}\right)$.

3.3 Navier-Stokes equations

The governing equations contain the unknown viscous stresses, τ_{ij}, which need a suitable model, in order to develop more useful forms for the conservation laws. In Newtonian fluids the viscous stresses are proportional to the deformation rates. In three-dimensions the viscous stresses can be describe by two proportionally constants: the dynamic viscosity, μ, which relate to linear deformations and the second viscosity, λ, which relates to the volumetric deformation. The nine viscous stress components for Newtonian and isotropic flow can be formulated as follows:

$$\tau_{xx}=2\mu\frac{\partial u}{\partial x}+\lambda div(\bar{u}) \tag{3.10}$$

$$\tau_{yy}=2\mu\frac{\partial v}{\partial y}+\lambda div(\bar{u}) \tag{3.11}$$

$$\tau_{zz}=2\mu\frac{\partial w}{\partial z}+\lambda div(\bar{u}) \tag{3.12}$$

$$\tau_{xy}=\tau_{yx}=\mu\left(\frac{\partial u}{\partial y}+\frac{\partial v}{\partial x}\right) \tag{3.13}$$

$$\tau_{xz} = \tau_{zx} = \mu\left(\frac{\partial u}{\partial z} + \frac{\partial w}{\partial x}\right) \tag{3.14}$$

$$\tau_{yz} = \tau_{zy} = \mu\left(\frac{\partial v}{\partial z} + \frac{\partial w}{\partial y}\right) \tag{3.15}$$

The second viscosity, λ, effect is small in practice and a good approximation can be obtained by taking the value $\lambda = -\frac{2}{3}\mu$. In the case of incompressible fluids, equation (3.4), the second term of equations (3.10 - 3.12) falls away. Substituting the viscous stress equations (3.10 – 3.15) into equations (3.6 – 3.8) then re-arranging the viscous terms and "hiding" the two smaller contributions to the viscous stress terms in the momentum source terms, leads to the Navier-Stokes equations:

$$\rho\frac{Du}{Dt} = -\frac{\partial p}{\partial x} + div\left(\mu\, grad(u)\right) + S_{Mx} \tag{3.16}$$

$$\rho\frac{Dv}{Dt} = -\frac{\partial p}{\partial y} + div\left(\mu\, grad(v)\right) + S_{My} \tag{3.17}$$

$$\rho\frac{Dw}{Dt} = -\frac{\partial p}{\partial z} + div\left(\mu\, grad(w)\right) + S_{Mz} \tag{3.18}$$

3.4 The finite volume method

Introducing the general variables ϕ and Γ, the Navier-Stokes equations can be written in a more compact form:

$$\underset{1}{\frac{\partial \rho\phi}{\partial t}} + \underset{2}{div\left(\rho\phi\bar{u}\right)} = \underset{3}{div\left(\Gamma\, grad\ \phi\right)} + \underset{4}{S_{\phi}} \tag{3.19}$$

The terms of the equation can be explained as follows:

1. Rate of increase of ϕ in a fluid element.
2. Total rate of decrease of ϕ due to convection across the boundaries of the fluid element.
3. Rate of increase of ϕ due to diffusion across the boundaries of the fluid element.
4. Rate of increase of ϕ due to the sources in the fluid element.

By setting ϕ equal to u, v, w and Γ to the appropriate diffusion coefficient, the mass and momentum equations can be obtained. Equation (3.19) is called the transport equation for property ϕ. The steady-state transport equation can be presented by deleting the transient term:

$$div\left(\rho\bar{u}\phi\right) = div\left(\Gamma\ grad\ \phi\right) + S_\phi \tag{3.20}$$

The computational domain is divided into a finite number of control volumes with a finite number of flat faces. The integration of equation (3.20) over a three-dimensional control volume, CV yields:

$$\int_{CV} div\left(\rho\phi\bar{u}\right)dV = \int_{CV} div\left(\Gamma\ grad\ \phi\right)dV + \int_{CV} S_\phi dV \tag{3.21}$$

The Gauss-divergence theorem is applied:

$$\int_{A} \bar{n}.\left(\rho\phi\bar{u}\right)dA = \int_{A} \bar{n}.\left(\Gamma\ grad\ \phi\right)dA + \int_{CV} S_\phi dV \tag{3.22}$$

where A is the surface area of the control volume face, V is the volume, S_ϕ is the source in the control volume and $\bar{n}$ is the vector normal to the surface element dA.

The steady-state convection and diffusion of the property ϕ in three-dimensions is given by:

$$\frac{d}{dx}(\rho u\phi)+\frac{d}{dy}(\rho u\phi)+\frac{d}{dz}(\rho u\phi)=\frac{d}{dx}\left(\Gamma\frac{\partial\phi}{\partial x}\right)+\frac{d}{dy}\left(\Gamma\frac{\partial\phi}{\partial y}\right)+\frac{d}{dz}\left(\Gamma\frac{\partial\phi}{\partial z}\right)+S_{\phi_P}V_P \tag{3.23}$$

A three-dimensional grid is used to subdivide the domain. Figure 3.2 illustrates a typical control volume:

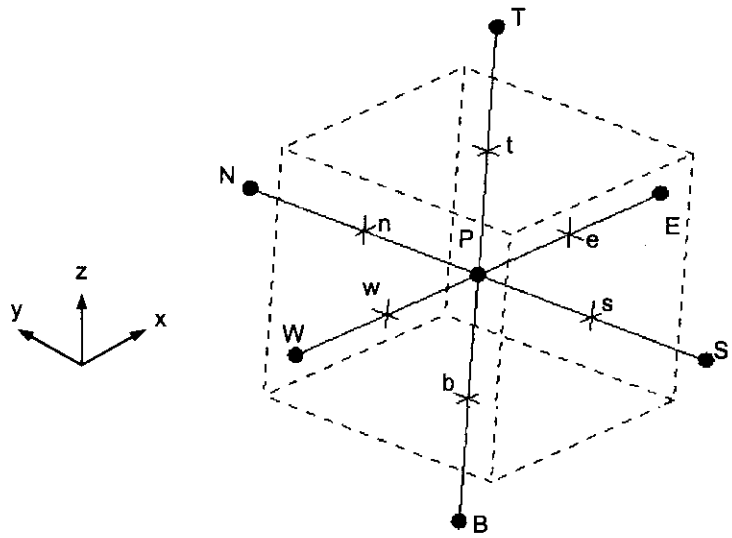

Figure 3.2: Cell in three-dimensions with neighbouring nodes.

The cell node P has six neighbouring nodes identified as west, east, south, north, bottom and top (W, E, S, N, B, T) and also six cell-faces (w, e, s, n, b, t).

Two variables F and D are defined to represent the convective flux per unit area and diffusion conductance at the cell faces:

$$F_w = (\rho u)_w A_w, \quad F_e = (\rho u)_e A_e, \quad F_s = (\rho u)_s A_s,$$
$$F_n = (\rho u)_n A_n, \quad F_b = (\rho u)_b A_b, \quad F_t = (\rho u)_t A_t \tag{3.24}$$

and

$$D_w = \left(\frac{\Gamma_w}{\delta x_{WP}}\right) A_w, \quad D_e = \left(\frac{\Gamma_e}{\delta x_{PE}}\right) A_w, \quad D_s = \left(\frac{\Gamma_s}{\delta x_{SP}}\right) A_s,$$
$$D_n = \left(\frac{\Gamma_n}{\delta x_{PN}}\right) A_n, \quad D_b = \left(\frac{\Gamma_b}{\delta x_{BP}}\right) A_b, \quad D_t = \left(\frac{\Gamma_t}{\delta x_{PT}}\right) A_t, \tag{3.25}$$

Integration of the transport equation (3.23) over the control volume and the substitution of equations (3.24) and (3.25) into equation (3.23) gives:

$$\begin{aligned}&(F_e\phi_e - F_w\phi_w) + (F_n\phi_n - F_s\phi_s) + (F_t\phi_t - F_b\phi_b) = (D_e(\phi_E - \phi_P) - D_w(\phi_P - \phi_W)) \\ &+ (D_n(\phi_N - \phi_P) - D_s(\phi_P - \phi_S)) + (D_t(\phi_T - \phi_P) - D_b(\phi_P - \phi_B)) + S_{\phi_P} V_p\end{aligned} \tag{3.26}$$

Using the upwind differencing scheme equation (3.26) can be written as:

$$\boxed{a_P\phi_P = a_W\phi_W + a_E\phi_E + a_S\phi_S + a_N\phi_N + a_B\phi_B + a_T\phi_T + S_P} \tag{3.27}$$

Table 3.1 shows the neighbouring coefficients of equation (3.27):

Neighbour coefficients:	Values:
a_W	$D_w + \max(F_w, 0)$
a_E	$D_e + \max(0, -F_e)$
a_S	$D_s + \max(F_s, 0)$
a_N	$D_n + \max(0, -F_n)$
a_B	$D_b + \max(F_b, 0)$
a_T	$D_t + \max(0, -F_t)$
a_P	$a_W + a_W + a_W + a_W + a_W + a_W + \Delta F$
S_P	$S_{\phi_P} V_P$

Table 3.1: Neighbour coefficients.

with $$\Delta F = F_e - F_w + F_n - F_s + F_t - F_b$$

The discretised equation (3.27) is formulated for all the nodes in the flow domain. This results in a system of linear algebraic equations and is solved by the SIMPLE algorithm (Chapter 3.5) in order to obtain the distribution of ϕ over the domain.

3.4.1 The upwind differencing scheme

The upwind differencing scheme is conservative because it utilises consistent expressions to calculate the flow fluxes through the cell faces. The most attractive characteristic of this scheme is its stability due to boundedness. This is because all the coefficients of the discretised equation are always positive. The flow direction is accounted for, thus transportiveness is built into the formulation. The upwind differencing scheme is based on the backward differencing formula, thus the accuracy is only first order on the basis of Taylor series truncation error. The major weakness of the scheme is that it

produces flawed results when the flow is not aligned with the grid lines (Versteeg & Malalasekera, 1995). In general the flow in the ESP model will be aligned with the grids, thus this flaw in the scheme will not have a significant effect on the numerical results.

3.5 The SIMPLE algorithm

The SIMPLE algorithm (Semi-Implicit Method for Pressure-Linked Equations) is a guess-and-correct procedure to solve the discretised Navier-Stokes equations for a staggered grid, shown in Figure 3.3. The method is illustrated for two-dimensional flow for clarity purposes. For three-dimensional problems the equations can be derived in the same manner. The procedure of the SIMPLE algorithm is illustrated by Figure 3.4 and an explanation for every step is also given. The detail of the derivations of the equations can be found in Versteeg & Malalasekera (1995).

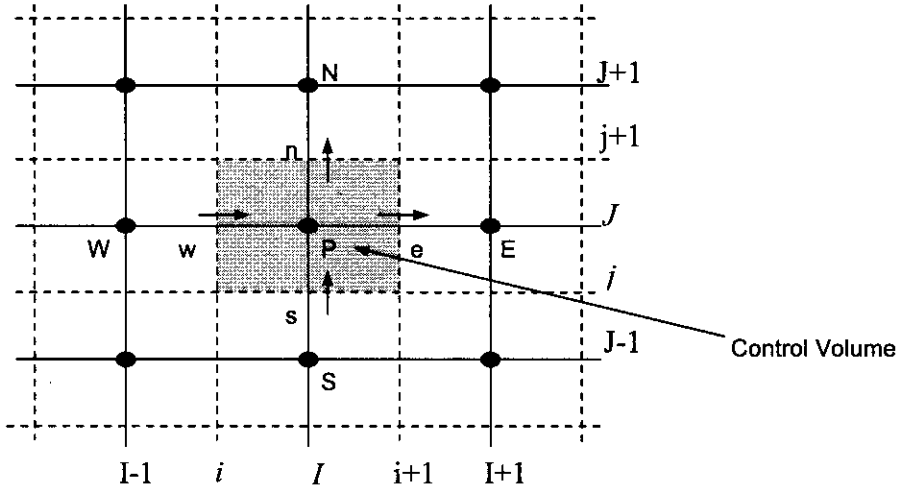

Figure 3.3: Staggered grid for two dimensional fluid flow calculations.

Step 1: The SIMPLE algorithm is initiated by guessing a pressure field, p^*.

Step 2: The guessed pressure field, p^*, is used to solve the discretised momentum equations in order to calculate the velocity components, u^* and v^*.

$$a_{i,J}u^*_{i,J} = \sum a_{nb}u^*_{nb} + \left(p^*_{I-1,J} - p^*_{I,J}\right)A_{i,J} + b_{i,J} \tag{3.28}$$

$$a_{I,j}u^*_{I,j} = \sum a_{nb}v^*_{nb} + \left(p^*_{I,J-1} - p^*_{I,J}\right)A_{I,j} + b_{I,j} \tag{3.29}$$

Where i, j denote the cell face locations and I, J denote the cell centre locations, the subscript nb presents the neighbour cells, A is the face area and b is the source term.

The pressure field correction, p', and velocity corrections, u' and v' can be defined as:

$$p' = p - p^* \quad \Rightarrow \quad p = p^* + p' \tag{3.30}$$

$$u' = u - u^* \quad \Rightarrow \quad u = u^* + u' \tag{3.31}$$

$$v' = v - v^* \quad \Rightarrow \quad v = v^* + v' \tag{3.32}$$

The main assumption made by the SIMPLE algorithm is the omission of the terms, $\sum a_{nb}u'_{nb}$ and $\sum a_{nb}v'_{nb}$ in the descritised equations for the velocity corrections. Thus the velocity correction descritised equations can be written as:

$$u'_{i,J} = d_{i,J}\left(p'_{I-1,J} - p'_{I,J}\right) \tag{3.33}$$

$$v'_{I,j} = d_{I,j}\left(p'_{I,J-1} - p'_{I,J}\right) \tag{3.34}$$

where

$$d_{i,J} = \frac{A_{i,J}}{a_{i,J}} \quad and \quad d_{I,j} = \frac{A_{I,j}}{a_{I,j}} \tag{3.35}$$

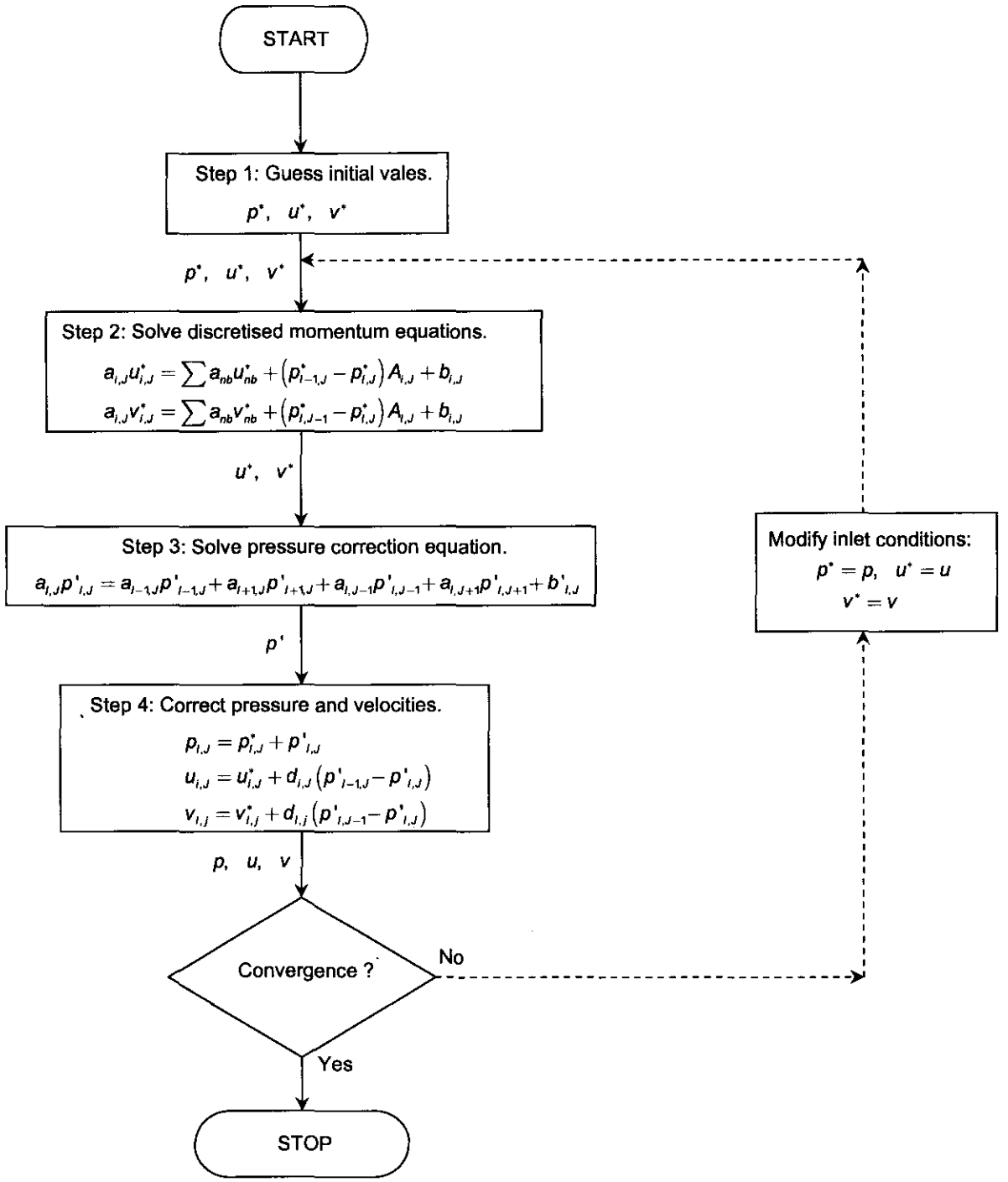

Figure 3.4: The SIMPLE algorithm.

Step 3: The correction pressure, p', is determined by the pressure correction equation:

$$a_{I,J}p'_{I,J} = a_{I+1,J}p'_{I+1,J} + a_{I-1,J}p'_{I-1,J} + a_{I,J+1}p'_{I,J+1} + a_{I,J-1}p'_{I,J-1} + b_{I,J} \tag{3.36}$$

Step 4: The calculated correction pressure, p', together with substituting equations (3.33), (3.34) and (3.35) into equations (3.31) and (3.32) gives the calculated actual pressure and velocities, p, u, and v:

$$p_{I,J} = p^*_{I,J} + p'_{I,J} \tag{3.37}$$

$$u_{i,J} = u^*_{i,J} + d_{i,J}\left(p'_{I-1,J} - p'_{I,J}\right) \tag{3.38}$$

$$v_{I,j} = v^*_{I,j} + d_{I,j}\left(p'_{I,J-1} - p'_{I,J}\right) \tag{3.39}$$

Step 5: Test for convergence, if not, repeat from step 2 and set the pressure and velocity values to:

$$p^* = p \tag{3.40}$$

$$u^* = u \tag{3.41}$$

$$v^* = v \tag{3.42}$$

3.6 Turbulence

The commercial software, Flo++ (Le Grange, 1999) employs the high Reynolds number $k-\varepsilon$ turbulence model. The model uses two different transport equations, one for the turbulent kinetic energy, k and one for the rate of dissipation of turbulent kinetic energy, ε. The Reynolds stresses are

calculated from these equations and incorporated into the momentum equations (Versteeg & Malalasekera, 1995).

The eddy viscosity, μ_t is defined as:

$$\mu_t = \rho C_\mu \frac{k^2}{\varepsilon} \tag{3.43}$$

where C_μ is a dimensionless constant.

The $k-\varepsilon$ turbulence model uses the following transport equations for, k and ε:

$$\boxed{\frac{\partial(\rho k)}{\partial t} + div\left(\rho k \overline{U}\right) = div\left(\frac{\mu_t}{\sigma_k}\ grad\ k\right) + 2\mu_t E_{ij} \cdot E_{ij} - \rho\varepsilon} \tag{3.44}$$

$$\boxed{\frac{\partial(\rho\varepsilon)}{\partial t} + div\left(\rho\varepsilon \overline{U}\right) = div\left(\frac{\mu_t}{\sigma_\varepsilon}\ grad\ \varepsilon\right) + C_{1\varepsilon}\frac{\varepsilon}{k}2\mu_t E_{ij} \cdot E_{ij} - C_{2\varepsilon}\rho\frac{\varepsilon^2}{k}} \tag{3.45}$$

1 2 3 4 5

The terms in equations (3.44) and (3.45) can be explained as follow:

1. Rate of change of k or ε.
2. Transport of k or ε by convection.
3. Transport of k or ε by diffusion.
4. Rate of production of k or ε.
5. Rate of destruction of k or ε.

The equations contain five adjustable constants, $C_{1\varepsilon}$, $C_{2\varepsilon}$, C_μ, σ_k and σ_ε. The values for these constant were found by comprehensive data fitting for a wide range of turbulent flows and are shown in Table 3.2. The Prandtl

numbers σ_k and σ_ε connect the diffusivities of k and ε to μ_t. The rate of deformation of the fluid element is presented by E_{ij}.

Symbol	C_μ	σ_k	σ_ε	$C_{1\varepsilon}$	$C_{2\varepsilon}$
Value	0.09	1.00	1.30	1.44	1.92

Table 3.2: Adjustable constant values for $k-\varepsilon$ model.

3.7 Closure

This chapter presented the relevant theory behind CFD modelling of fluid flow through an ESP. The governing equations were presented, which are used to develop the Navier-Stokes equations. The finite volume method uses the Navier-Stokes equations to develop discretised equations, where the pressures and velocities of one cell are written in terms of the neighbouring cells properties. The SIMPLE algorithm is then used to solve the discretised equations, in order to calculate the actual velocities and pressures in the flow domain.

The next chapter discusses the development and implementation of a fluid flow ESP model. The ESP geometry forms an important part in the development of the CFD model. The assumptions and the boundary conditions of the model will also be discussed.

CHAPTER 4

4. ESP Model

4.1 Introduction

Chapter 3 presented the basic theory used for the computation of the fluid dynamics of a certain flow region. Thermal flow does not form part of this research, thus only the mass and momentum laws are applied. The previous chapter also described the SIMPLE algorithm, which is used to solve the governing equations.

The main objective of this study is to develop a numerical model to simulate the gas flow through an ESP. This chapter will discuss the ESP geometry and the main internal structures, which influence the bulk gas flow through the ESP. The computer resources and time available for this study were not adequate to develop a detailed fluid flow ESP model and the model will only be used to give an overview of the gas flow through an ESP. This means that certain assumptions will be made in order to simplify the model. These assumptions and the boundary conditions of the model will also be discussed.

4.2 Flow Domain

Figure 4.1 illustrates the large scale of an industrial precipitator used by SASOL industries. The simulation of the gas flow through the entire ESP is impractical and would be very expensive concerning time and computational resources. Therefore some of the flow regions will be excluded from the simulation. The grey areas in Figure 4.1 depict the excluded areas. The entire flow region is divided into two sections because of the symmetry seen in the top view. Secondly two of the electric fields were also excluded from the flow domain.

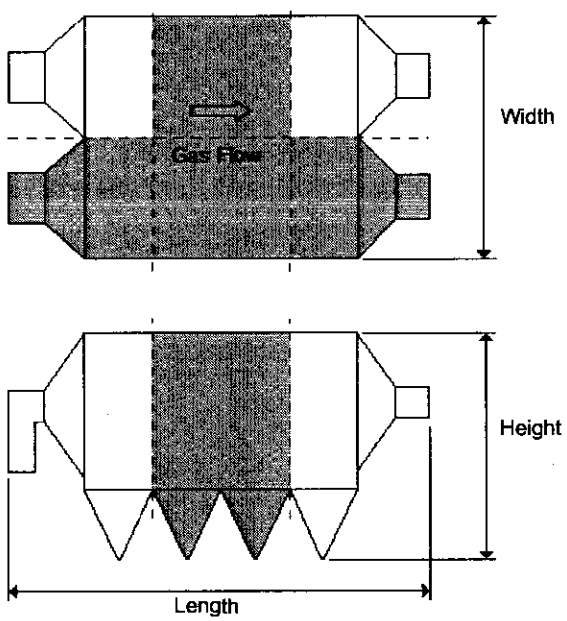

Dimension	SASOL ESP	Numerical Model
Length	38.72 m	26.08 m
Width	22.8 m	11.4 m
Height	21.5 m	21.5 m

Figure 4.1: Top and front view of a SASOL ESP.

Figure 4.2 shows the flow domain identified for the numerical model. This means that only a quarter of the main electric flow region, three hoppers (two halves and two whole hoppers), one inlet and one outlet are simulated. This will reduce the number of cells required to simulate the flow through the ESP considerably. The model can thus be more accurate because a finer grid can be used for the smaller flow domain.

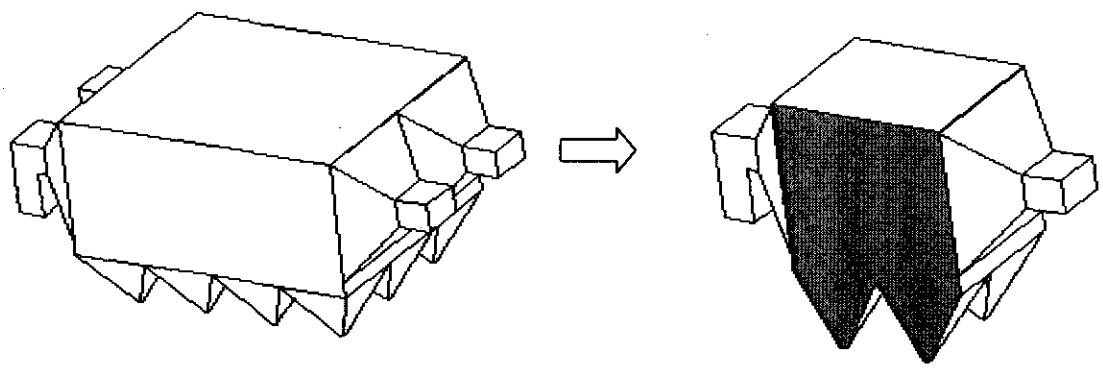

Figure 4.2: a) Full-scale ESP. b) Flow domain of ESP model.

4.3 ESP inlet

The flow region in front of the collecting ducts is of great importance because it determines the gas flow distribution through the collecting areas. Uniform gas flow distribution will ensure that the entire collecting area is utilized. This will also ensure that the average velocity of the gas flow is reduced to an acceptable level, in order to ensure more residence time for the ash particles inside the collecting ducts. A non-uniform gas distribution will result in low collection efficiencies. This area includes the inlet duct (just in front the ESP) and the ESP inlet, which is the expansion area in front of the main flow area.

4.3.1 Inlet duct

A sharp bend is present in the inlet duct in front of the ESP (Figure 4.1). This sharp bend can have serious degrading effects on the ESP efficiency, if it is not properly designed. The gas flow will be non-uniform as it enters the ESP, resulting in a non-uniform gas distribution throughout the ESP. Using turning vanes at the turn can eliminate the effect of the sharp bend. Figure 4.3 shows the turning vanes in the inlet duct. The SASOL precipitators are equipped with fifteen turning vanes at the ESP inlet. Earlier studies showed that the dimensions of the turning vanes also influence the ESP performance.

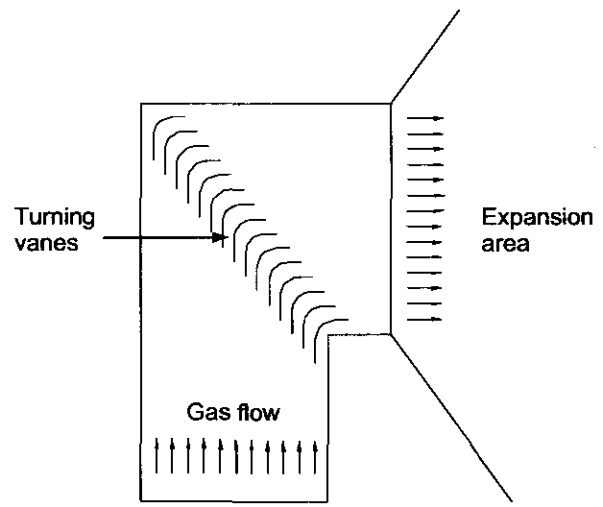

Figure 4.3: ESP inlet duct with turning vanes.

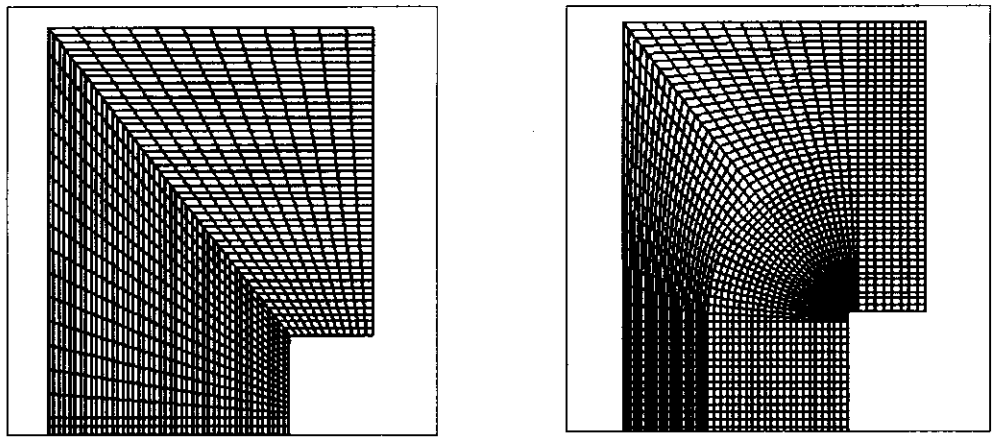

a b

Figure 4.4: Grids for inlet duct: a) Rectangular grid. b) Semi-elliptic grid.

The most effective dimensions were identified as 400 mm in the horizontal direction and 550 mm in the vertical direction.

Various grid layouts were considered to simulate the inlet to the ESP. Semi-elliptical and rectangular grids proved to provide the best solution. Figure 4.4 shows the two different grid layouts. The elliptical grid does not approximate the effect of the turning vanes as well as can be expected and only four numerical turning vanes can be inserted. The rectangular grid provides a much more stable solution and eight numerical turning vanes can be inserted, which are adequate to simulate the effect of the tuning vanes. The pressure drop over the inlet duct will be incorrect with eight and not fifteen turning vanes. However, this study is more concerned with the gas flow patterns through the ESP and the stability of the simulation. Thus eight vanes are sufficient for this study. Every turning vane is simulated as a solid baffle on the cell boundaries at the specific location for the turning vane.

4.3.2 Expansion area

The well-organized flow, due to the turning vanes, enters the expansion inlet of the ESP. The flow must be expanded to the whole area, in order to obtain a good gas flow distribution over the entire collecting flow area. This can be

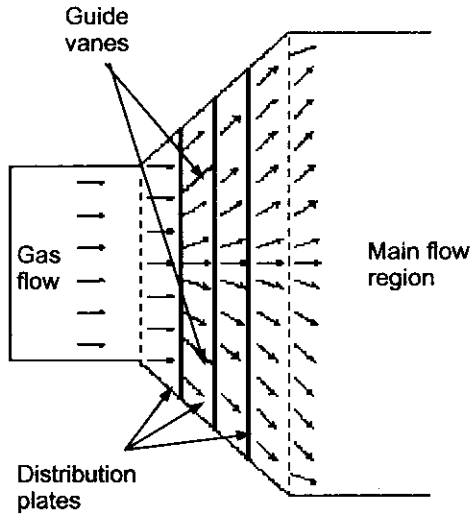

Figure 4.5: Expansion area with distribution plates (Top view).

achieved by using distribution plates. The distribution plates are located in the expansion area at even intervals, shown in Figure 4.5. Distribution plates are perforated metal plates (plates with holes), which are placed perpendicular to the flow direction. This will force the flow to spread more evenly over the entire flow domain. The expansion area is also equipped with guiding vanes (Figure 4.5). The purpose of the guiding vanes is to guide some of the flow more to the outside of the flow region. These vanes are solid metal plates and are located between the first and second distribution plates at the bottom of the expansion area. The guide vanes do not extend over the whole height of the expansion area and are only 2.5 m high. The distribution plates and guide vanes in the expansion area will ensure that the whole flow area is utilized.

Figure 4.6 shows the perforation detail of the distribution plates. The dimensions of the first distribution plate (small plate) is about $5.9m \times 6.6m$, which means the number of holes in the plate is about 15 500. The dimensions of the second distribution plate is about $8.2m \times 8.1m$, and consist of about 26 500 holes. The last plate's dimensions is about $10.5m \times 9.7m$, and consist of about 40 500 holes. The computer resources available are not adequate to handle a simulation of such detail. Porous baffles can be used to approximate the effect of the perforated plates.

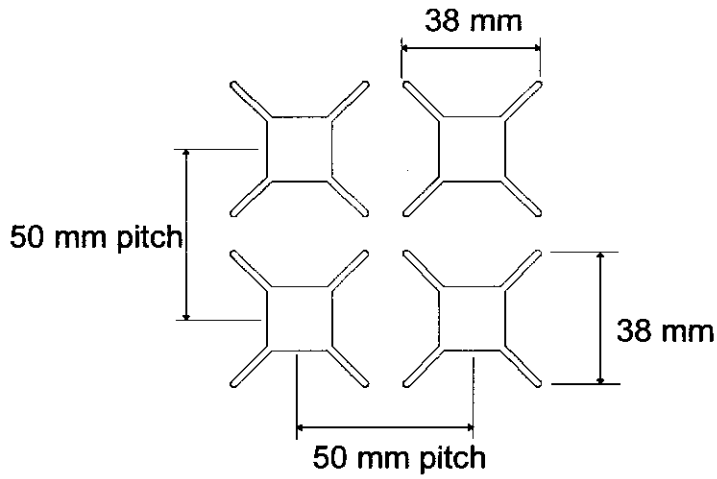

Figure 4.6: Perforation Detail of distribution plates.

Porous baffle

In Flo++ a porous baffle is defined in terms of the pressure drop, Δp, across the baffle and is given by (STAR-CD Methodology Version 3.10, 1999):

$$\Delta p = -\rho\left(\alpha|v_n| + \beta\right)v_n \tag{4.1}$$

where v_n is the superficial velocity normal to the baffle surface and α & β are user-specified coefficients defining the baffle permeability. The superficial velocity is defined as the volume flow rate divided by the total cross sectional area. It is assumed that the flow direction is uncharged as it passes through the baffle.

In order to use porous baffles in the ESP model the values of α and β must be determined. Determining the relationship between the pressure drop and the velocity across one hole in the distribution plates can determine these values. An alternative CFD simulation, of one distribution hole, can be used to determine the relationship. Figure 4.7 shows the flow domain of this simulation. The perforation detail (Figure 4.6) of one hole is approximated by a square hole.

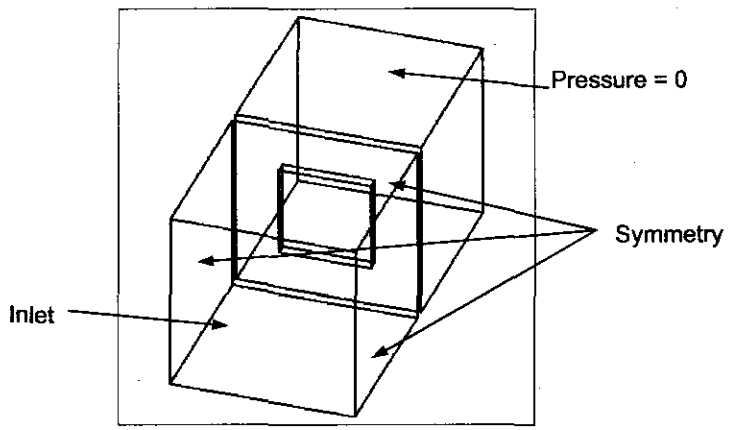

Figure 4.7: Flow domain for distribution hole simulation with boundary conditions.

The inlet velocity of the flow domain was varied and the pressure drop over the domain was calculated. Symmetry boundary conditions were used for the sides of the flow domain and a pressure boundary at the outlet. The relationship between the pressure drop and flow velocity is presented in figure 4.8.

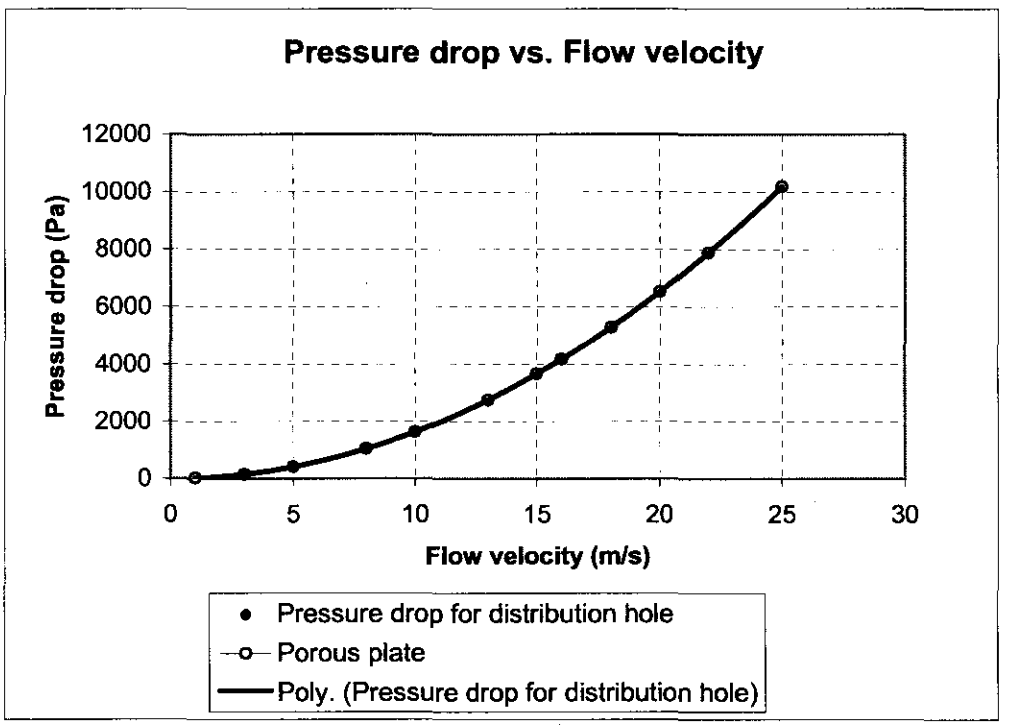

Figure 4.8: Relationship between pressure drop and flow velocity for distribution plates.

A second order polynomial was fitted to the simulation points (Figure 4.8):

$$\Delta p = -\left(16.274\ |v_n| + 0.3455\ \right)v_n \tag{4.2}$$

thus,

$$\alpha = 16.274 \quad and \quad \beta = 0.3455 \tag{4.3}$$

The hole in the flow domain was replaced by a porous baffle in order to determine if the values of α and β are correct. The difference in the pressure drops of the distribution hole simulation and the porous baffle simulation were negligible (Figure 4.8). Thus porous baffles can be used to approximate the effect of the distribution plates on the gas flow through the ESP.

4.4 Collecting flow domain

The distributed flow moves through the collecting flow region towards the ESP outlet. The collecting flow domain consists of the four electrical fields, the bottom hoppers and the rapping system. The effect of the rapping system structure on the gas flow is small in comparison with the effect of the collecting structures and will be excluded in this study.

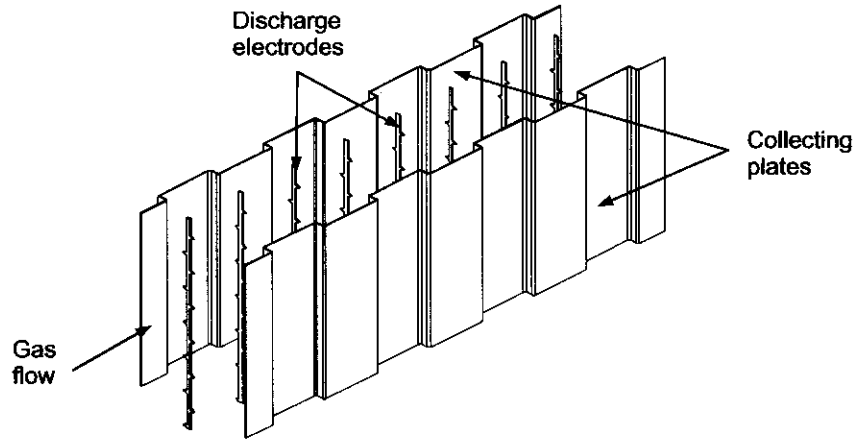

Figure 4.9: Electrical field flow area.

In the ESP model only two electrical field regions are considered. One electrical field is about 4.32 m long and 13.75 m high and consists mainly of the collecting plates and discharge electrodes. Figure 4.9 shows a section of the electrical field region. The effect of the discharge electrodes on the fluid flow through the collecting ducts is negligible and will be excluded from this study.

The dimensions of the collecting duct are illustrated in Figure 4.10-a and Table 4.1. The collecting plates are at 300 mm intervals in the electrical fields. Thus one electrical field consists of 76 collecting passages (Appendix A). Only half of the electrical fields are considered in the ESP model, thus the effect of 38 collecting passages on the gas flow must be simulated. Once again the detail is to complex for the available computer resources, therefore an approximation is required for the electrical fields.

A possible approximation is to simulate the collector plates as solid straight baffles with a large wall roughness. The purpose of the large wall roughness is to obtain the pressure drop associated with the original collector plate geometry. This approximation however gives an unstable solution and requires a large number of cells. A second approximation is to simulate the electrical field as porous media. The same method, which was used to define the porous baffle, will be used to define the porous media.

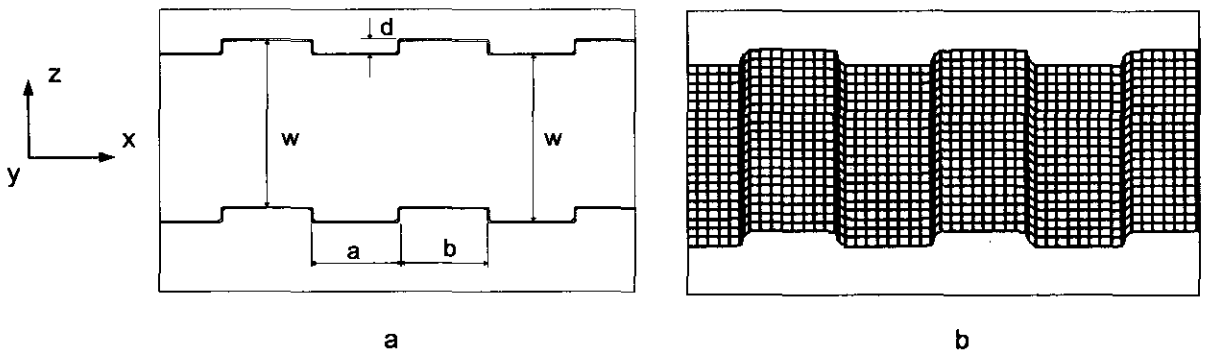

Figure 4.10: a) Collector plate geometry. b) Collector plate numerical grid.

Dimension	W	a	b	d
Value	0.3 m	0.15 m	0.15 m	0.025 m

Table 4.1: Dimensions of collector plates.

Porous media

Similar to a porous baffle, the porous media is also defined in terms of the pressure drop, ∂p, over the porous media (STAR-CD Methodology Version 3.10, 1999):

$$-K_i u_i = \frac{\partial p}{\partial \xi_i} \tag{4.4}$$

where $\xi_i \quad (i = x, y, z)$ represents the orthotropic directions, K_i is the permeability and u_i is the superficial velocity in direction ξ_i. The permeability, K_i is assumed to be a quasilinear function of the superficial velocity magnitude, $|\bar{u}|$ of the from:

$$K_i = \alpha_i \left|\bar{u}\right| + \beta_i \tag{4.5}$$

Combining equations (4.4) and (4.5), gives the pressure drop across the porous volume:

$$\boxed{\frac{\partial p}{\partial \xi_i} = -\left(\alpha_i \left|\bar{u}\right| + \beta_i\right) u_i} \tag{4.6}$$

where α_i and β_i are user-supplied coefficients for the direction ξ_i.

The values of α_i and β_i for the pressure drop over the collecting duct geometry must be determined in order to use porous medias as an approximation for the electrical fields. The main difference between a porous baffle and a porous media is that the pressure drop over a baffle is across an area but the pressure drop over a porous media is across a volume. Thus the

pressure drop per meter over the collecting duct must be determined in order to determine the values of α_i and β_i. The pressure drop across the collecting duct geometry can be determined by using a fluid flow simulation.

Figure 4.10-b shows the computational grid for the collecting duct simulation. Symmetry boundary conditions were used for the top and bottom boundaries, a pressure boundary condition for the outlet boundary and wall boundaries for the front and back boundaries. The inlet velocity of the simulation was varied and the pressure drop across the flow domain was determined. The pressure drop was then divided by the length of the flow domain in order to obtain the pressure drop per meter. This was done for the x- and y-directions. Figure 4.11 and Figure 4.12 show the pressure drop per meter though the collecting duct, for different flow velocities, in the x-direction and in the y-direction respectively. The gas flow in the z-direction is very limited because of the orientation of the collecting plates (Figure 4.10). Thus the α value is set to zero for stability reasons and the β value is set to a thousand in order to limit the flow in the z-direction.

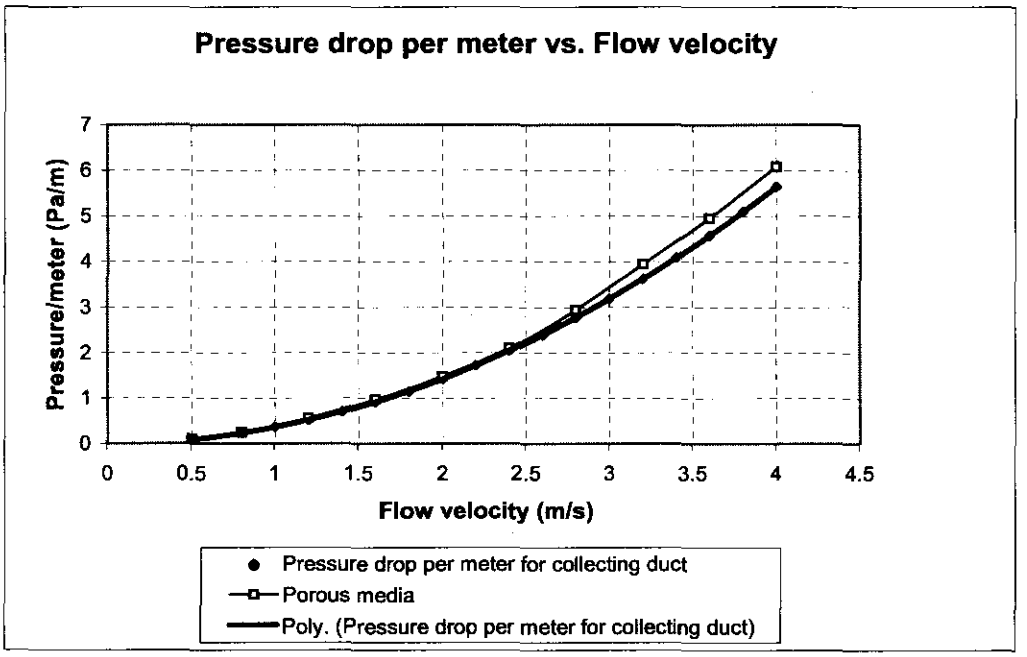

Figure 4.11: Pressure drop per meter in collecting duct in x-direction.

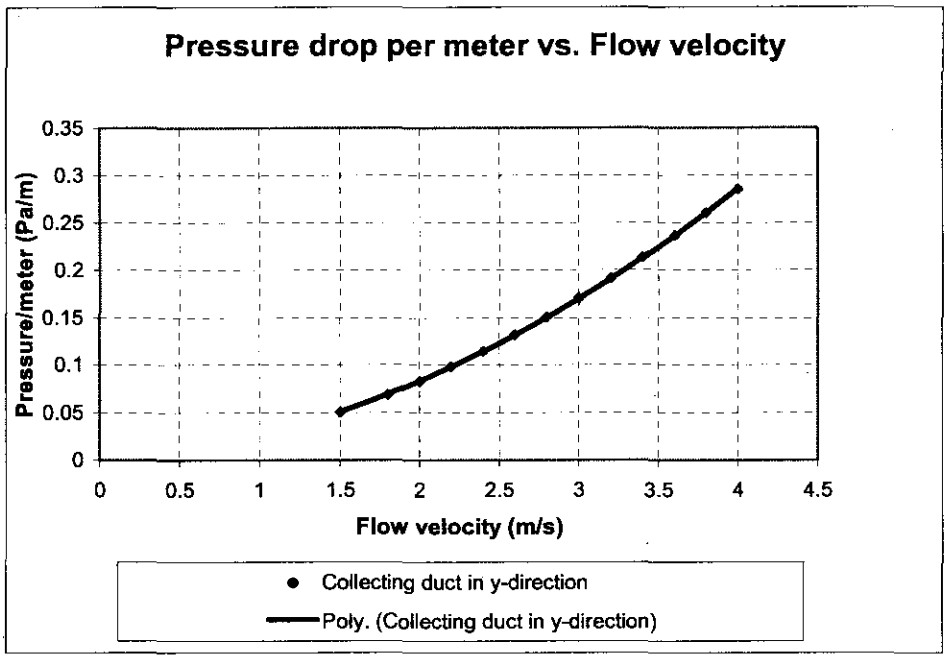

Figure 4.12: Pressure drop per meter in collecting duct in y-direction.

Two second order polynomials (one for the x-direction and one for the y-direction) were fitted to the simulation points (Figure 4.11 and Figure 4.12):

$$\frac{\partial p}{\xi_x} = -\left(0.3501\ |\bar{u}| + 0.0108\right) u_x \tag{4.7}$$

and

$$\frac{\partial p}{\xi_y} = -\left(0.015\ |\bar{u}| + 0.0115\right) u_y \tag{4.8}$$

thus,

$$\alpha_x = 0.3501 \quad \& \quad \beta_x = 0.0108 \tag{4.9}$$

$$\alpha_y = 0.015 \quad \& \quad \beta_y = 0.0115 \tag{4.10}$$

$$\alpha_z = 0 \quad \& \quad \beta_z = 1000 \tag{4.11}$$

A rectangular porous flow domain was used with the same volume as the collecting duct simulation in order to confirm if the α_i and β_i values are correct. The pressure drop per meter of the collecting duct simulation and the pressure drop per meter of the porous media simulation are in good agreement (Figure 4.11). Thus porous media can be used to predict the effect of the electrical fields on the gas flow.

It is important to note that when the gas flow is not perpendicular to the porous baffle and the porous media, additional loss factors are necessary to accurately describe the flow through these porous regions (Du Toit & Kotze, 1990). To accurately describe the flow through the porous region the approach angle of the flow must be taken into account. This is because the flow approaching the porous region at an angle sees a reduced flow area and therefore a higher flow resistance should be applied. According to Jansen van Rensburg & Van Staden (2003) accurate modelling of gas flow through a screen (distribution plate) must account for the following:

- The change in the resistance as a function of the angle of incidence, the screen thickness and the Free Area Ratio (FAR) of the screen. (FAR is the ratio of the flow area through the screen divided by the total flow area of the duct.)
- The deflection of the gas flow as it passes through the screen.

The available information is not sufficient to develop a formulation to calculate the pressure losses associated with these effects. Thus the effect of non-perpendicular flow towards the porous baffles and porous media is excluded from the ESP model.

The collecting plates and the discharge wires are not the only structures in the collecting flow area. Safety plates, protecting maintenance personnel from the hammer rapping system, are installed at the beginning of the flow area and between the two electrical fields. These plates are about 1 m high and stretch over the whole width of the ESP. These plates have an effect on the fluid flow and are simulated as solid baffles at the designed locations (Figure 4.13).

4.5 The numerical model

The information obtained thus far can be used to assemble the ESP model. Figure 4.13 shows the total computational flow domain for the ESP model. The ESP model is equipped with an extra set of cells on top of the electrical fields to incorporate the effects of sneakage. The average dimension of one cell in the main flow region is about 0.25 m X 0.25 m X 0.25 m and the total number of cells and vertices used for the numerical model are presented in Table 4.2.

Geometrical Data	Vertices	Cells	Boundary cells	Surfaces
Value	517 907	491 664	58 114	1 500 835

Table 4.2: Number of cells and nodes.

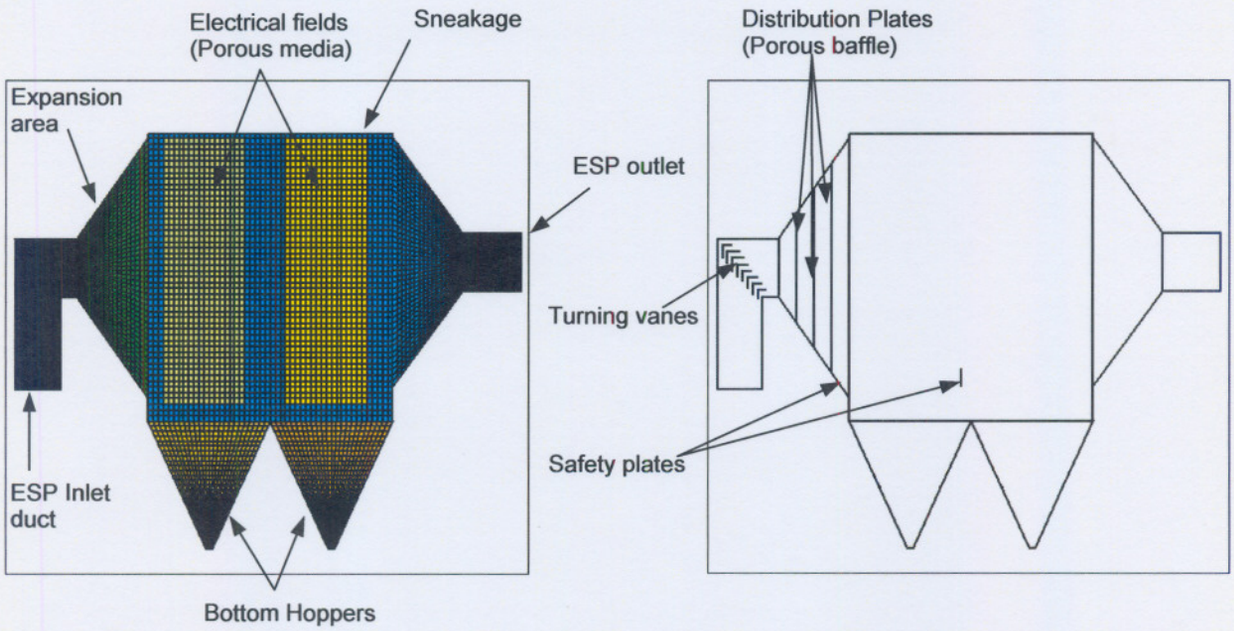

Figure 4.13: Complete ESP fluid flow model.

4.5.1 Boundary conditions

The boundary conditions are required to ensure the correct simulation of the gas flow through the ESP. Three major boundary conditions are applied in the simulation: the inlet conditions, the outlet conditions and symmetry.

Inlet

At the ESP inlet duct the velocity is specified in the y-direction. Three different velocities will be used during the simulations:

The design velocity (Appendix A): $v_2 = 13.2\ (m/s)$

The measured velocity inside a SASOL ESP will also be used. The ESP was not performing as designed and various measurements and investigations were conducted.

The measured velocity: $v_3 = 22\ (m/s)$

A minimum velocity value will also be used in order to investigate the effect of gas flow velocity on the fluid flow through the ESP.

The minimum velocity: $v_1 = 5\ (m/s)$

Outlet

The outlet of the ESP consists of a $3m$ long duct and a pressure boundary will be applied at the out side of the duct.

Pressure at outlet: $p_{out} = 0\ (Pa)$

Symmetry

Because of the symmetric nature of the ESP flow domain the flow domain was divided into two (Chapter 4.2). Thus symmetry boundary conditions must be applied at the section boundary. The grey area in Figure 4.2-b depicts the symmetry boundary for the numerical flow domain.

Other

The pressure gradient at the walls is set to zero. This is done for stability reasons.

The fluid flow is assumed to be incompressible and the fluid properties are defined as:

Density: $\rho_g = 1 \ (kg/m^3)$

Viscosity: $\mu_g = 1.85 \times 10^{-5} \ (Ns/m^2)$

The standard wall functions incorporated in Flo++ are also used. The velocity of the flow at the wall is zero because it is assumed that there is no slip present at the wall.

Typical values for the turbulence intensity and the turbulence length scale are used (STAR-CD Methodology Version 3.10, 1999: 8-3). The length scale can be taken as 0.1 times the characteristic passage dimension.

Thus: $L_{dr} = 1.284$

and the turbulence intensity: $I_{dr} = 0.01$

4.6 Closure

This chapter described the methodology followed to develop the numerical fluid flow model of the ESP. The flow domain of the ESP was reduced in order to identify an appropriate flow domain for the numerical model. Porous baffles approximate the distribution plates at the ESP inlet. The electrical fields inside the ESP are approximated by porous media. The effect of non-perpendicular flow towards the porous regions is excluded from this study.

The following chapter will discuss the results obtained from the ESP model. The effect of the distribution plates and the electrical fields on the gas flow through the ESP will be presented and discussed. The results of the numerical model will be compared with velocity measurements of an industrial SASOL ESP in order to evaluate the validity of the results.

CHAPTER 5

5. Results

5.1 Introduction

The previous chapter presented the development of a numerical model to simulate the gas flow through an industrial ESP. The computer resources available are not sufficient to simulate the full complex internal geometry of a precipitator. Thus certain assumptions and approximations were made in order to simplify the flow domain. The distribution plates in the ESP inlet and the electrical fields inside the ESP were approximated by porous baffles and porous mediums respectively.

This chapter discusses the results obtained from the numerical model. The effect of the distribution plates and the electrical fields on the gas flow through an ESP is presented. The lack of experimental investigations into the gas flow through industrial ESPs increases the difficulty to validate the results obtained from the numerical model. However the inlet velocity profile of the numerical model is compared with a measured velocity profile. The effect of the safety plates in front of and between the electrical fields is also discussed.

5.2 Turning vanes

This chapter will commence by showing the effect of the turning vanes in the inlet duct of the ESP. Figure 5.1-a shows the inlet duct with no turning vanes. The velocity vectors show how the gas flow moves through the duct towards the upper part of the duct outlet, resulting in a non-uniform gas flow which enters the ESP. A large area of recirculation flow is also visible at the lower section of the outlet. Figure 5.1-b shows the effect of numerical turning vanes used with the semi-elliptical grid. The non-uniformity of the outlet gas flow is reduced but the flow still seems to move to the upper section of the duct outlet. The recirculation flow at the lower section of the outlet is smaller than

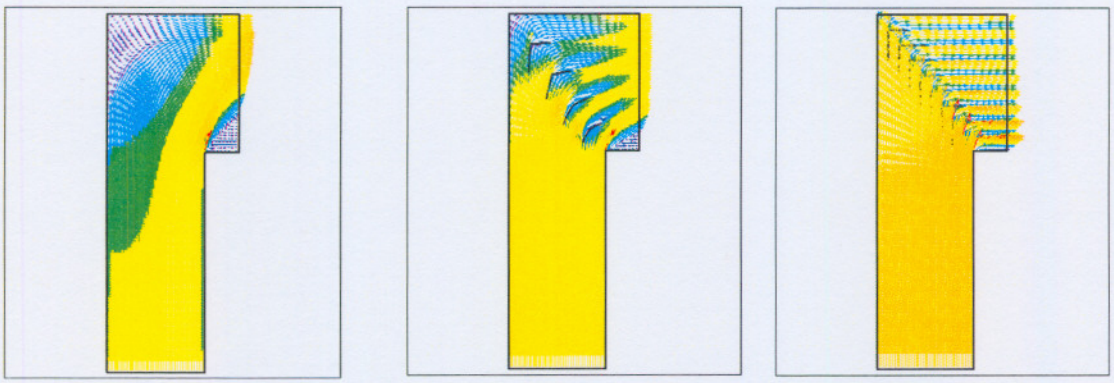

Figure 5.1: Effect of turning vanes. a) No turning vanes. b) Semi-elliptical grid turning vanes. c) Rectangular grid turning vanes.

with no turning vanes present. Figure 5.1-c shows the effect of the numerical turning vanes used with the rectangular grid. The outlet gas flow seems to be more uniform and the gas flow movement to the upper section of the duct is eliminated. The recirculation flow which is present with no turning vanes and with the semi-elliptical grid at the lower section of the outlet can cause large swirling inside the ESP. This recirculation flow is reduced to a minimum in the rectangular grid.

The results showed that the maximum outlet velocity with no turning vanes was 18.96 m/s. The maximum outlet velocity of the elliptical grid was 14.13 m/s and the maximum outlet velocity of the rectangular grid was 13.96 m/s. The lower maximum velocity shows that the flow is more evenly spread over the outlet than with the other geometries. The rectangular grid also showed almost no turbulence in the duct. The gas flow inside the flow domain is turbulent in nature. The turbulence described in this chapter refers to the large flow swirls and eddies resulting from the ESP geometry.

The pressure drop over the rectangular grid (61.2 Pa) was much larger than the pressure drop over the elliptical grid (40 Pa) and when no turning vanes were used. However the uniformity of the gas flow is much more important than the pressure drop. Thus the rectangular grid provides the best approximation for the inlet duct of the ESP.

5.3 Overview of simulation

Four different simulations were conducted in order to investigate the effect of the distribution plates (DP) and the electrical fields (EF) on the gas flow through the ESP. Every simulation was also done with three different inlet velocities in order to investigate the effect of flow velocity on the gas flow distribution through the precipitator. The four different simulations are:

- ESP with distribution plates and electrical fields. (industrial ESP)
- ESP with distribution plates but without electrical fields.
- ESP with electrical fields but without distribution plates.
- ESP without distribution plates and without electrical fields.

The results of the numerical model will mostly be shown in the xy-plane, the xz-plane and the symmetry plane of the ESP. Figure 5.2 shows the orientation of the different Cartesian planes which will be used to show the results. Velocity surface plots will be used to show the gas flow through the ESP. The duration, iterations, pressure drop (over the flow domain), maximum velocity (in the collecting flow area) and the outlet velocities of every simulation are shown in the following tables. The tables are followed by the velocity surface plots of the symmetry planes.

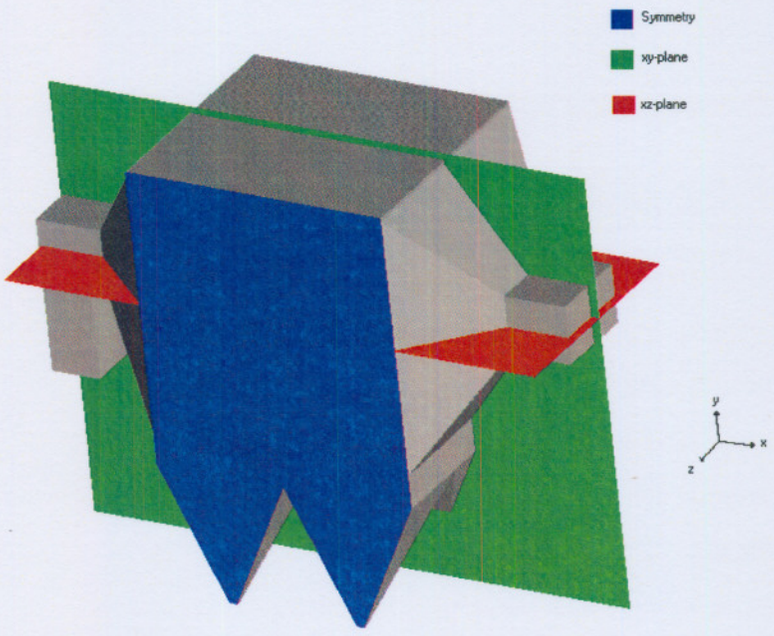

Figure 5.2: Symmetry, xy-plane and xz-plane in ESP geometry.

5.3.1 ESP with distribution plates and electrical fields.

Table 5.1 shows the overall results from the simulations of the ESP with the distribution plates and with the electrical fields. Figure 5.3 shows the velocity surface plots of the symmetry planes of these simulations.

Simulation	ESP with DP and EF		
Inlet velocity. (m/s)	$V_1 = 5$	$V_2 = 13.2$	$V_3 = 22$
Iterations	541	612	522
Duration (Hours)	4.2	5	4
Pressure Drop over flow domain. (Pa)	117.5	813.5	2255
Max. velocity in main flow area. (m/s)	0.5575	1.478	2.466
Outlet velocity (m/s)	5.368	14.16	23.6

Table 5.1: ESP with DP and EF.

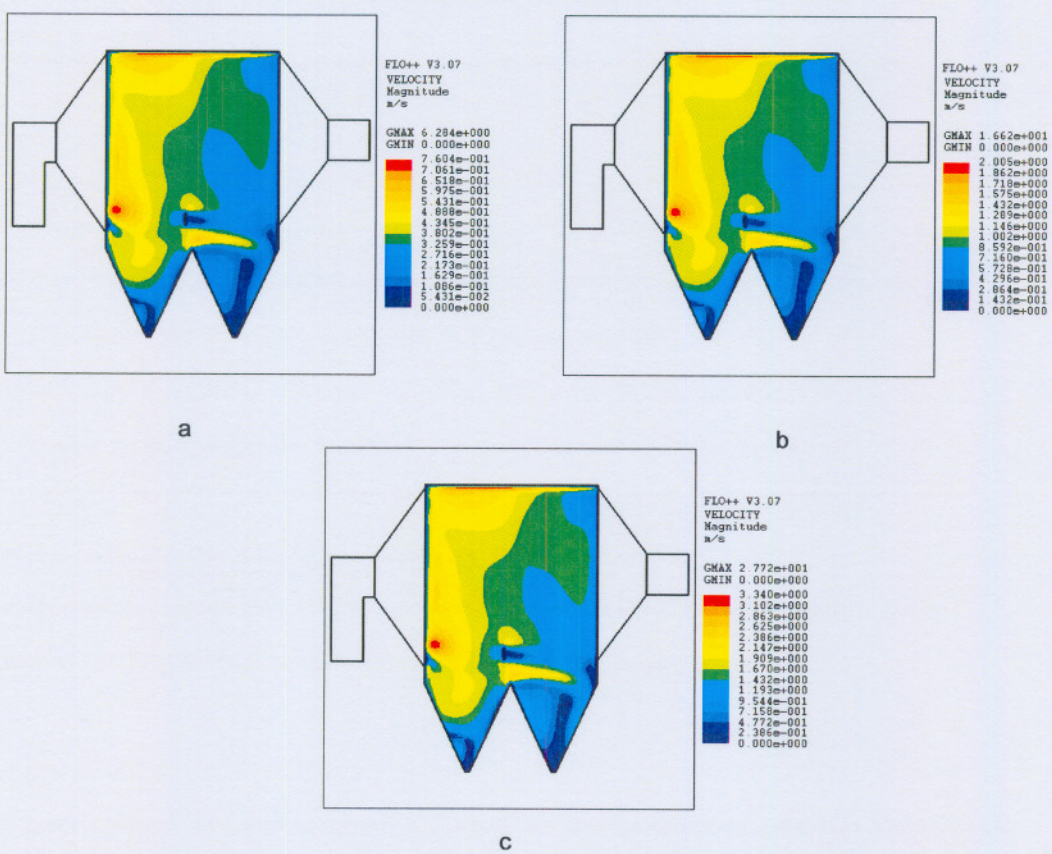

Figure 5.3: ESP model with DP and EF. a) Symmetry velocity surface plot, with (V_{in} = 5 m/s) b) Symmetry velocity surface plot, with (V_{in} = 13.2 m/s) c) Symmetry velocity surface plot, with (V_{in} = 22 m/s)

5.3.2 ESP with distribution plates and without electrical fields.

Table 5.2 shows the overall results from the simulations of the ESP with the distribution plates but without the electrical fields. Figure 5.4 shows the velocity surface plots of the symmetry planes of these simulations.

Simulation	ESP with DP and without EF		
Inlet velocity. (m/s)	$V_1 = 5$	$V_2 = 13.2$	$V_3 = 22$
Iterations	812	739	789
Duration (Hours)	9.2	8.1	9.1
Pressure Drop over flow domain. (Pa)	117.4	812.6	2253
Max. velocity in main flow area. (m/s)	0.8648	2.297	3.797
Outlet velocity (m/s)	5.401	14.23	23.71

Table 5.2: ESP with DP and without EF.

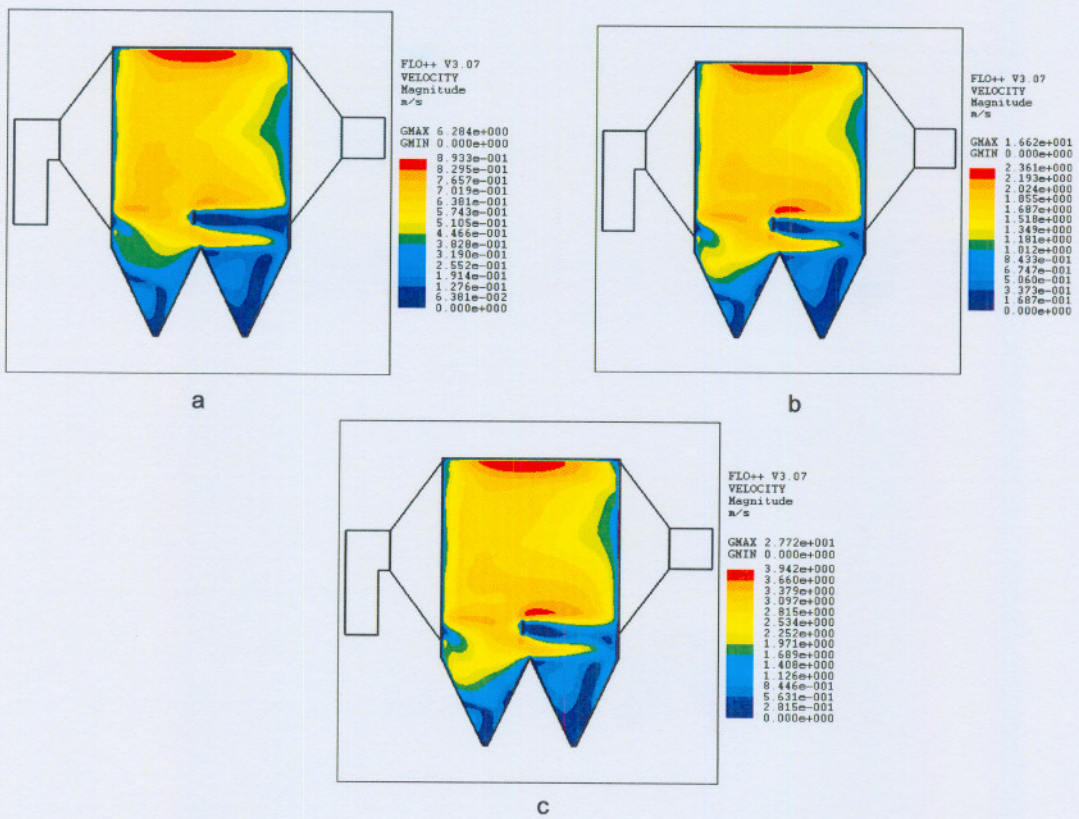

Figure 5.4: ESP model with DP and without EF. a) Symmetry velocity surface plot, with (V_{in} = 5 m/s) b) Symmetry velocity surface plot, with (V_{in} = 13.2 m/s) c) Symmetry velocity surface plot, with (V_{in} = 22 m/s)

5.3.3 ESP with electrical fields and without distribution plates.

Table 5.3 shows the overall results from the simulations of the ESP with the electrical fields but without the distribution plates. Figure 5.5 shows the velocity surface plots of the symmetry planes of these simulations.

Simulation	ESP with EF and without DP		
Inlet velocity. (m/s)	$V_1 = 5$	$V_2 = 13.2$	$V_3 = 22$
Iterations	329	309	364
Duration (Hours)	2.5	2.4	2.8
Pressure Drop over flow domain. (Pa)	23.58	163.4	452.7
Max. velocity in main flow area. (m/s)	1.771	4.693	7.824
Outlet velocity (m/s)	5.372	14.17	23.61

Table 5.3: ESP with EF and without DP.

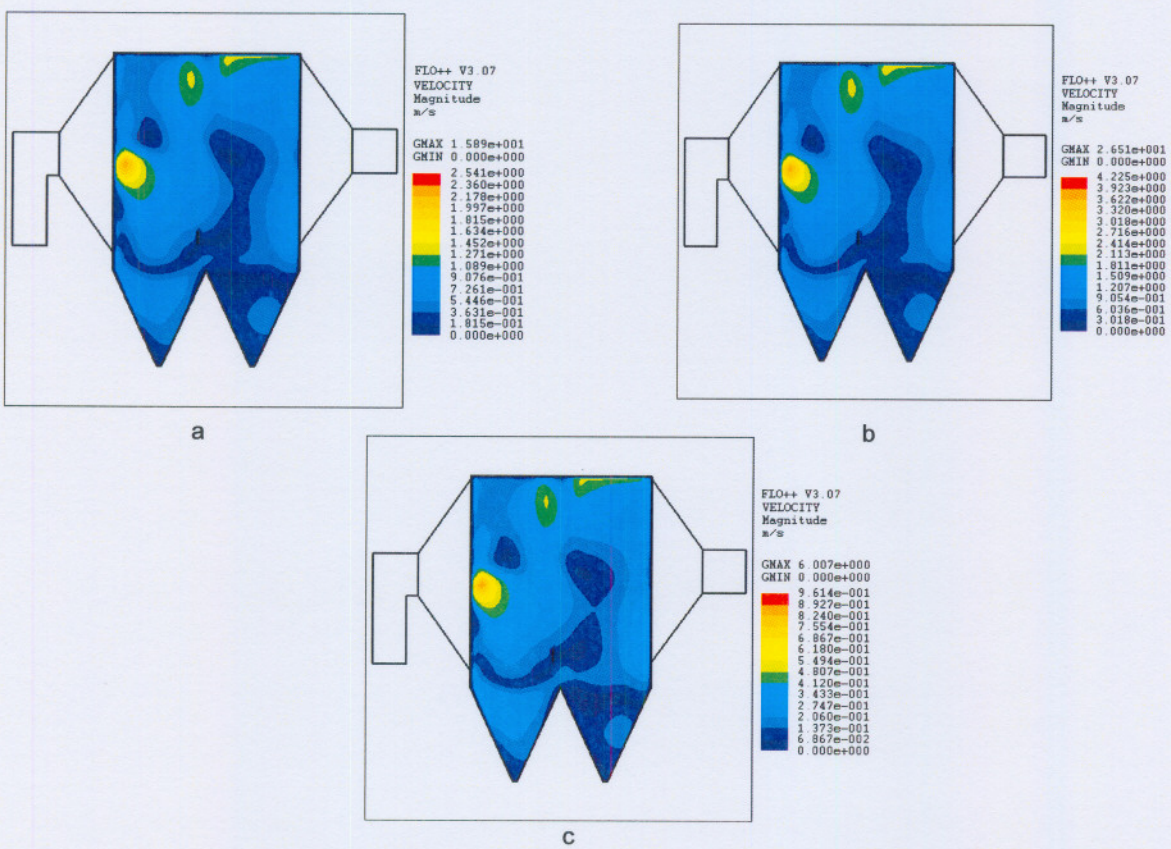

Figure 5.5: ESP model with EF and without DP. a) Symmetry velocity surface plot, with (V_{in} = 5 m/s) b) Symmetry velocity surface plot, with (V_{in} = 13.2 m/s) c) Symmetry velocity surface plot, with (V_{in} = 22 m/s)

5.3.4 ESP without electrical fields and without distribution plates.

Table 5.4 shows the overall results from the simulations of the ESP without the electrical fields and without the distribution plates. Figure 5.6 shows the velocity surface plots of the symmetry planes of these simulations.

Simulation	ESP without EF and without DP		
Inlet velocity. (m/s)	$V_1 = 5$	$V_2 = 13.2$	$V_3 = 22$
Iterations	3079	3106	3247
Duration (Hours)	32.8	33	34.7
Pressure Drop over flow domain. (Pa)	21.42	148.6	411.9
Max. velocity in main flow area. (m/s)	3.686	9.704	16.15
Outlet velocity (m/s)	5.646	14.89	24.82

Table 5.4: ESP without EF and without DP.

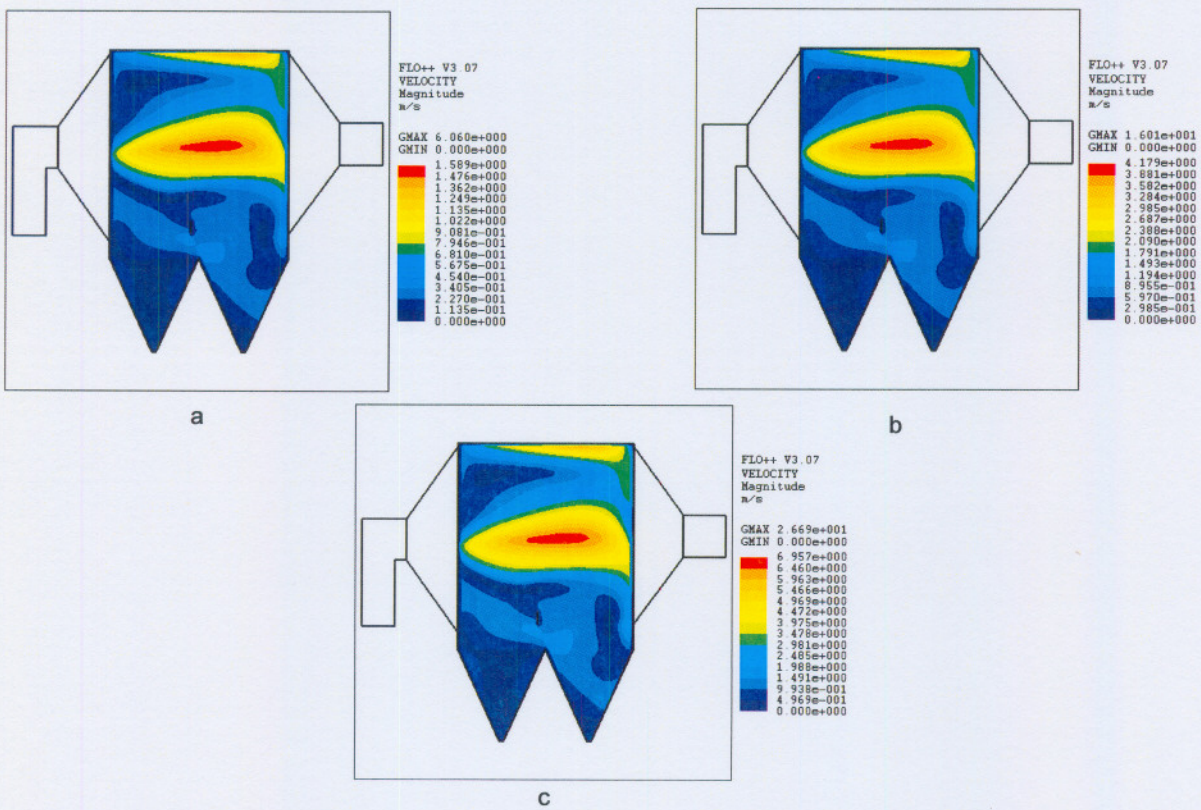

Figure 5.6: ESP model without EF and without DP. a) Symmetry velocity surface plot, with (V_{in} = 5 m/s) b) Symmetry velocity surface plot, with (V_{in} = 13.2 m/s) c) Symmetry velocity surface plot, with (V_{in} = 22 m/s)

5.3.5 Discussion

The results have shown the importance of the distribution plates. The velocities inside the ESPs with the distribution plates (Tables 5.1 and 5.2) were the lowest. The gas flow velocity was reduced from 4.693 (m/s) (Table 5.3) to 1.478 (m/s) (Table 5.1) in the presence of the distribution plates. Thus the lower gas flow velocities allow more treatment time for the ash particles inside the collecting ducts. The velocity surface plots also show that the gas flow is more evenly distributed through the ESP when distribution plates were present (Figure 5.3 and Figure 5.4). The velocity surface plots with no distribution plates (Figure 5.5 and Figure 5.6) show large variations in colour, which indicates that the flow is not equally distributed through the collecting flow area. The distribution plates also have the largest effect on the pressure drop over the ESP. The results have shown that the pressure drop is five times larger in the presence of distribution plates, than without it. The electrical field region reduces the gas velocity through the ESP but has almost no effect on the pressure drop over the flow domain with distribution plates, and little effect on pressure drop without distribution plates.

The results also show that the different gas flow velocities have no major effect on the gas flow patterns. Higher inlet gas flow velocities cause an obvious increase in the pressure drop and the velocity inside the collecting area. The rest of the results in this chapter will be confined to the design inlet velocity, $V_2 = 13.2$ m/s. (See Appendix B for the remainder of the results)

The effect of the distribution plates on the gas flow through the ESP will be discussed in more detail because of its importance.

5.4 Distribution plates

The main purpose of the distribution plates is to expand the gas flow over the entire collecting area and to reduce the maximum gas flow velocity. Figure 5.7 shows the gas flow through the ESP without distribution plates and without electrical fields. This can be compared with the gas flow through the

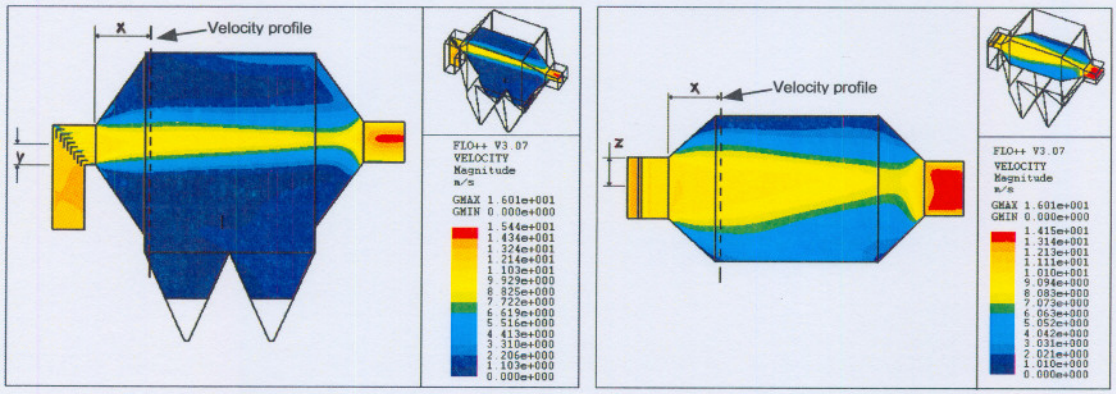

a b

Figure 5.7: Gas flow through ESP without DP and without EF. a) Gas flow in xy-plane. b) Gas flow in xz-plane

ESP with distribution plates and without electrical fields (Figure 5.8) in order to illustrate the effect of the distribution plates on the gas flow. The gas flow passes through the ESP with no restrictions, resulting in high gas flow velocities and a non-uniform gas flow distribution (Figure 5.7). The gas flow is already well expanded over the flow domain when it passes the first distribution plate, illustrated by Figure 5.8. The best way to illustrate the effect of the distribution plates is to compare the velocity profile (at the inlet of the collecting area) of the distribution plates with the velocity profile without the distribution plates. Figure 5.7 shows the location of the velocity profiles which are determined in order to compare the two profiles. Velocity measurements of an industrial ESP (in the same region) were provided by SASOL personnel and will be used to validate the results obtained in the simulation.

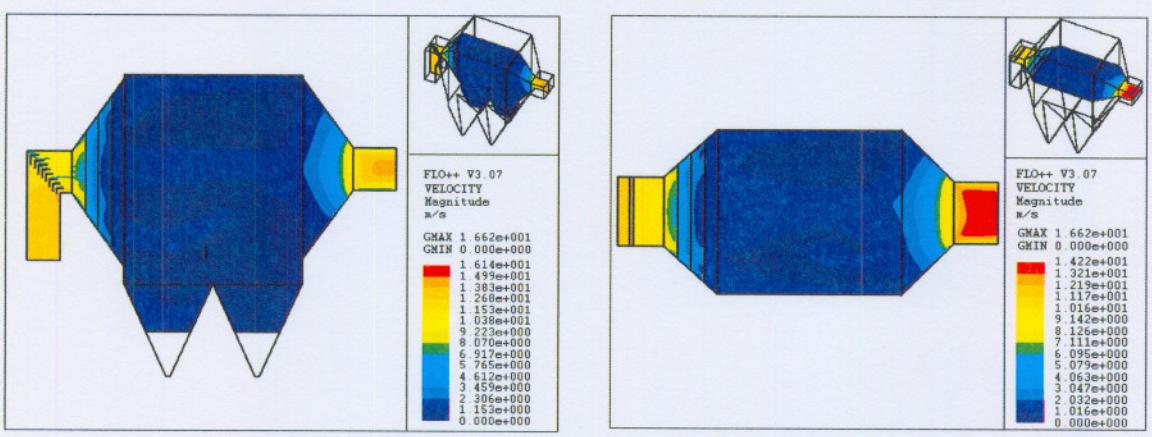

a b

Figure 5.8: Gas flow through ESP with DP and without EF. a) Gas flow in xy-plane. b) Gas flow in xz-plane

Figure 5.9 shows the measured velocity profile, the simulated velocity profile with distribution plates and the simulated velocity profile without the distribution plates in the xy-plane. Figure 5.10 shows the same velocity profiles in the xz-plane. The simulation results are in reasonable good agreement with the measured values, for the xy-plane and for the xz-plane. The distribution plates reduce the velocity significantly and the gas flow is evenly distributed over the inlet. The reduction in velocity values because of the effect of the distribution plates is illustrated in Table 5.5. The simulated average velocity, 1.22 (m/s) (Table 5.5) corresponds well to the design velocity in the ESP, 1.28 (m/s) (Appendix A).

Velocity profiles	Measurements	With DP	Without DP
Average velocity (m/s)	1.29	1.22	2.97
Maximum velocity (m/s)	1.3	2.05	9.83

Table 5.5: Velocity values of velocity inlet profiles.

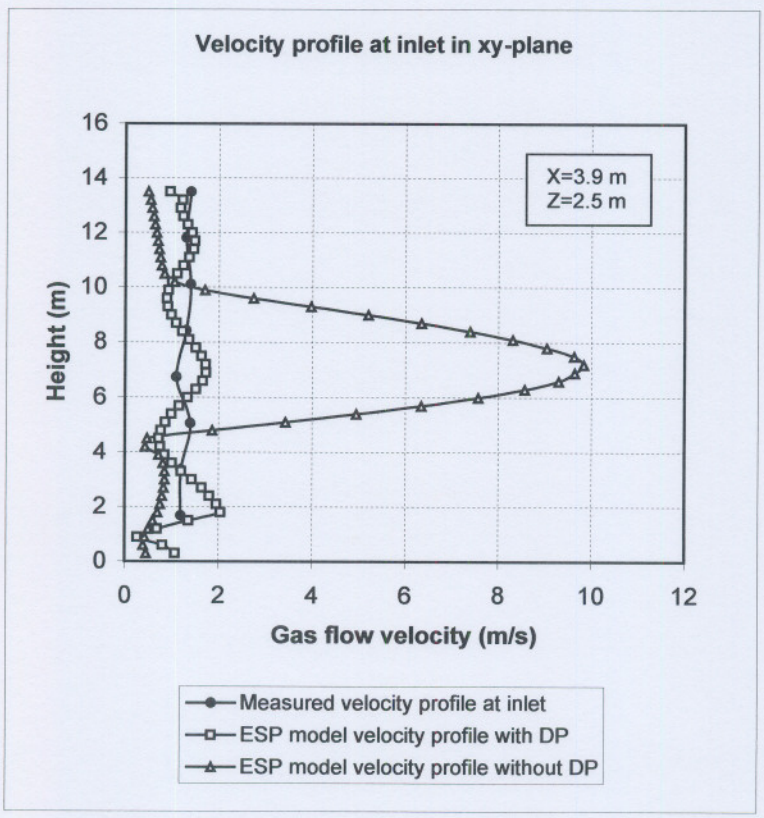

Figure 5.9: Measured velocity profile, simulated velocity profile and velocity profile without distribution plates in the xy-plane.

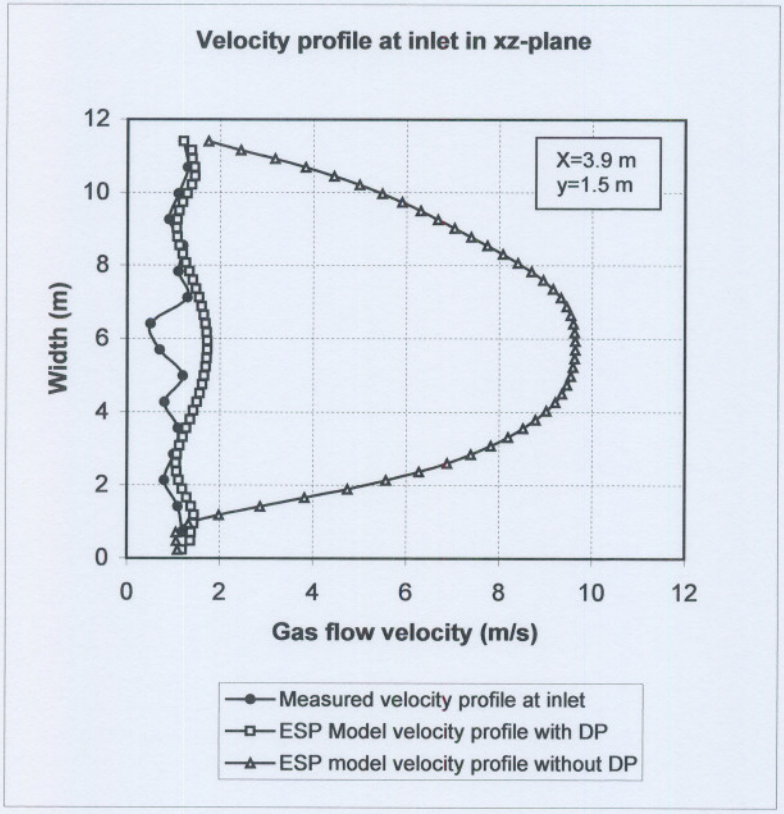

Figure 5.10: Measured velocity profile, simulated velocity profile and velocity profile without distribution plates in the xz-plane.

The variation in the velocity profile at the lower section of the xy-plane (Figure 5.9) can be attributed to the effect of the safety plates at the bottom of the collecting flow area.

The pressure drop over the expansion area also describes the effect of the distribution plates. Figure 5.11-a shows how the pressure drops significantly when the gas flow is affected by the distribution plates. Figure 5.11-b shows the velocity vectors through the ESP expansion area and shows how the distribution plates manipulate the flow in order to expand the gas flow over the entire flow domain.

Thus the distribution plates reduce the velocity inside the collecting duct and expand the gas flow through the entire collecting flow area.

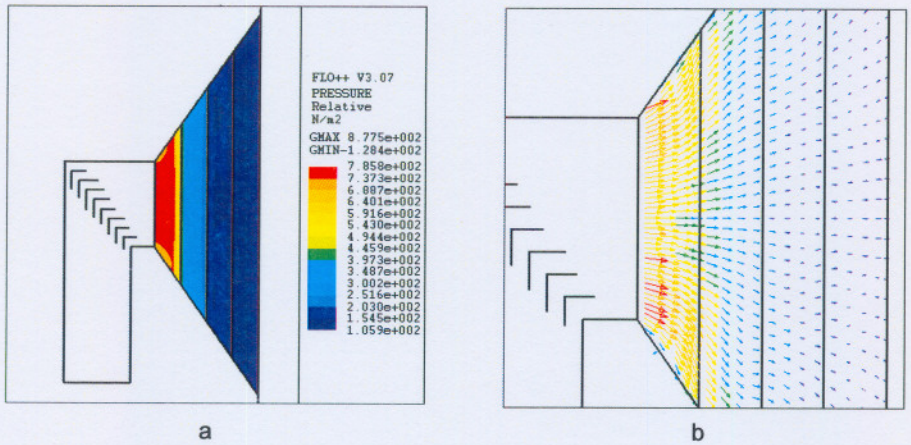

Figure 5.11: a) Pressure drop over distribution plates. b) Velocity vectors in expansion area.

5.5 Electrical fields

Comparing Figure 5.7 with Figure 5.12 illustrates the effect of the electrical fields on the gas flow through the ESP. The gas flow slows down considerably as it approaches the electrical fields. Figure 5.13-a shows the gas flow through the collecting area with the distribution plates and with the electrical fields. Figure 5.13-b also shows the gas flow through the collecting area, but without the electrical fields. The gas flow through the collecting area without the electrical fields is much more turbulent (swirling) than the gas flow with the electrical fields present.

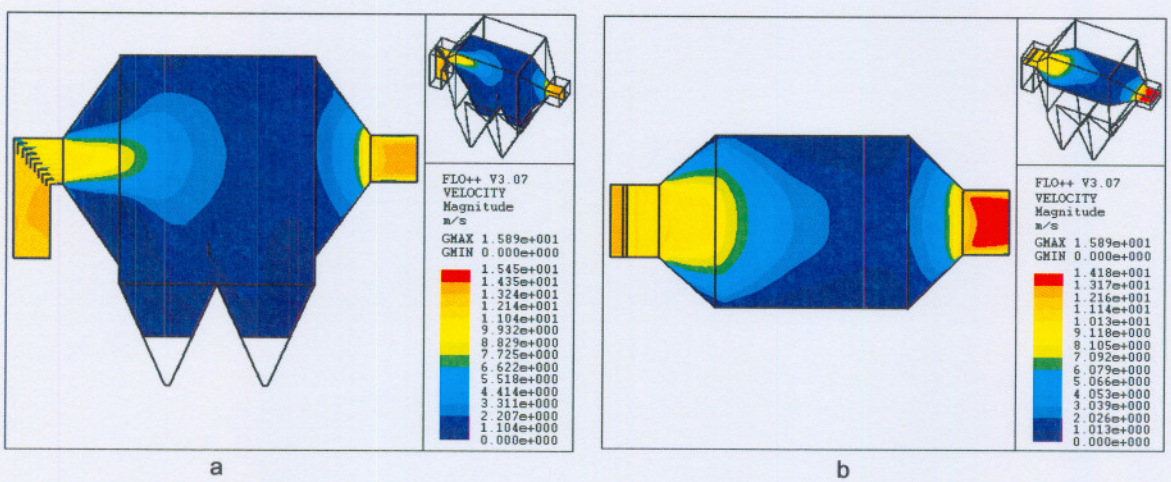

Figure 5.12: Gas flow through ESP with EF and without DP. a) Gas flow in xy-plane. b) Gas flow in xz-plane

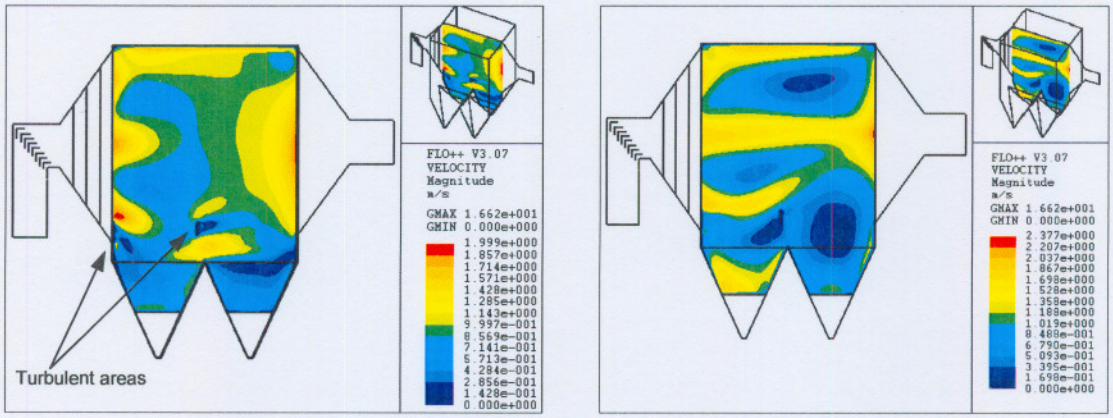

a b

Figure 5.13: a) Gas flow through collecting area with DP and EF. b) Gas flow through collecting area with DP and without EF.

5.6 Safety plates

Turbulent flows (eddying flows) and swirls inside the ESP must be avoided in order to ensure good quality gas flow through the precipitator. The safety plates at the inlet of the collecting area and between the electrical fields are located perpendicular to the gas flow. This can cause turbulence (swirling) in the collecting flow domain, which can have a detrimental effect on the ESP performance. Figure 5.13-a shows the turbulent areas caused by the steel plates. Figure 5.14 show the gas flow velocity vectors surrounding the safety plates. Circulation flows are visible behind the steel plates.

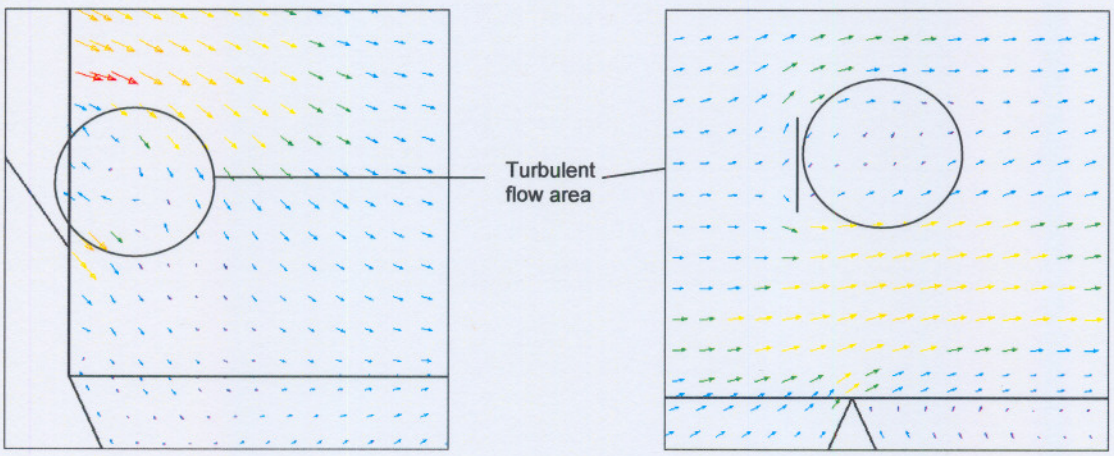

a b

Figure 5.14: a) Turbulent flow caused by inlet steel plate. b) Turbulent flow caused by steel plate between electrical fields.

The effect of the steel plates can also be illustrated on the symmetry plane of the simulation with distribution plates but without electrical fields (Figure 5.4). The large blue areas behind the safety plates show the high levels of turbulence (swirling) caused by the steel plates.

The safety plates also create jets at the bottom of the electrical fields (Figure 5.3). These jets can cause the gas flow to move underneath and not through the electrical fields, because the collecting plates do not extend over the entire height of the ESP. Thus some of the fly-ash particles will move through the ESP without being charged and collected by the collecting area. The jets will also cause some of the falling fly-ash (from the plates) to be re-entrained into the gas stream. Therefore, the jets can cause lower ESP collection efficiencies.

However the turbulence scale caused by the steel plates is small in comparison with the large flow domain of the ESP. Thus this turbulence will not have a large effect on the collection efficiency, but it must be limited to the minimum.

5.7 Closure

In this chapter the results obtained form the ESP model were discussed. The distribution plates in the ESP inlet succeed in their purpose. The maximum gas flow velocity is reduced and the gas flow is well distributed over the entire flow domain. The inlet velocity profiles are in reasonable agreement with measured velocities from an SASOL ESP.

The main objective of this study is to investigate if the methodology followed during this study can be used to predict gas flow patterns inside an ESP. The future objective is to extend the capabilities of the model in order to simulate larger flow domains and more complex geometries when adequate resources are available.

The following chapter presents the conclusions reached during this study and the recommendations for future research and numerical modelling of a flue gas precipitator.

CHAPTER 6

6. Conclusions and Recommendations

6.1 Introduction

This chapter consists of a short summary of this study, followed by the most important conclusions that can be made. Recommendations for further research complete the chapter.

6.2 Summary

Air pollution is a major concern in today's civilization and prevention methods have grown to a world wide business. Electrostatic precipitation is one of the most important processes to limit air pollution to a minimum. Electrostatic precipitators use electrostatic forces to extract fly-ash particles from industrial flue gasses. Investigations and research are continuously conducted on electrostatic precipitators in order to improve their performance.

The literature survey showed that the influence of the gas flow on the overall performance of an electrostatic precipitator is one of the most important factors. Three dimensional modelling is not typical in ESP modelling because of the complexity of the precipitation process and the lack of sufficient computer resources. Research and investigation are more focussed on the electrostatic conditions inside an ESP than on the gas flow through the precipitator. More research must be done on secondary effects like re-entrainment, back corona and ash resistivities which can have a degrading effect on the precipitator efficiency.

The main objective of this study was to develop a three-dimensional numerical model in order to predict the gas flow patterns inside a precipitator. The study was only concerned with the fluid flow, thus the mass and momentum laws

were applied. The model uses the finite volume method together with the SIMPLE algorithm to solve the governing equations.

The internal structures were too complex and the flow domain is too large for the available computer resources to simulate the gas flow through the precipitator. Thus certain assumptions and approximations were made in order to simplify the ESP flow domain. The distribution plates reduce the gas flow velocities and expand the gas flow over the entire flow region. The distribution plates and the collecting electrical flow regions were approximated by porous baffles and porous mediums respectively. The effect of non-normal flow approaching the porous regions was excluded from this study.

The previous chapter discussed the results obtained from the ESP model and investigated the effect of the distribution plates and the electrical fields on the gas flow through the ESP. The simulated inlet velocity profiles were in relative good agreement with measured velocity profiles obtained from an industrial SASOL ESP. The distribution plates reduced the maximum inlet velocity (to the collecting flow area) from 9 (m/s) to 2 (m/s). It was also shown that the flow was distributed more evenly over the entire flow domain because of the distribution plates.

6.3 Conclusions

As previously mentioned the main objective of this study was to develop a three-dimensional numerical flow model to simulate the gas flow through a precipitator. The model was used to investigate if the methodology followed during this study can be used to predict gas flow patterns inside an ESP.

It was concluded that the model could be used to predict the flow and this methodology can therefore be used in future models that will be able to simulate the entire ESP flow domain and more complex internal geometries. The simulated velocity values were in relative good agreement with measured velocities but further improvements in the model are necessary.

6.4 Recommendations

During the development stages of the numerical model major assumptions and approximations were made. Thus the model can not be used to draw definite conclusions concerning the gas flow through a precipitator. In order to develop a more appropriate numerical model certain adjustments and improvements are necessary for future use:

- The incorporation of additional loss factors into the model to account for the effect of non-normal flow towards the porous baffles and porous mediums.

- The incorporation of particle trajectories into the gas flow model, in order to investigate the effect of fly-ash particles on the gas flow through an ESP.

- The development of a more complete model, which account for the entire flow domain of an ESP. The development of more accurate approximations for the distribution plates and the electrical fields.

- More experimental studies and measurements of the gas flow through an ESP are required to fully validate the results of the model.

- The incorporation of a loss factors which account for the overall effect of the electrostatic conditions on the gas flow through the precipitator.

- More research is required on the effect of aspects such as ash resistivity, re-entrainment, back corona and pulsed energization on the gas flow through an ESP.

REFRENCES

BIBBO, P.P. 1995. EPRICON : Agentless Flue Gas Conditioning For Electrostatic Precipitators. *Proceedings of the American Power Conference*, **51-1**: 32-37.

CHANG, C. & BAI, H. 1999. An experimental study on the performance of a single discharge wire-plate Electrostatic Precipitator with Back Corona. *Journal Aerosol Sci.*, **30**(3): 325-340.

CHOI, B.S., FLETCHER, C.A.J. 1997. Computation of Particle Transport in an Electrostatic Precipitator. *Journal of Electrostatics*, **40 & 41**: 413-418.

DAVIDSON, J. H. & McKINNEY, P. 1991. EHD Flow Visualization in the Wire-Plate and Barbed Plate Electrostatic Precipitator. *IEEE Transactions on Industry Applications,* **27(1)**: 154-160.

DE NEVERS, N. 1995. *Air Pollution Control Engineering.* 1st ed. Singapore: McGraw-Hill. : 217-230

DINELLI, G., BOGANI, V. & REA, M., 2002. Enhanced Precipitation Efficiency of Electrostatic Precipitators by Means of Impulse Energization. *IEE Transactions on Industry Applications*, **55 (2)**: 323-33.

DU TOIT, C.G. & KOTZE, J.C.B. 1990. The Modelling of the Air Flow through a Grill and Radiator Core. *Proceedings of the Symposium on Finite Element Methods in S.A.,* : 51-62.

GALLIMBERTI, I. 1998. Recent advancements in the physical modelling of electrostatic precipitators. *Journal of Electrostatics*, **43** : 219-247.

HAO, J., HE, K. & CHAO, H., 1990. Calculation of Electric Field Strength Distribution for new Electrostatic Precipitator Discharge Electrode Designs. *Journal of the Air & Waste Management Association*, **40**: 1510-1513.

HATI, S.K. & SINGIRESU, S.R. 2001. Game theory approach for the design of an optimal air pollution control system for thermal power plants. *International Journal of Environment and Pollution*, **15 (5)** : 505-516.

JANSE VAN RENSBURG, C. & VAN STADEN, M.P. 2003. Proposed methodology for the modelling of expanded metal screens using variable resistance factors. *Paper accepted for presentation: Fourth South African Conference on Applied Mechanics, 19-21 January 2004, Johannesburg.*, 8p.

JEDRUSIK, M., GAJEWSKI, J.B. & SWIERCZOK, A.J. 2001. Effect of the particle diameter and corona electrode geometry on the particle migration velocity in electrostatic precipitators. *Journal of Electrostatics*, **51-52**: 245-251.

KATZ, J. 1979. *The Art of Electrostatic Precipitation.* 1st ed. Pennsylvania: S&S Printing Company, Inc. 350p

KIM, S.H. & LEE, K.W. 1999. Experimental study of electrostatic precipitator performance and comparison with existing theoretical prediction models. *Journal of Electrostatics,* **48**: 3-25.

KISS, I. & BERTA, I. 2001. New concept of ESP modelling based on fuzzy logic. *Journal of Electrostatics*, **51-52** : 206-211.

KOGELSCHATZ, U. & EDGAR, W.E. 2001. Advanced Computer Modelling of Electrostatic Precipitators. *Computer Modelling of an Electrostatic Precipitator*: 32-37, November.

KRUGER, J. H. 1999. *Euler/Lagrangian modelling of an electrostatic precipitator.* Potchefstroom : University of Potchefstroom for Christian Higher Education. (Thesis-M.Eng.). 99p

LE GRANGE, L.A. 1999. *Flo++ CFD Softwate, Users's Manual (electronic version).* 2nd ed. Potchefstroom: Softflo, cc.

LEIBACHER, U. 1996. Improving heavy dust laden airflow in electrostatic precipitators. *World cement. London: Eyre & Spottiswoode Publications Ltd*, **27 (10)** : 47-50.

LEONARD, G. A., MITCHNER, M. & SELF, S. A., 1980. Particle Transport in Electrostatic Precipitators. *Atmosphere Environment*, **14** : 1289-1299.

LEONARD, G. A., MITCHNER, M. & SELF, S. A., 1983. An experimental study of the electrohydrodynamic flow in electrostatic precipitators. *Journal of Fluid Mechanics*, **127** : 123-140.

MACARIE, R. & MARTIN, D. 1997. New technologies for the electrostatic precipitators pulsed energization in energetics. *Energy Convers. Mgmt.*, **38 (5)** : 511-516.

MEROTH, A. M. 1997. *Numerical electrodydrodynamics in electrostatic precipitators.* Karlsruhe : Universität Fridericiana Karlsruhe. (Thesis-D.Phil.). 150 p.

MILLER, J., HOFERER, B. & SCHWAB, A.J. 1998. The impact of corona electrode configuration on Electrostatic Precipitator performance. *Journal of Electrostatics*, **44**: 67-75.

MIZERACZYK, J., KOCIK, M., DEKOWSKI, J., DORS, M., PODLINSKI, J., OHKUBO, T., KANAZAWA, S. & KAWASAKI, T., 2001. Measurements of the velocity field of the flue gas flow in an electrostatic precipitator model using PIV method. *Journal of Electrostatics*, **51-52** : 272-277.

NAVARRETE, B., CANADAS, L., CORTéS, V., Salvador, L. & Galindo, J. 1997. Influence of plate spacing and ash resistivity on the efficiency of electrostatic precipitators. *Journal of Electrostatics*, **39**: 65-81.

PALMER, A. K. 1996. *Computational Fluid Dynamic Software Comparison and Electrostatic Precipitator Modelling.* Chico : California State University. (Thesis-M.Sci.). 84p

RAMSDELL, R. G. 1968. Design criteria for Precipitators for modern central station power plants. *Proceedings of the American Power Conference. Chicago*, 30 : 444-449.

SCHMIDLE, K., BURTSCHER, H., KLIPPEL, N. & STUTZ, S. 1995. Precipitation of fly-ash of different resistivity in a laboratory electrostatic precipitator. *J. Aerosol Sci.*, **26**: S15-S16.

SERFONTEIN, J. B. 2000. *The Calculation of Unsteady 2-Dimensional Flow over a Cylinder with Finite Volume Method.* Potchefstroom : University of Potchefstroom for Christian Higher Education. (Thesis-M.Eng.). pp 33-44

SOLDATI, A., 2000. On the Effects of Electrohydrodynamic flows and Turbulence on Aerosol transport and Collection in Wire-plate Electrostatic Precipitators. *Journal Aerosol Sci.*, **31 (3)**: 293-305.

SOLDATI, A., ANDREUSSI, P. & BANERJEE, S., 1993. Direct Simulation of Turbulent Particle Transport in Electrostatic Precipitators. *AIChE Journal*, **39 (12)**: 1910-1919.

STAR-CD Methodology Version 3.10, 1999. : Computational Dynamics Limited. p 8-1 to 8-8

YAMAMOTO, T. & SPARKS, L. 1986. Numerical Simulation of Three-Dimensional Tuft Corona and Electrohydrodynamics. *IEEE Transactions on Industry Applications,* **IA-22(5)**: 880-885.

TULSA, O. 1998. Lower catalyst resistivities raise precipitator efficiencies. Oil & Gas Journal, **96**: 78-79.

VARONOS, A., ANAGNOSTOPOULOS, J. & BERGELES, G., 2002. Prediction of the cleaning efficiency of an electrostatic precipitator. *Journal of Electrostatics*, **55**: 111-133.

VERSTEEG, H. K. & MALALASEKERA, W. 1995. *An Introduction to Computational Fluid Dynamics. The Finite Volume Method.* 1st ed. Essex : Addison-Wesley. 257 p.

WHITE, H.J. 1963. *Industrial Electrostatic Precipitation.* 1st ed. USA: Addison-Wesley Publishing Company, Inc. 376p

ZHIBIN, Z. & GUOQUAN, Z. 1994. Investigations of the Collection Efficiency of an Electrostatic Precipitator with Turbulent Effects. *Aerosol Science and Technology,* **20**: 169-176.

APPENDIX A: Design Specifications

The appendix presents the design specifications for an industrial SASOL ESP.

1. Specification Data Sheets 2.

Sasol THREE Block 2

FLUOR
SHEET NO. 1 of 2 REV.
BY Lurgi DATE 10.6.81
INQ. NO.
P.O. NO. EX 20/897 529
PAGE 1 OF 2

SASOL III PROJECT
SOUTH AFRICAN COAL, OIL AND GAS CORPORATION LTD.

SPECIFICATION DATA SHEET

ELECTROSTATIC PRECIPITATOR

ITEM NO 243-FT 101-801 SERVICE Flue gas dust collector

PROCESS DATA

DUST ANALYSIS

MATERIAL SPECIFIC GRAVITY	2,4 **	g/cm³
DRY BULK DENSITY	800 **	kg/m³
MOISTURE CONTENT	< 1 **	% BY WT.
DUST LOADING AT INLET	29,200	mg/m³ NTP
MAX. ALLOWABLE DUST LOADING AT OUTLET	200	mg/m³ NTP

PARTICLE SIZE DISTRIBUTION BY WEIGHT: **

SUBMICRON	%	< 3 MICRON	20 %
3–5 MICRON	20 %	5–10 MICRON	25 %
10–20 MICRON	20 %	OVER 20 MICRON	15 %

CHARACTERISTICS: **

ABRASIVE	( )	TOXIC	( )
CORROSIVE	( )	COMBUSTIBLE	( )
STICKY	(X)	EXPLOSIVE	( )
FIBROUS	( )	ALKALINE	( )
HYGROSCOPIC	(X)	OTHERS	( )

DUST COMPOSITION:
Unburnt Carbon 4%

GAS ANALYSIS

		DESIGN	NORMAL	MAXIMUM
VOLUME	m³/s	401.2	–	384
TEMPERATURE	°C	226	–	205
MOISTURE	% BY WT.	–	–	7.4
DENSITY	kg/m³	0.568	–	0.595

CHARACTERISTICS: TOXIC ( ) COMBUSTIBLE ( ) EXPLOSIVE ( ) CORROSIVE (X) CONDENSIBLE (X) OTHERS ( )

CHEMICAL COMPOSITION	% VOLUME	% WEIGHT
H_2O	–	7.4
CO_2	–	20.7
SO_2	–	0.2
O_2	–	3.4

GAS DUCT VELOCITY 13.2 m/s
GAS PRECIPITATOR VELOCITY 1.28 m/s

DESIGN PRESSURE	± 5.10 kPa	POSITIVE (X	NEGATIVE (X)
OPERATING PRESSURE	– 2.45 kPa	POSITIVE ( )	NEGATIVE (X)
PRESSURE DROP ACROSS PRECIPITATOR	0.125 kPa		
MIGRATION OR DRIFT VELOCITY	5.55 cm/s		
RETENTION OR TREATMENT TIME	12 SECS.		
GUARANTEED EFFICIENCY	99.32 %		

MECHANICAL DESIGN

NUMBER OF PRECIPITATORS	8
CHAMBERS/PRECIPITATOR	1
FIELDS: (NUMBER AND LENGTH)/PRECIPITATOR	4/4.32 m
CELLS: NUMBER/PRECIPITATOR	76
BUS SECTIONS: NUMBER/PRECIPITATOR	8
CASING MATERIAL AND THICKNESS (mm)	USt37.2; ≥ 5
NUMBER OF HOPPERS/PRECIPITATOR	12
HOPPER MATERIAL AND THICKNESS (mm)	USt37.2; 5
MINIMUM HOPPER VALLEY ANGLE	55°
TOTAL HOPPER CAPACITY/PRECIPITATOR (m³)	1272
HOPPER ACCESSORIES (LIST)	Level Indicator + Alarm 43 LSH 1281 + 1293
LEVEL ALARM	YES (X) NO ( )
INSULATOR COMPARTMENT (MATERIAL & THICKNESS)	USt 37.2; 5 mm
NUMBER OF INSULATOR COMPARTMENTS/PRECIPITATOR	20
NUMBER OF NOZZLES/PRECIPITATOR (INLET/OUTLET)	2/2

SURFACE AREA/PRECIPITATOR (sq.m.)
ROOF 840 sq.m.

HOPPER	1360	sq.m.
SHELL	650	sq.m.
OTHER	840	sq.m.

PRECIPITATOR INTERNAL GAS DISTRIBUTION DEVICES:
TYPES perforated plates
QUANTITY & LOCATION/PRECIPITATOR 3 located in inlet nozzels
MATERIAL & THICKNESS USt 37.2; 5 mm
NUMBER & TYPE RAPPERS 2, Rotohit

NUMBER, TYPE AND SIZE OF ACCESS DOORS/PRECIPITATOR

ROOF	–	
SHELL	5	575 mm ø
HOPPER	12	575 mm ø
INSULATOR COMPARTMENTS		20; 420x585 mm
NOZZLE	2	575 mm ø

VOLUME : 6
CHAPTER : 4.4.3.1. D.1
PAGE : 1
REV :

SASOL III PROJECT
SOUTH AFRICAN COAL, OIL AND GAS CORPORATION LTD.

[2] Sasol THREE Block 2

SPECIFICATION DATA SHEET

ELECTROSTATIC PRECIPITATOR

FLUOR

SHEET NO. 2 of 2 REV.
BY Lurgi DATE 10.6.81
INQ. NO.
P.O. NO EX 20/897 529
PAGE 2 OF 2

MECHANICAL DESIGN

COLLECTING SYSTEM/PRECIPITATOR		NO. & TYPE HIGH VOLTAGE SWITCHES	8
NUMBER OF GAS PASSAGES	76	KEY INTERLOCK:	
SPACING OF GAS PASSAGES	300 mm	CONTROL CABINET	YES (X) NO ( )
COLLECTING SURFACE: MAT'L & THICKNESS	USt12.05/1.2 mm	HIGH VOLTAGE SWITCHES	YES (X) NO ( )
COLLECTING SURFACE: EFFECTIVE LENGTH	17.28 m	ACCESS DOOR	YES (X) NO ( )
COLLECTING SURFACE: EFFECTIVE HEIGHT	13.75 m_o	TYPE TRANSFORMER RECTIFIER CONTROLS	Thyristor
TOTAL COLLECTING SURFACE AREA	36115 m_o^2	MAX. AMBIENT TEMP. FOR T.-R. °C	40
MAX. COLLECTING AREA RAPPED ANY INSTANT	147 m^2	POWER CONSUMPTION kVa/PRECIP.	332
TYPE COLLECTING ELECTRODE RAPPERS	Rothoit	TRANSFORMER-RECTIFIER KVA/PRECIP.	520
NO. OF COLLECTING ELECTRODE RAPPERS/PRECIP.	8	RAPPERS / PRECIP. KW	1,2
HIGH VOLTAGE SYSTEM:		INSULATOR HEATER & BLOWERS (KVA/PRECIP.)	25.6
DISCHARGE ELECTRODE-TYPE	Jsodyn B5	TOTAL LOAD /PRECIPITATOR KW	358.8
MATERIAL	MU St 2 LGG BK	INDIVIDUAL BREAKERS EACH CONTROL CABINETS	YES ( ) NO (X)
THICKNESS	5 x 1,5 mm	CENTRAL DISTRIBUTION PANEL	YES ( ) NO (X)
TOTAL EFFECTIVE LENGTH OF DISCH. ELECTRODE	110800m	CASING HEAT INSULATION	YES ( ) NO (X)
TYPE DISCH. ELECTRODE RAPPERS	impact hammer	TYPE	
NO. OF ~~[illegible]~~ ELECTRODE RAPPERS/PRECIP.	16	THICKNESS (cm)	
Discharge.		INSULATOR COMPARTMENT BLOWER	YES ( ) NO (X)
HIGH VOLTAGE ELECTRICAL SET:		SYSTEM AND NUMBER	
TYPE TRANSFORMER-RECTIFIERS	Silicon	INSULATOR HEATER	YES (X) NO ( )
NUMBER TRANSFORMER-RECTIFIERS	4	TYPE AND NUMBER	electrical,32
SIZE TRANSFORMER-RECTIFIERS	1.325x1.255x1.7m	EXPANSION JOINTS	YES ( ) NO (X)
VOLTAGE RATING kV (DC) AVG.	39	LOCATION	
CURRENT RATING MILLIAMPS (DC) AVG.	2000	TYPE	
NO. OF T.R. CONTROL CABINETS	4	DAMPERS	YES ( ) NO (X)
CONSTRUCTION OF CONTROL CABINETS	steel sheeted cubicles	TYPE	
TRANSFORMER RECTIFIER INSULATION FLUID	-oil-	NUMBER	
WAVE FORM OF HIGH VOLTAGE	full wave	DIMENSION	

REMARKS:

* Air-fuel-ratio n (furnace) 1.2
** preliminary

VOLUME : 8
CHAPTER : 4.4.3.1.D.1
PAGE : 2
REV :

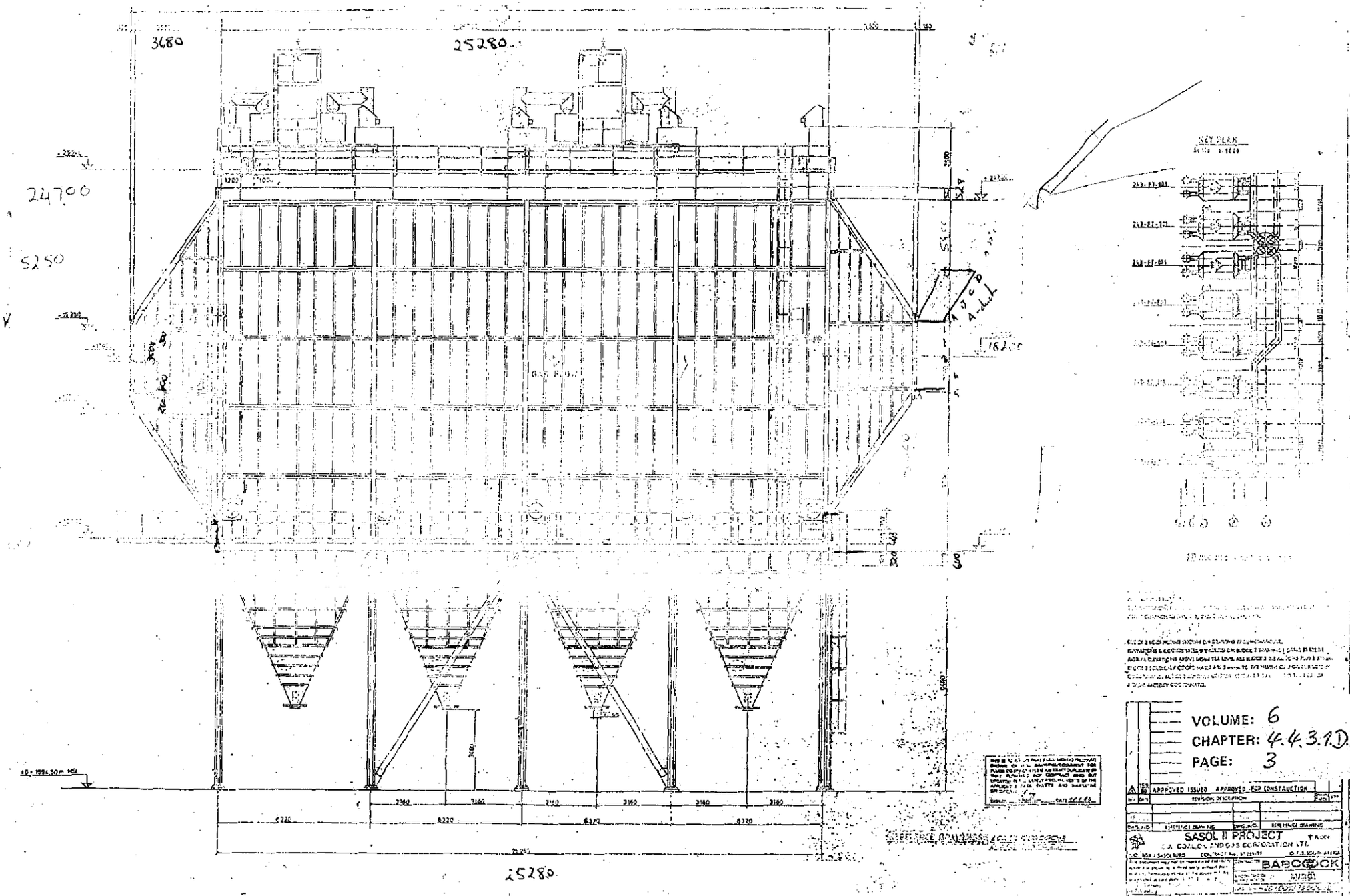

VOLUME: 6
CHAPTER: 4.4.3.1.D.2
PAGE: 3

APPROVED ISSUED APPROVED FOR CONSTRUCTION

SASOL II PROJECT

BABCOCK

PRECIPITATOR No 243-FT-101

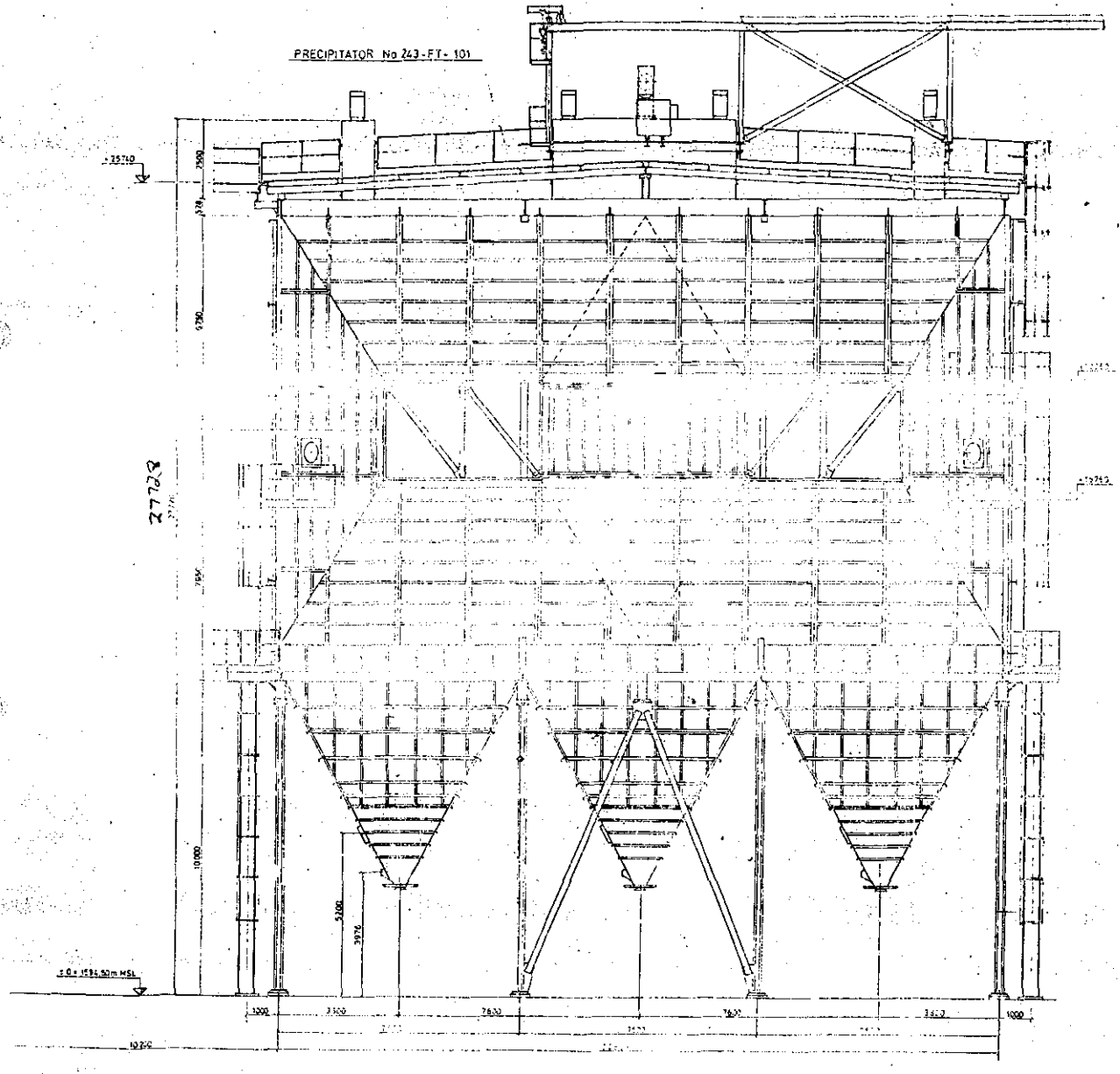

KEY PLAN

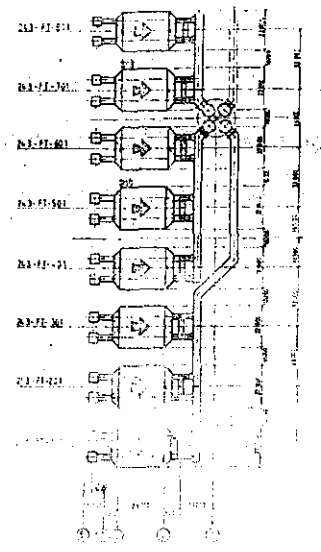

Level = 0,00m = 1 556,5m - MSL

REFERENCE DRAWINGS

VOLUME: 6
CHAPTER: 4.4.3.1.D.2
PAGE: 4

SASOL II PROJECT
SA COAL, OIL AND GAS CORPORATION LTD

BABCOCK

PRECIPITATOR CASING CROSS SECTION

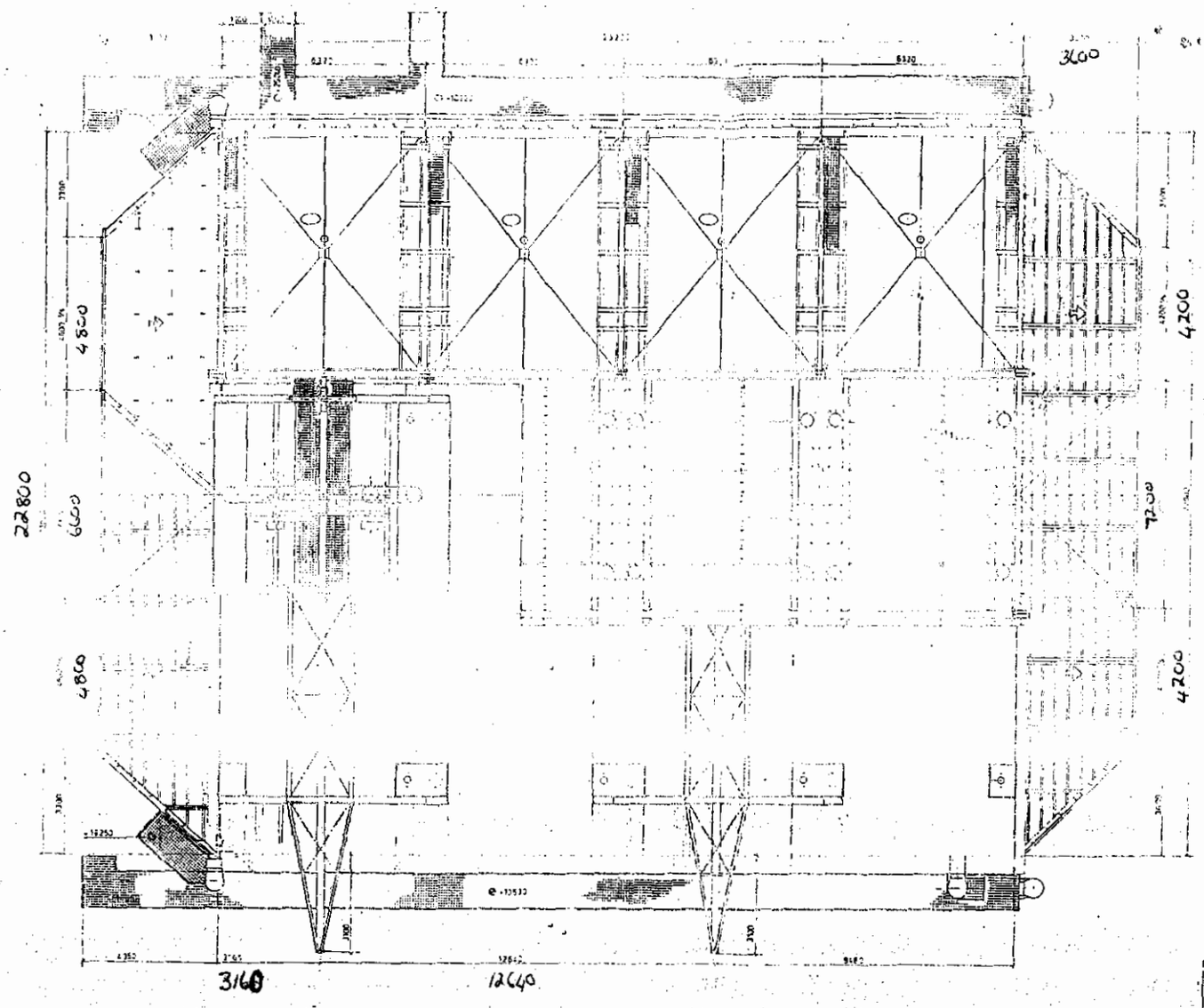

KEY PLAN

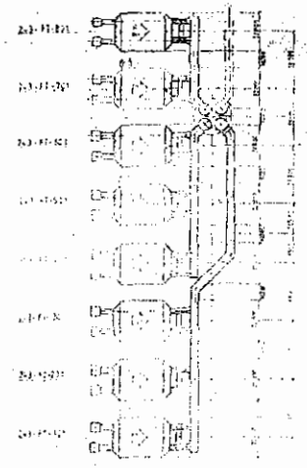

BLOCK 2 – FIRST THREE

ALL FIGURED ITEMS. FAILURE TO INCORPORATE MODIFICATIONS WITH CHANGE TO AXES OR UNIT NUMBER.

FOR INSTRUMENT NUMBERING, REPLACE THE FIRST UNIT DIGIT WITH THE FOLLOWING ALPHA CHARACTERS: 0=A, 1=B, 2=C, 3=D, 4=E, 5=F, 6=G.

BLOCK 2 LOCATION IS SHOWN ON DRAWING 4320H-0040-0002.
ELEVATIONS & COORDINATES INDICATED ON BLOCK 2 DRAWINGS SHALL BE USED ACTUAL ELEVATIONS ABOVE MEAN SEA LEVEL ARE BLOCK 2 ELEVATIONS PLUS 2.700 m.
BLOCK 2 SURVEY COORDINATES ARE 2 metres TO THE NORTH OF ACTUAL FACTORY COORDINATES. BLOCK 2 SURVEY COORDINATES ARE TWO metres TO THE WEST OF ACTUAL FACTORY COORDINATES.

DRAWN IS PRECIPITATOR 243-FT-101

REFERENCE DRAWINGS: L0A0072600012
L0A0072850012

BABCOCK

VOLUME: 6
CHAPTER: 4.4.3.1.0.2
PAGE: 5

NO.	REVISION DESCRIPTION	BY
1	APPROVED ISSUED AFFICHES FOR CONSTRUCTION	

SASOL II PROJECT
SASOL COAL OIL AND GAS CORPORATION LTD

BABCOCK

APPENDIX B: Simulation Results

The appendix presents some of the major results obtained form the ESP model.

Appendix B-1: ESP with DP and EF.

Figure B-1 illustrates the gas flow through an entire ESP with distribution plates (DP) and with electrical fields (EF) for three different inlet velocities.

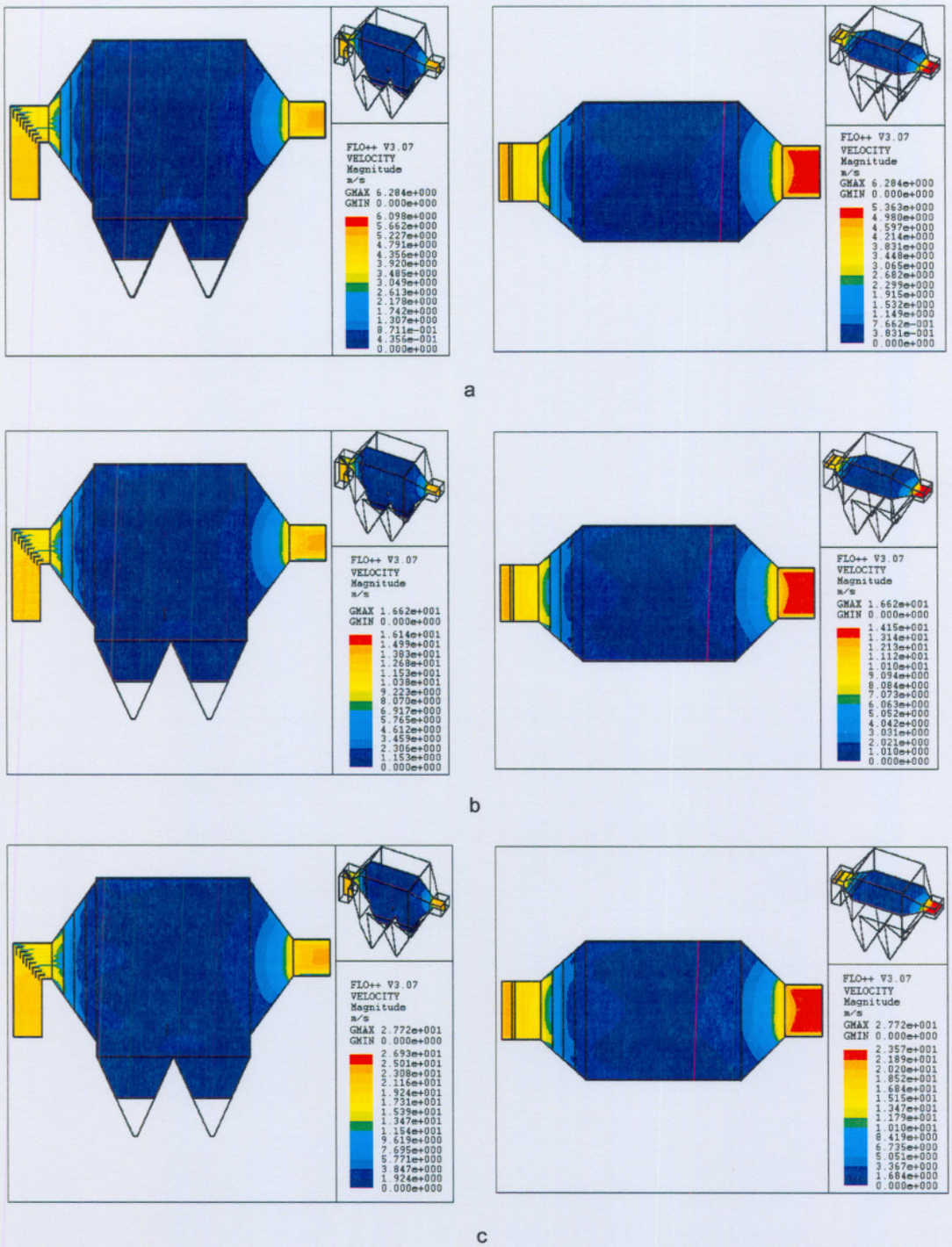

Figure B-1: Gas flow through ESP with DP and with EF. a) v_{inlet} = 5 (m/s) b) v_{inlet} = 13.2 (m/s) c) v_{inlet} = 22 (m/s)

Appendix B-2: ESP with DP and without EF.

Figure B-2 illustrates the gas flow through an entire ESP with distribution plates (DP) but without electrical fields (EF) for three different inlet velocities.

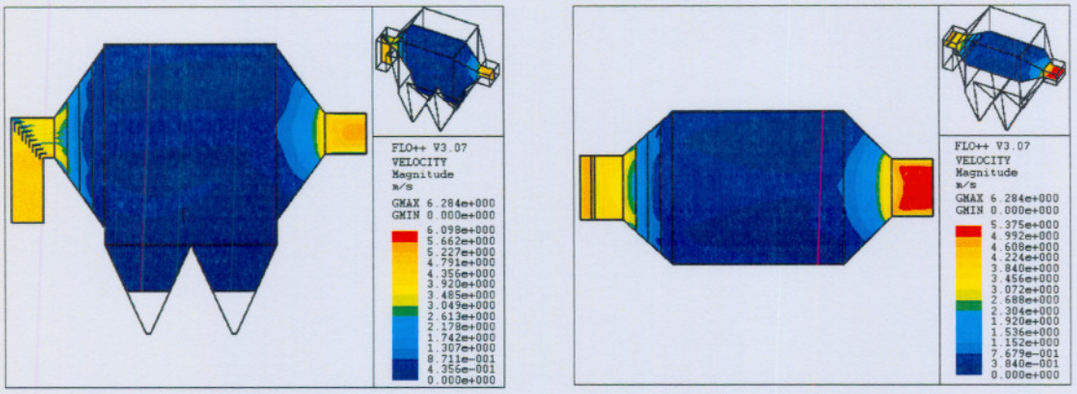

a

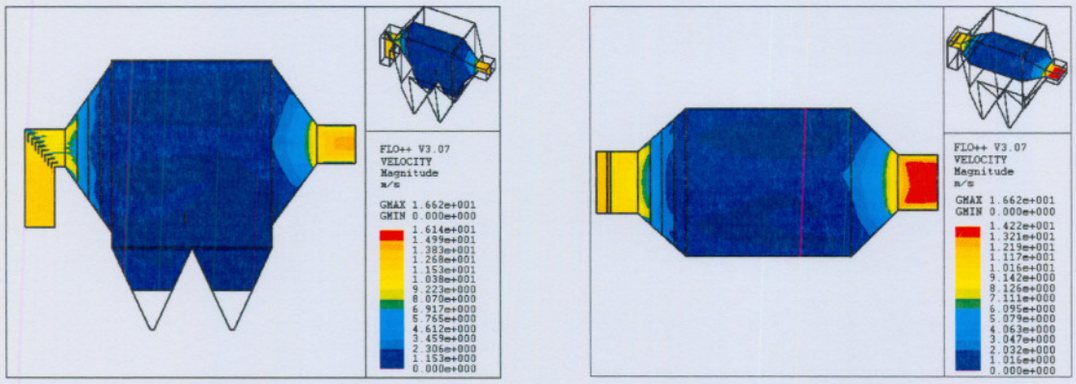

b

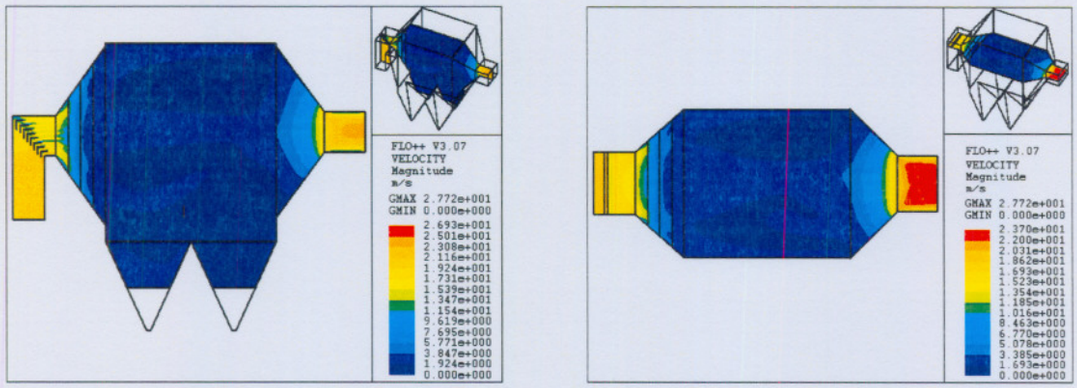

c

Figure B-2: Gas flow through ESP with DP and without EF. a) v_{inlet} = 5 (m/s) b) v_{inlet} = 13.2 (m/s) c) v_{inlet} = 22 (m/s)

Appendix B-3: ESP with EF and without DP.

Figure B-3 illustrates the gas flow through an entire ESP with electrical fields (EF) but without distribution plates (DP) for three different inlet velocities.

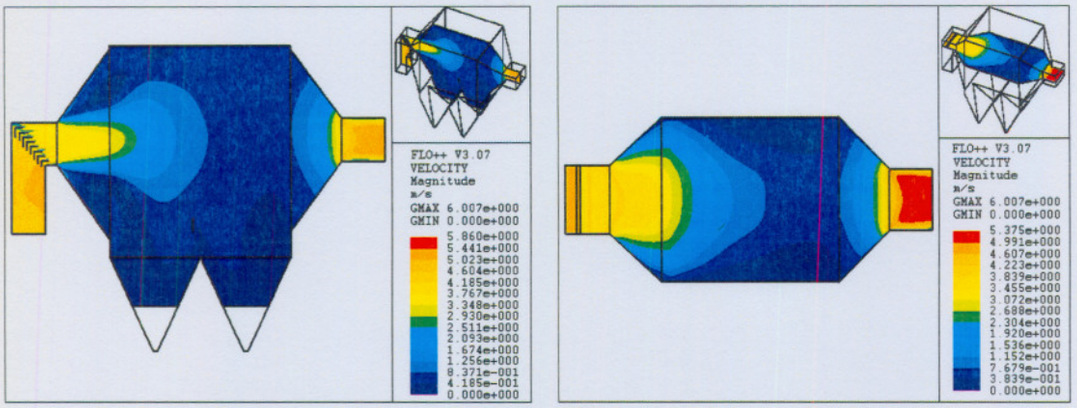

a

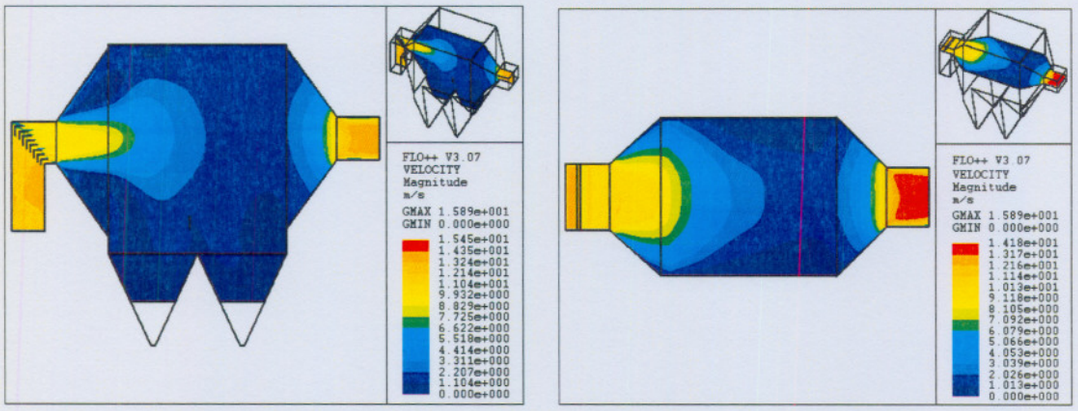

b

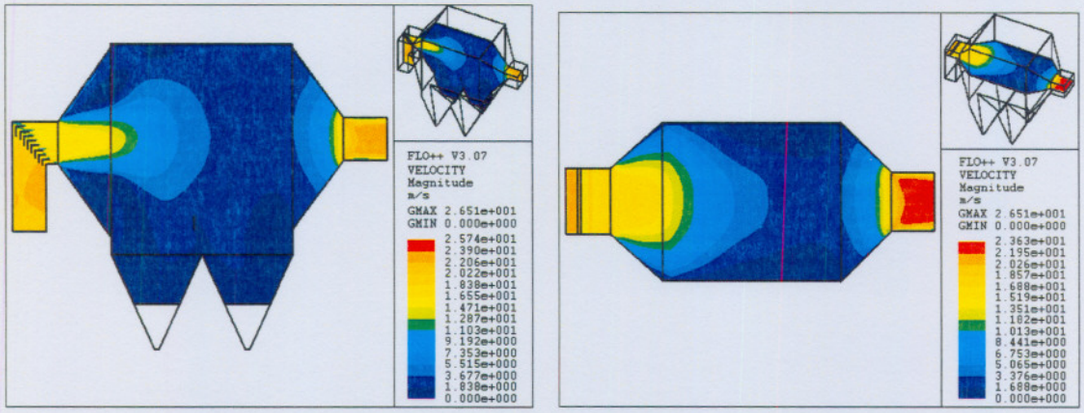

c

Figure B-3: Gas flow through ESP with EF and without DP. a) v_{inlet} = 5 (m/s) b) v_{inlet} = 13.2 (m/s) c) v_{inlet} = 22 (m/s)

Appendix B-4: ESP without DP and without EF

Figure B-4 illustrates the gas flow through an entire ESP without electrical fields (EF) and without distribution plates (DP) for three inlet velocities.

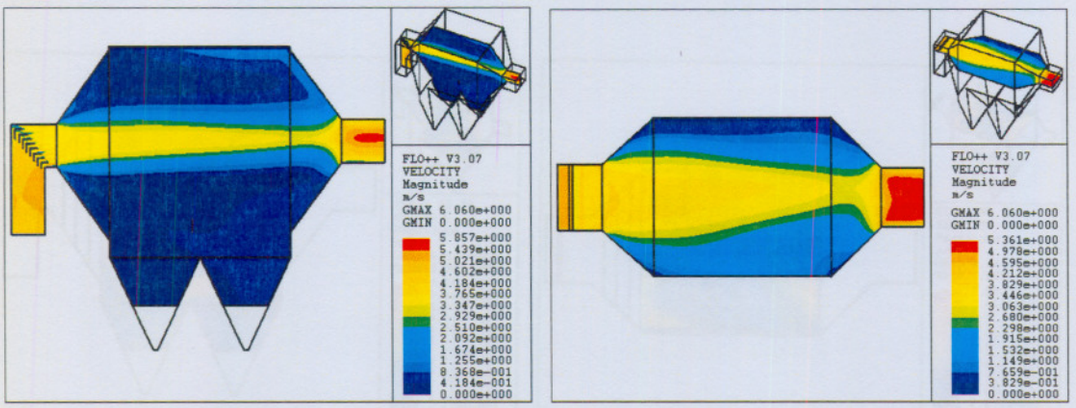

a

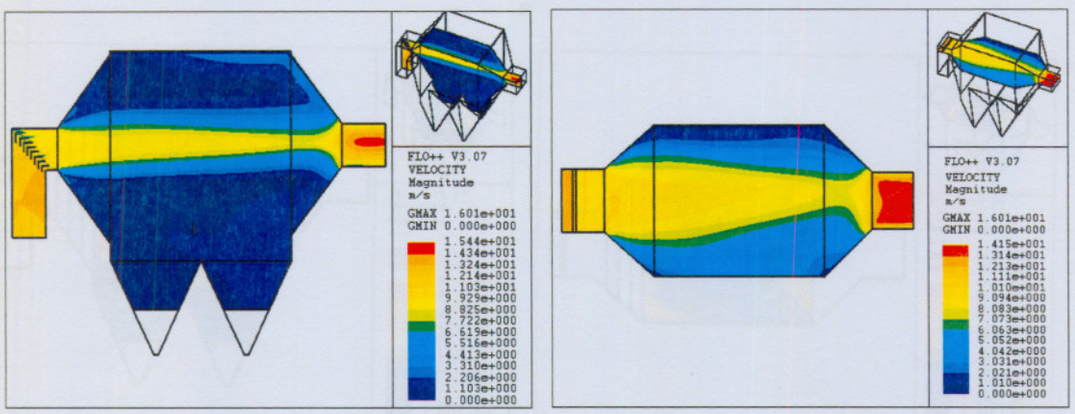

b

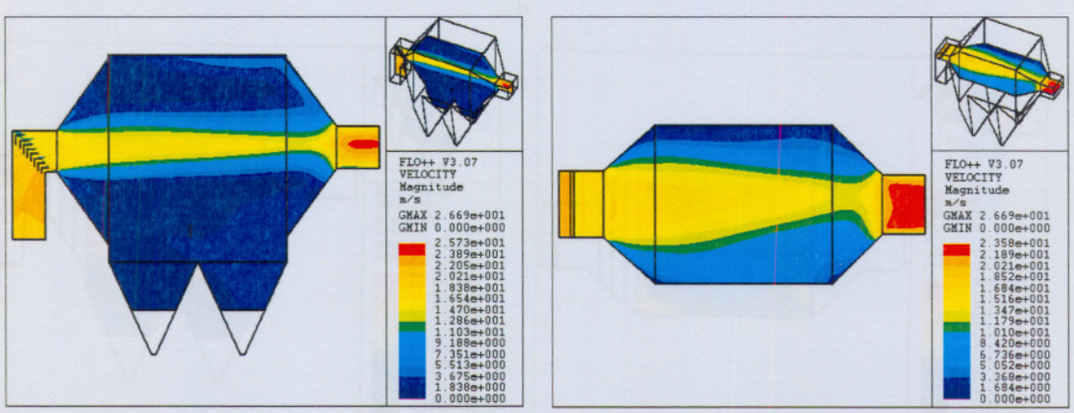

c

Figure B-4: Gas flow through ESP without EF and without DP. a) v_{inlet} = 5 (m/s) b) v_{inlet} = 13.2 (m/s) c) v_{inlet} = 22 (m/s)

Appendix B-5: Collecting area with DP and EF

Figure B-5 illustrates the gas flow through the collecting flow area with electrical fields (EF) and with distribution plates (DP) for three inlet velocities.

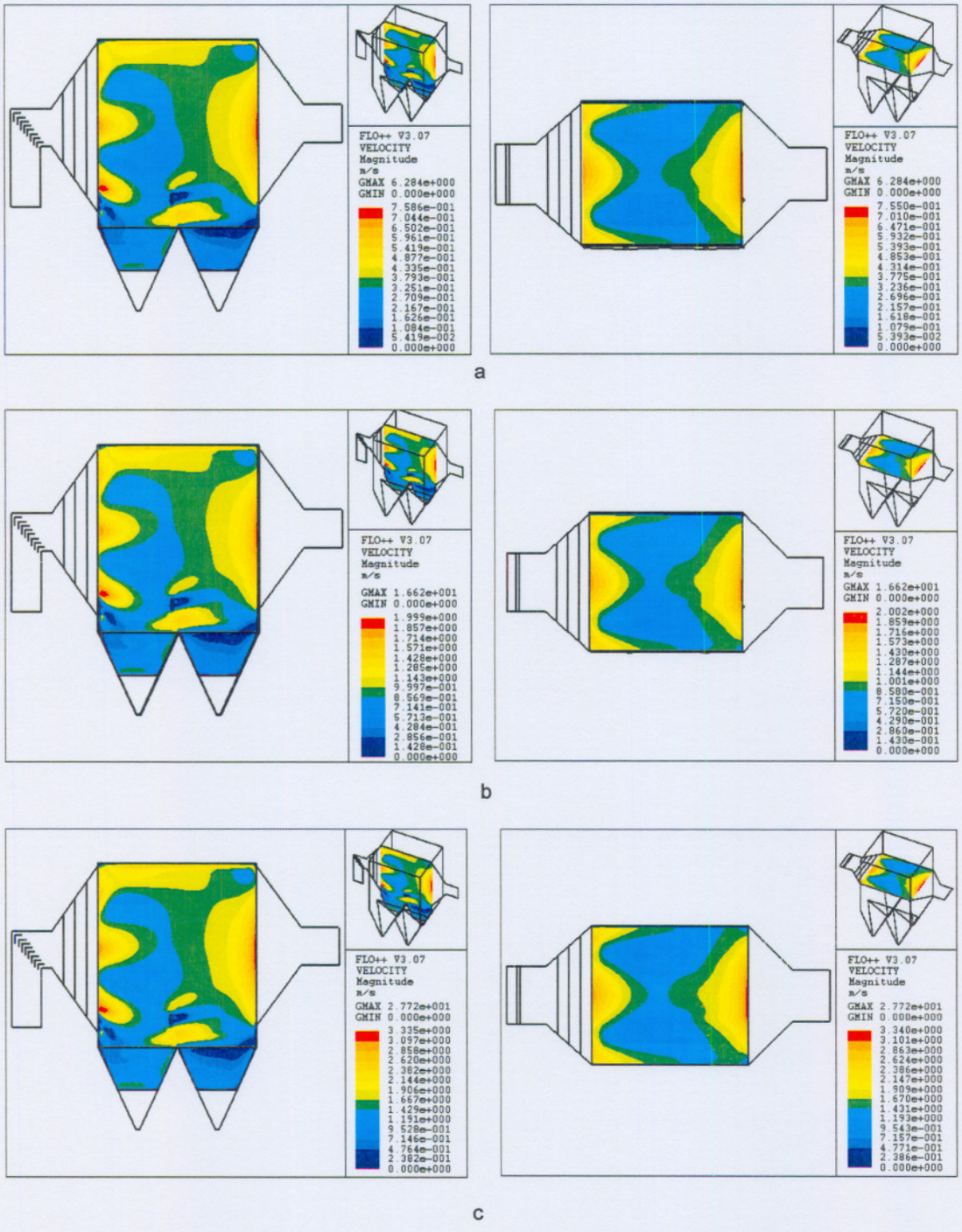

Figure B-5: Gas flow through collecting area with EF and with DP. a) v_{inlet} = 5 (m/s) b) v_{inlet} = 13.2 (m/s) c) v_{inlet} = 22 (m/s)

Appendix B-6: Collecting area with DP and without EF

Figure B-6 illustrates the gas flow through the collecting flow area without electrical fields (EF) and with distribution plates (DP) for three inlet velocities.

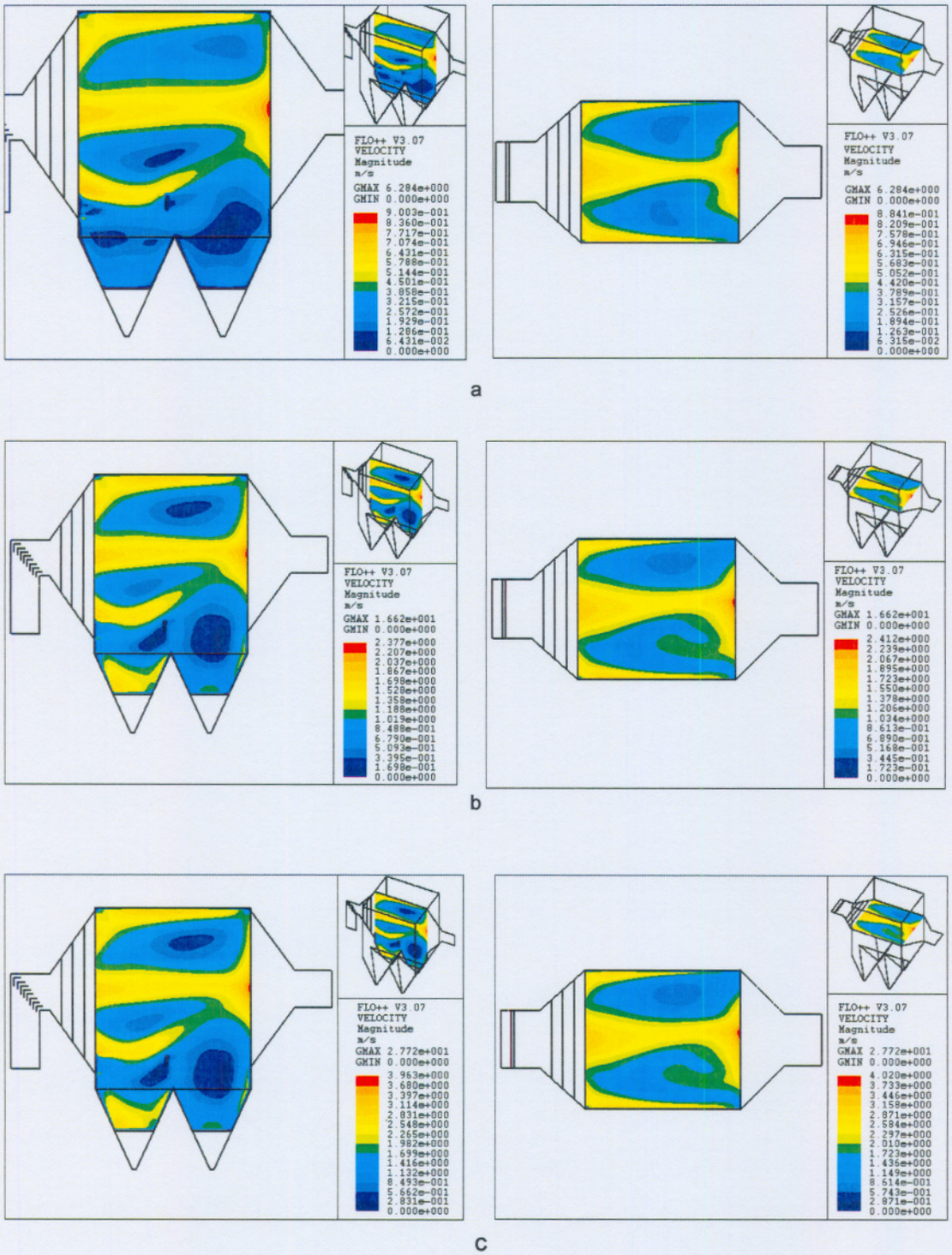

Figure B-6: Gas flow through collecting area without EF and with DP. a) v_{inlet} = 5 (m/s) b) v_{inlet} = 13.2 (m/s) c) v_{inlet} = 22 (m/s)